AD-A012 476

AURORAL SIMULATION STUDIES. HAES REPORT
NUMBER 6

Douglas H. Archer, et al

Mission Research Corporation

Prepared for:

Defense Nuclear Agency

22 April 1975

209141

DNA 3567T

AURORAL SIMULATION STUDIES

HAES Report No. 6

Mission Research Corporation

735 State Street

Santa Barbara, California 93101

22 April 1975

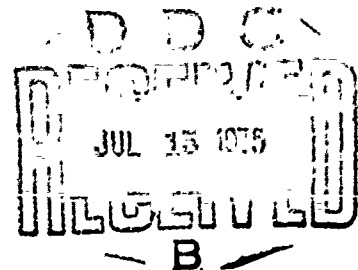Topical Report for Period 1 January 1974—30 September 1974

CONTRACT No. DNA 001-74-C-0143

> **APPROVED FOR PUBLIC RELEASE;**
> **DISTRIBUTION UNLIMITED.**

Prepared for

Director

DEFENSE NUCLEAR AGENCY

Washington, D. C. 20305

D D C

JUL 15 1975

— B

REPORT DOCUMENTATION PAGE		READ INSTRUCTIONS BEFORE COMPLETING FORM
1. REPORT NUMBER DNA 3567T	2. GOVT ACCESSION NO.	3. RECIPIENT'S CATALOG NUMBER AD-A 012 476
4. TITLE *(and Subtitle)* AURORAL SIMULATION STUDIES HAES Report No. 6		5. TYPE OF REPORT & PERIOD COVERED Topical Report for Period 1 Jan 74—30 Sep 74
		6. PERFORMING ORG. REPORT NUMBER MRC-R-152
7. AUTHOR(s) Douglas H. Archer Paul W. Tarr		8. CONTRACT OR GRANT NUMBER(s) DNA 001-74-C-0143
9. PERFORMING ORGANIZATION NAME AND ADDRESS Mission Research Corporation 735 State Street Santa Barbara, California 93101		10. PROGRAM ELEMENT, PROJECT, TASK AREA & WORK UNIT NUMBERS NWET Subtask L25AAXYX966-17
11. CONTROLLING OFFICE NAME AND ADDRESS Director Defense Nuclear Agency Washington, D.C. 20305		12. REPORT DATE 22 April 1975
		13. NUMBER OF PAGES ~~152~~ 147
14. MONITORING AGENCY NAME & ADDRESS(*if different from Controlling Office*)		15. SECURITY CLASS. (*of this report*) UNCLASSIFIED
		15a. DECLASSIFICATION/DOWNGRADING SCHEDULE

16. DISTRIBUTION STATEMENT *(of this Report)*

Approved for public release; distribution unlimited.

17. DISTRIBUTION STATEMENT *(of the abstract entered in Block 20, if different from Report)*

18. SUPPLEMENTARY NOTES

This work sponsored by the Defense Nuclear Agency under Subtask
L25AAXYX966-17.

19. KEY WORDS *(Continue on reverse side if necessary and identify by block number)*

Aurora	Auroral Code
Electron Excitation	Auroral Simulation
Infrared Radiation	

20. ABSTRACT *(Continue on reverse side if necessary and identify by block number)*

This report describes work performed in three areas of activity:
(1) applications of the ARCTIC code, especially to a study of and comparison
with ICECAP data from an auroral event recorded near Poker Flat, Alaska on
27 March 1973, (2) study of certain applications of aurorally-generated
extreme ultraviolet (EUV) radiation in an auroral environment, and (3)
atmospheric heave resulting from auroral bombardment.

PRICES SUBJECT TO CHANGE

20. ABSTRACT (Continued)

A detailed model was constructed to describe the auroral event, consisting of a main arc and its associated drizzle environment. Based on this model, comparisons between ARCTIC code calculations and preliminary field data suggest a number of discrepancies. These are described in detail and possible sources for the differences are suggested.

Study of EUV effects in the aurora has led to the preliminary conclusions that (a) the N_2 molecule is an unlikely source for certain LWIR features observed on ICECAP and (b) the EUV is probably not an important source of 5577 Å emission in the aurora.

Intense auroral bombardment over a period of 4 minutes is found to result in negligible atmospheric heave.

Recommendations pertaining to future laboratory and field measurement programs are given.

ja

SUMMARY

       The work reported herein could not have been accomplished without the help and cooperation of a number of individuals involved directly in the ICECAP program. Preliminary data provided to us by them, prior to its publication in reports or in the open literature, has been of great benefit. Special thanks go to Mr. James Ulwick and Dr. Rocco Narcisi (AFCRL), Dr. Kay Baker (Utah State University), and Drs. Irving Kofsky and John Schroeder (Photometrics). Benefit was also derived from conversations with Drs. A. T. Stair (AFCRL), Richard Hegblom (Boston College), and Murray Baron (SRI). Additional aid provided by Major Lawrence Doan (DNA) is much appreciated. The assistance of all these individuals is hereby gratefully acknowledged.

PREFACE

The High Altitude Effects Simulation (HAES) Program sponsored by the Defense Nuclear Agency since the early 1970 time period, comprises several groupings of separate, but interrelated technical activities, e.g. ICECAP (Infrared Chemistry Experiments - Coordinated Auroral Program). Each of the latter have the common objective of providing information ascertained as essential for the development and validation of predictive computer codes designed for use with high priority DoD radar, communications, and optical defensive systems.

Since the inception of the HAES Program, significant achievement and results have been described in reports published by DNA, participating service laboratories, and supportive organizations. In order to provide greater visibility for such information and enhance its timely applications, significant reports published since early calendar 1974 shall be identified with an assigned HAES serial number and the appropriate activity acronym (e.g. ICECAP) as part of the report title. A complete and current bibliography of all HAES reports issued prior to and subsequent to HAES Report No. 1, dated 5 February 1974 entitled, "Rocket Launch of an SWIR Spectrometer into an Aurora (ICECAP 72)," AFCRL Environmental Research Paper No. 466, is maintained and available on request from DASIAC, DoD Nuclear Information and Analysis Center, 816 State Street, Santa Barbara, California 93102, Telephone (805) 965-0551.

This is the sixth report in the HAES series and covers technical work performed under DNA Contract 001-74-C-0143 from 1 January 1974 to

2

30 September 1974. Po.tions of this program were previously reported in DNA Report 3297F entitled: "Studies of Auroral Simulation". The main purpose of the work is to understand auroral data, especially those obtained under the ICECAP program, so that better models can be constructed to describe the nuclear-disturbed environment. One of the principal tools used for this purpose is the ARCTIC code that embodies a wide range of phenomenon including excitation of atomic, ionic, and molecular states, chemical reactions, and optical/IR radiation in an auroral environment. The present report includes a description of some calculations pertinent to auroral events and comparisons with experimental observations.

TABLE OF CONTENTS

TABLE OF CONTENTS (Continued)

LIST OF ILLUSTRATIONS

LIST OF ILLUSTRATIONS (Continued)

8

LIST OF TABLES

SECTION 1
INTRODUCTION

This report describes the continuing work on auroral simulation performed from 1 January 1974 to 30 September 1974. Related work on the prior contract was reported in Reference 1.

The main purpose of these studies is to understand auroral data, especially those obtained under the ICECAP program, so that better models can be constructed to describe the nuclear-disturbed environment.

One of the principal tools developed for use in these studies is the ARCTIC code, described in Reference 1. It is especially suitable for analyzing data from multi-experiment rocket flights that provide simultaneous information on particle fluxes, chemical species, and optical/infrared emissions for single auroral events. Indeed, it is in this capacity that the code has been largely used so far.

Section 2 below contains the bulk of our work relating to use of the ARCTIC code. It includes (1) the detailed energy partition by primary electrons incident on "normal" air as predicted by the current version of the ARCTIC code, (2) results prepared for a code-comparison meeting at Lockheed, Palo Alto, on 14 June 1974, (3) a detailed comparison with ICECAP data for an IBC III auroral event recorded by ground- and rocket-based instruments, and (4) a comparison between calculated and observed auroral emissions from $O_2(^1\Delta)$.

11

Section 3 outlines our exploratory efforts to account for certain long wavelength infrared (LWIR) features observed on ICECAP. It also gives some preliminary conclusions with respect to the importance of aurorally-generated extreme ultraviolet (EUV) radiation in an auroral environment.

Section 4 presents the results of our study of atmospheric heave under intense auroral bombardment conditions.

Section 5 summarizes our conclusions and lists some specific recommendations.

Three appendices are included. Appendix A describes a derivation of the spectral distribution of chemiluminescent emission in the fundamental and first overtone bands of NO arising from the reaction $N(^2D) + O_2 \rightarrow NO + O$. Appendix B gives corresponding results for NO^+ chemiluminescence arising from the reactions $O_2^+ + NO \rightarrow O_2 + NO^+$ and $N_2^+ + O \rightarrow NO^+ + N$. Appendix C briefly describes the structure of the ARCTIC code and includes (on micro-fiche) a complete listing of the program.

Tentative conclusions, based on a study of the "Murcray phenom-enon", were reported separately (Reference 2).

12

SECTION 2
APPLICATIONS OF THE ARCTIC CODE

A detailed description of the ARCTIC code can be found in Reference 1. It will not be repeated here, although a listing of the code and a brief outline of its structure appear in Appendix C. Before proceeding with the applications, however, the following remarks are appropriate.

As explained in Reference 1, scattering of the primary electrons can be treated using two different versions of the code. The first, and simplest version, is based on what we call the mean scattering approximation in which each electron is assumed to have the same range. The second version, called scattering with range variance, recognizes the fact that there is actually a distribution in range among those electrons that have a common mean range. The second, and more accurate version, was believed to be considerably more expensive to run than the first one. We have since found, however, that the range-variance version is much faster than expected (less than a factor of 2 more than the simpler version). The results presented below are based on the more accurate range-variance version of the code.

This section presents four applications of the code. The first, and simplest, is a tabulation of species populations produced in "normal" air by the total stopping of primary electrons. Such a tabulation is often needed as input to chemistry and optical/infrared codes used for weapon effects studies involving the deposition of x rays or beta particles. The second is a calculation, for the case of a hypothetical aurora, performed for comparison purposes at a DNA-sponsored meeting at Lockheed, Palo Alto, on 14 June 1974. The third, and major application, is to the case of an

13

auroral arc measured by ground- and rocket-based instruments on the night of March 27, 1973. A detailed comparison with the data available to us is made, and conclusions and inferences drawn therefrom are given. The fourth application is to auroral enhancement of $O_2(^1\Delta)$ emission at 1.27 μm compared with some observations reported in the literature.

SPECIES POPULATIONS IN "NORMAL" AIR UNDER ELECTRON BOMBARDMENT

The partition of energy into states of excitation, ionization, and dissociation was determined for primary electrons stopped in a "normal" air mixture consisting of 79% N_2 and 21% O_2. Results were obtained for primary energies between 0.17 eV and 27 keV. For the sake of compactness, however, only the results for energies of 0.92 keV and 6 keV are presented here. These appear in Table 2-1.

For each of the two primary energies, Table 2-1 lists the population of the species produced directly by the primary electron as well as the total population, including contributions from all generations of secondary electrons. Also listed are the populations produced per ion pair. The Rydberg states with different values of the principal quantum number, n, are lumped together for each of the series[*]. The energies of the individual states fall within the ranges indicated in the second column of the table.

Calculated values of the average energy required to produce an ion pair in the air mixture, as a function of the primary electron energy, are shown in Figure 2-1. They are in excellent agreement with limited data obtained at energies above 1 keV with beta particles in air (Reference 3). Similar calculations have been performed for electrons incident in pure N_2 and pure O_2 and the results (not shown) are in correspondingly good agreement with the limited data.

---

[*] The code actually computes the partition into states with different n, but for the sake of compactness we have merged the results in Table 2-1 for each of the Rydberg series.

14

Table 2-1. Species populations in "normal" air (79% N_2, 21% O_2) produced by the stopping of 0.92 keV and 6 keV electrons.

Species	State Energy (eV)	Primary Population		Total Population		Population Per Ion Pair	
		0.92 keV	6 keV	0.92 keV	6 keV	0.92 keV	6 keV
$N_2(1)$ [1]	0.29	2.7	2.7	4.5^1	2.9^2	1.8	1.7
$N_2(2)$	0.57	9.4^{-1}	9.4^{-1}	1.6^1	1.0^2	6.3^{-1}	5.7^{-1}
$N_2(3)$	0.86	3.8^{-1}	3.8^{-1}	6.6	4.2^1	2.6^{-1}	2.4^{-1}
$N_2(4)$	1.13	2.8^{-1}	2.8^{-1}	4.7	3.0^1	1.8^{-1}	1.7^{-1}
$N_2(5)$	1.41	1.8^{-1}	1.8^{-1}	3.1	2.0^1	1.2^{-1}	1.1^{-1}
$N_2(6)$	1.68	1.2^{-1}	1.2^{-1}	2.1	1.3^1	8.2^{-2}	7.4^{-2}
$N_2(7)$	1.95	9.3^{-2}	9.3^{-2}	1.6	1.0^1	6.3^{-2}	5.7^{-2}
$N_2(8)$	2.21	5.5^{-2}	5.5^{-2}	9.4^{-1}	6.0	3.7^{-2}	3.4^{-2}
$N_2(A^3\Sigma_u^+)$	6.17	5.2^{-1}	5.2^{-1}	5.1	3.3^1	2.0^{-1}	1.9^{-1}
$N_2(B^3\Pi_g)$	7.35	6.6^{-1}	8.5^{-1}	4.5	2.8^1	1.8^{-1}	1.6^{-1}
$N_2(C^3\Pi_u)$	11.03	2.6^{-1}	2.6^{-1}	1.7	1.1^1	6.6^{-2}	6.3^{-2}
$N_2(E^3\Sigma_g^+)$	11.9	3.1^{-2}	3.1^{-2}	2.1^{-1}	1.3	8.2^{-3}	7.4^{-3}
$N_2(a^1\Pi_g)$ [2]	8.55	5.9^{-1}	1.0	2.9	1.8^1	1.1^{-1}	1.0^{-1}
$N_2(^1\Sigma_g^+)$ [3]	12.25	8.1^{-2}	1.6^{-1}	2.8^{-1}	1.7	1.1^{-2}	9.7^{-3}
$N_2(b^1\Pi_u)$ [4]	12.80	1.9	9.3	2.8	1.8^1	1.1^{-1}	1.0^{-1}
$N_2(b'^1\Sigma_u^+)$	14.00	8.7^{-1}	4.2	1.2	7.9	4.7^{-2}	4.5^{-2}
$N_2[Ry(X)]$ [5]	$13.01 \to 14.84$	2.6	1.3^1	3.6	2.4^1	1.4^{-1}	1.4^{-1}
$N_2[Ry(A)]$ [6]	$13.19 \to 15.86$	7.5^{-1}	3.6	1.0	6.8	3.9^{-2}	3.9^{-2}
$N_2[Ry(B)]$	$15.75 \to 17.95$	8.1^{-2}	4.2^{-1}	1.0^{-1}	6.8^{-1}	3.9^{-3}	3.9^{-3}
$N_2[Ry(D)]$	$15.71 \to 20.87$	1.4^{-1}	7.2^{-1}	1.8^{-1}	1.2	7.0^{-3}	6.9^{-3}
$N_2[Ry(C)]$	$20.79 \to 22.83$	3.4^{-2}	1.9^{-1}	4.0^{-2}	2.7^{-1}	1.6^{-3}	1.5^{-3}
$N(^4S)$ [7]	-	3.7	1.8^1	5.8	3.8^1	2.3^{-1}	2.2^{-1}
$N(^2D)$	-	3.7	1.9^1	5.4	3.7^1	2.1^{-1}	2.1^{-1}
$N(^2P)$	-	1.1	6.7	1.6	1.2^1	6.3^{-2}	6.7^{-2}
$N_2^+(X^2\Pi_g)$ [8]	15.58	7.2	3.6^1	9.0	5.9^1	3.5^{-1}	3.4^{-1}
$N_2^+(A^2\Pi_u)$	16.73	3.6	1.9^1	4.4	2.9^1	1.7^{-1}	1.7^{-1}
$N_2^+(B^2\Sigma_u^+)$	18.75	1.6	8.5	1.8	1.3^1	7.0^{-2}	7.4^{-2}
$N_2^+(D^2\Pi_g)$	22.00	7.1^{-1}	4.1	8.1^{-1}	5.6	3.2^{-2}	3.2^{-2}
$N_2^+(C^2\Sigma_u^+)$	23.60	7.3^{-1}	4.3	8.1^{-1}	5.8	3.2^{-2}	3.3^{-2}
$N^+(^3P)$ [9]	-	1.9	1.2^1	2.1	1.6^1	8.2^{-2}	9.1^{-2}
$N^+(^2D)$	-	7.9^{-1}	5.7	8.8^{-1}	7.3	3.4^{-2}	4.2^{-2}
$N^+(^1S)$	-	2.4^{-1}	1.8	2.7^{-1}	2.3	1.1^{-2}	1.3^{-2}

Table 2-1 (Continued). Species populations in "normal" air (79% N_2, 21% O_2) produced by the stopping of 0.92 keV and 6 keV electrons.

Species	State Energy (eV)	Primary Population		Total Population		Population Per Ion Pair	
		0.92 keV	6 keV	0.92 keV	6 keV	0.92 keV	6 keV
$O_2(v)$	~0.25	5.6	5.6	1.1^2	7.2^2	4.3	4.1
9.9 eV peak[10]	9.90	6.7^{-2}	2.4^{-1}	1.2^{-1}	7.5^{-1}	4.7^{-3}	4.3^{-3}
$O_2(a^1\Delta_g)$	0.98	6.4^{-1}	6.4^{-1}	9.9	6.4^1	3.9^{-1}	3.7^{-1}
$O_2(b^1\Sigma_g^+)$	1.64	1.5^{-1}	1.5^{-1}	2.2	1.4^1	8.6^{-2}	8.0^{-2}
$O_2(A^3\Sigma_u^+)$ [11]	4.50	6.2^{-1}	7.5^{-1}	7.3	4.7^1	2.9^{-1}	2.7^{-1}
$O_2(B^3\Sigma_u^-)$ [12]	6.10	1.0	3.8	2.4	1.5^1	9.4^{-2}	8.6^{-2}
$O_2[Ry(X)]$	8.41 → 11.22	3.5^{-1}	1.5	6.5^{-1}	4.1	2.5^{-2}	2.3^{-2}
$O_2[Ry(a)]$ [13]	12.70 → 15.25	1.7^{-1}	8.4^{-1}	2.4^{-1}	1.6	9.4^{-3}	9.1^{-3}
$O_2[Ry(A)]$	13.25 → 16.02	1.5^{-1}	7.3^{-1}	2.0^{-1}	1.3	7.8^{-3}	7.4^{-3}
$O_2[Ry(b)]$	15.65 → 17.47	6.4^{-2}	3.3^{-1}	8.2^{-2}	5.4^{-1}	3.2^{-3}	3.1^{-3}
$O_2[Ry(B,c)]$ [14]	19.60 → 22.15	2.5^{-2}	1.4^{-1}	2.9^{-2}	2.0^{-1}	1.1^{-3}	1.1^{-3}
$O(^3P)$	-	3.9	1.4^1	1.7^1	1.1^2	6.6^{-1}	6.3^{-1}
$O(^1D)$	-	1.0	3.8	2.4	1.5^1	9.4^{-2}	8.6^{-2}
$O_2^+(X^2\Pi_g)$	12.10	7.3^{-1}	3.6	9.9^{-1}	6.5	3.9^{-2}	3.7^{-2}
$O_2^+(a^4\Pi_u)$	16.10	7.0^{-1}	3.6	8.5^{-1}	5.6	3.3^{-2}	3.2^{-2}
$O_2^+(A^2\Pi_u)$	16.90	6.8^{-1}	3.6	8.1^{-1}	5.4	3.2^{-2}	3.1^{-2}
$O_2^+(b^4\Sigma_g^-)$	18.20	5.6^{-1}	3.0	6.6^{-1}	4.4	2.6^{-2}	2.5^{-2}
$O_2^+(B,c)$ [15]	23.00	2.4^{-1}	1.4	2.6^{-1}	1.9	1.0^{-2}	1.1^{-2}
$O^+(^4S)$	-	1.1	5.4	1.2	7.7	4.7^{-2}	4.4^{-2}
$O^+(^2D)$	-	6.2^{-1}	3.2	6.7^{-1}	4.4	2.6^{-2}	2.5^{-2}

(1) $N_2(v)$ refers to the vth vibrational state of $N_2(X^1\Sigma)$.

(2) 18% predissociation into $N(^4S) + N(^4S)$ assumed.

(3) The lowest Rydberg state of N_2.

(4) 69% predissociation into $N(^4S) + N(^2D)$ assumed.

(5) Ry(X) means the Rydberg states (n = 3,4,5+---) converging on $N_2^+(X^2\Sigma_g^+)$; similarly Ry(A) means the Rydberg states converging on $N_2^+(A^2\Pi_u)$, etc.

(6) For the Rydberg states Ry[A(n=5),B,D,C], the numbers in the table are 25% of the total excitations to the respective states. The remaining 75% are assumed to be autoionized and have been added to $N_2^+(X^2\Pi_g)$.

(7) The nitrogen atoms arise from predissociation and from dissociative excitation and dissociative ionization.

(8) Includes contributions from autoionization of Rydberg states. See note (6) above).

(9) The atomic ions arise from dissociative ionization.

(10) Unassigned.

(11) Assumed to be 100% dissociated into $O(^3P) + O(^3P)$.

(12) Assumed to be 100% dissociated into $O(^3P) + O(^1D)$.

16

Table 2-1 (Continued). Species populations in "normal" air (79% N_2, 21% O_2) produced by the stopping of 0.92 keV and 6 keV electrons.

(13) For the Rydberg states Ry(a,---), the numbers in the table are 50% of the total excitations to the respective states. The remaining 50% are assumed to be autoionized and have been added to $O_2^+(X^2\Pi_g)$.
(14) Ry(B,c) is a blend of the Rydberg states converging on the $B^2\Sigma_g^-$ and $c^4\Sigma_u^-$ states of O_2^+.
(15) A blend of the states $B^2\Sigma_g^-$ and $c^4\Sigma_u^-$.

It should be pointed out, however, that the agreement with data is partly forced because the unknown autoionization factors have been adjusted to improve the agreement. Furthermore, a large number of the excitation cross sections are not well known and, in some cases, especially for the Rydberg states, are little more than guesses. Changes in the relatively large cross sections for the Rydberg states can have an appreciable effect (the calculated values for "eV per ion pair".

TEST CASE (HYPOTHETICAL AURORA)

For the code-comparison meeting at Lockheed, two test problems were run using the ARCTIC code. The first one, described here, involved a hypothetical electron flux of exponential type. The second one, described in detail in the next subsection, was based on a flux spectrum measured under the ICECAP program.

The first problem was essentially as follows. Given an incident spectral flux of primary electrons:

$$\text{flux} = e^{-E/10} \quad (\text{electrons cm}^{-2} \text{ sec}^{-1} \text{ ster}^{-1} \text{ keV}^{-1})$$
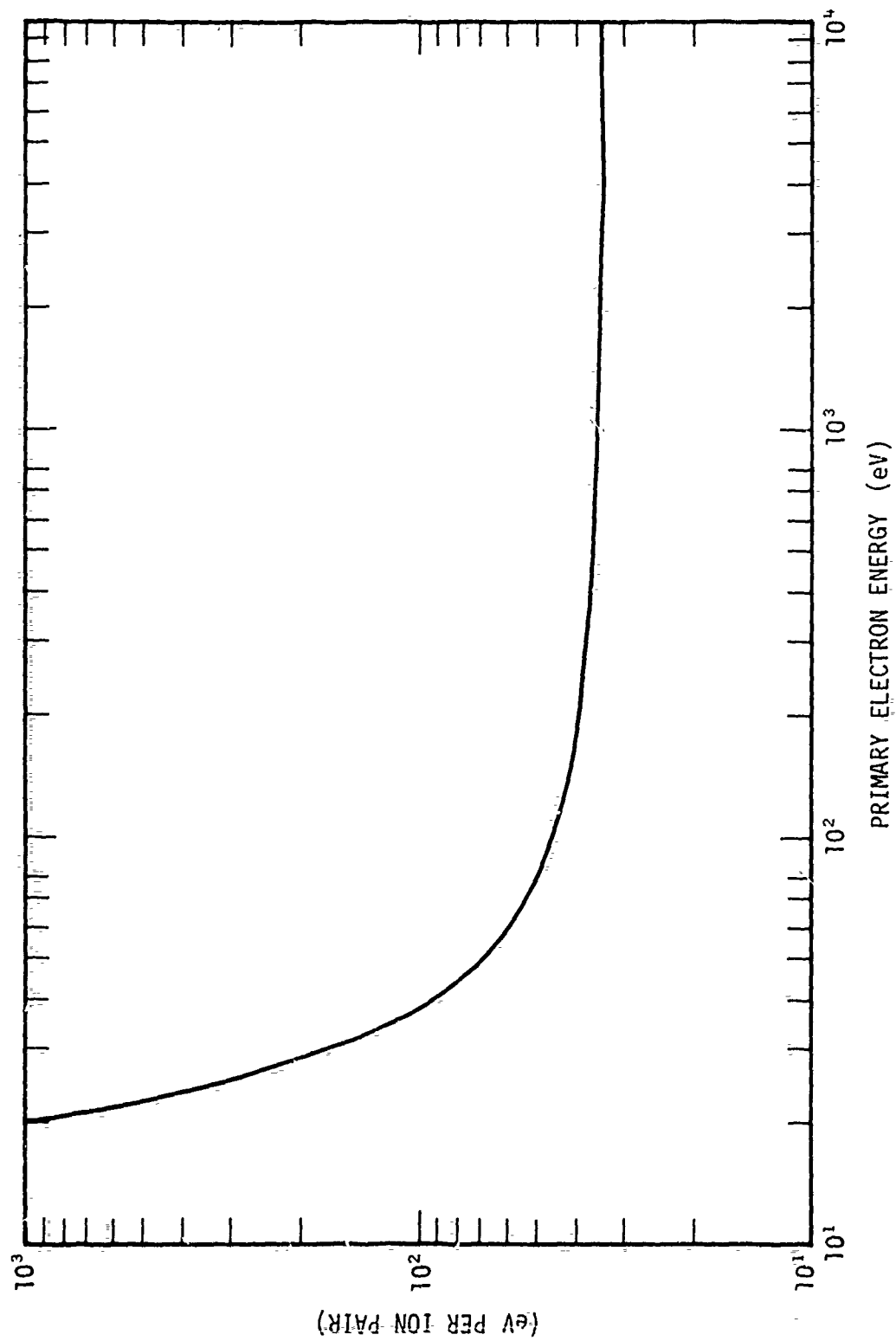
Figure 2-1. eV/ion pair in $N_2(79\%)/O_2(21\%)$ mixture calculated with the ARCTIC code.

at an altitude of 250 km, isotropic downward with a vertical magnetic field, determine the energy deposition rate as a function of altitude, and the volume production rate of selected states. The atmosphere specified was CIRA 1965, model 5, hour 0.

Figure 2-2 shows the calculated energy deposition rate profile. Shown for comparison (dashed curve) are the results obtained with the Lockheed (LMSC) code. They are seen to be in substantial agreement with those from the ARCTIC code. A study of the differences has shown that they arise almost entirely from differences in the assumed elastic scattering cross sections. Results obtained with the NRL and Visidyne codes were at variance with each other as well as with those in figure 2-2. They are not shown here.

Production rates for about 200 different excited states of N_2, O_2, N, and O were obtained. Figures 2-3 to 2-6 show a few selected results from the list. Comparison of these results with those from other codes was not made.

AURORAL ARC OF 27 MARCH 1973 (BLACK BRANT 18.205-1)

Preliminary Discussion

A considerable fraction of our effort has been devoted to a study of the auroral event of 27 March 1973, observed in the vicinity of Poker Flat, Alaska. Details of the event (an arc with brightness coefficient at least II+) were recorded by instruments on board a Black Brant rocket and by various ground-based instruments including those located at Ester Dome (EDO) and Fort Yukon (FYU), Alaska. All of the data obtained with these instruments are not yet reduced and available. The analyses and results reported below are based on the limited amount of preliminary data that was made available to us. We believe that a better model to describe the event, especially the auroral environment outside the main arc, can be constructed when all of the evidence is at hand.
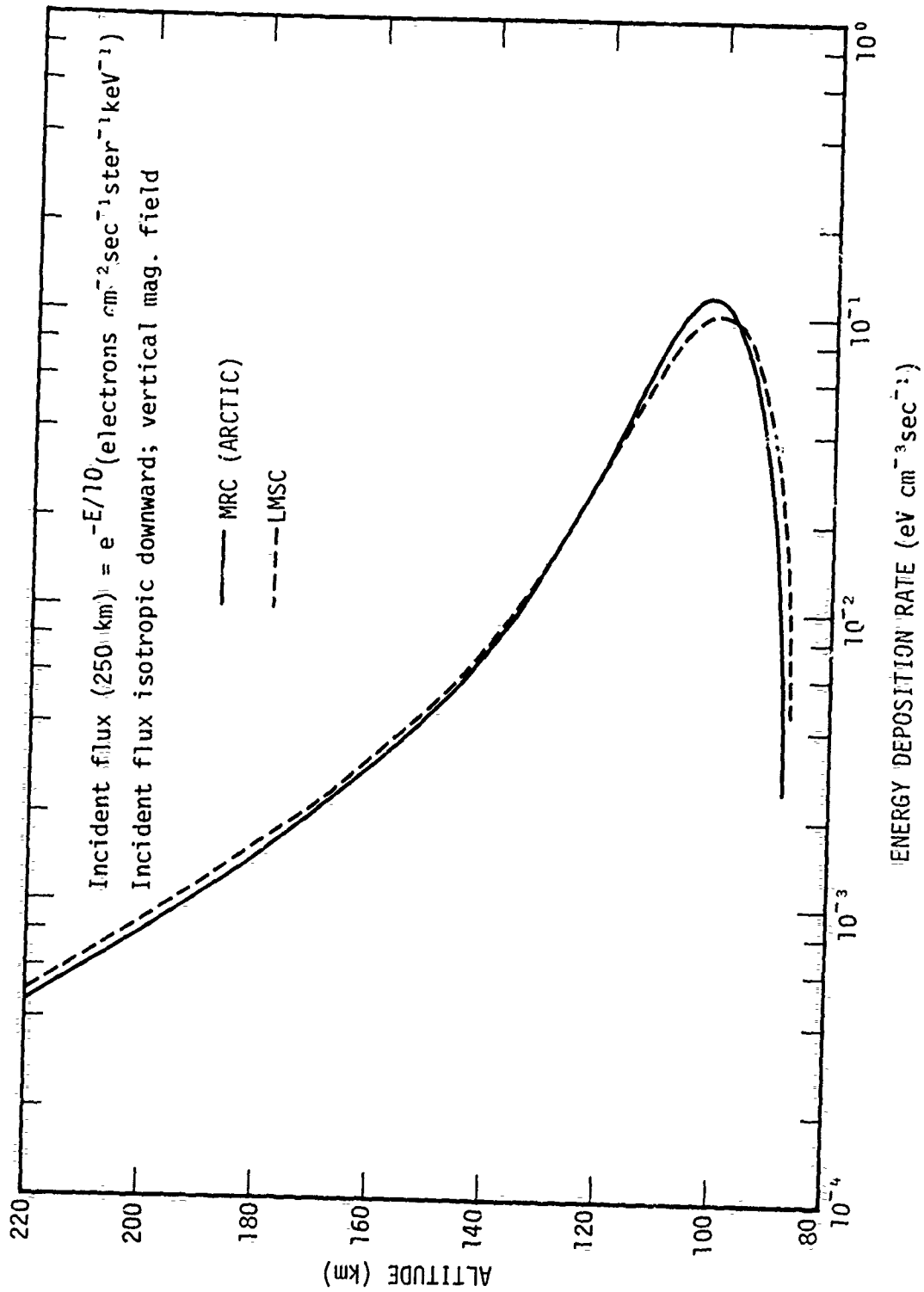
Figure 2-2. Calculated energy deposition rate for hypothetical electron flux.

Incident flux (250 km) = $e^{-E/10}$ (electrons $cm^{-2}sec^{-1}ster^{-1}keV^{-1}$)

Incident flux isotropic downward; vertical mag. field

——— MRC (ARCTIC)

– – – LMSC

ENERGY DEPOSITION RATE (eV $cm^{-3}sec^{-1}$)

ALTITUDE (km)
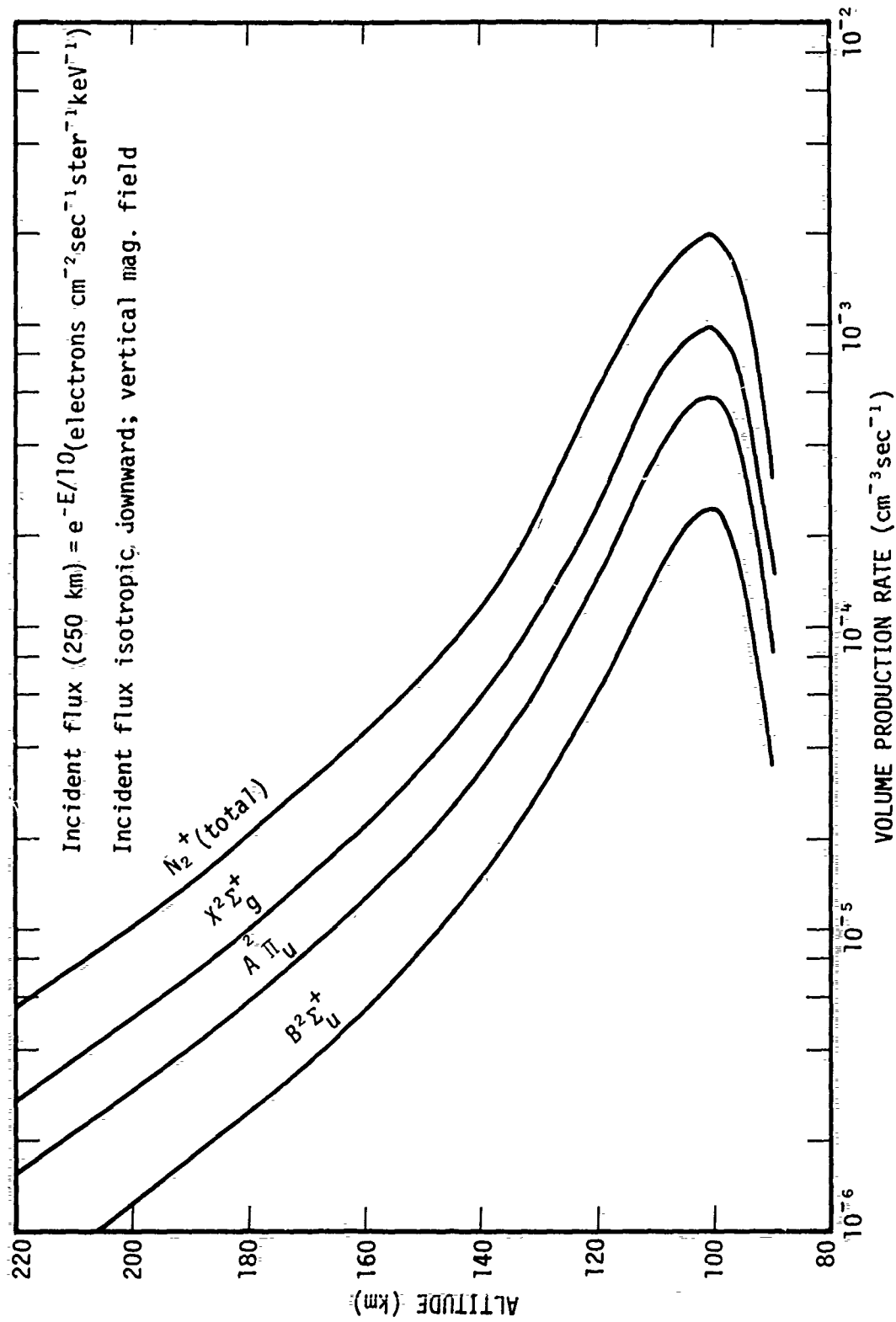
Figure 2-3. Volume production rates for selected state of N_2^+.

Incident flux (250 km) = $e^{-E/10}$(electrons $cm^{-2}sec^{-1}ster^{-1}keV^{-1}$)

Incident flux isotropic, downward; vertical mag. field

N_2^+ (total)

$X^2\Sigma_g^+$

$A^2\Pi_u$

$B^2\Sigma_u^+$

VOLUME PRODUCTION RATE ($cm^{-3}sec^{-1}$)

ALTITUDE (km)

For description of incident flux, see Figure 2-3.
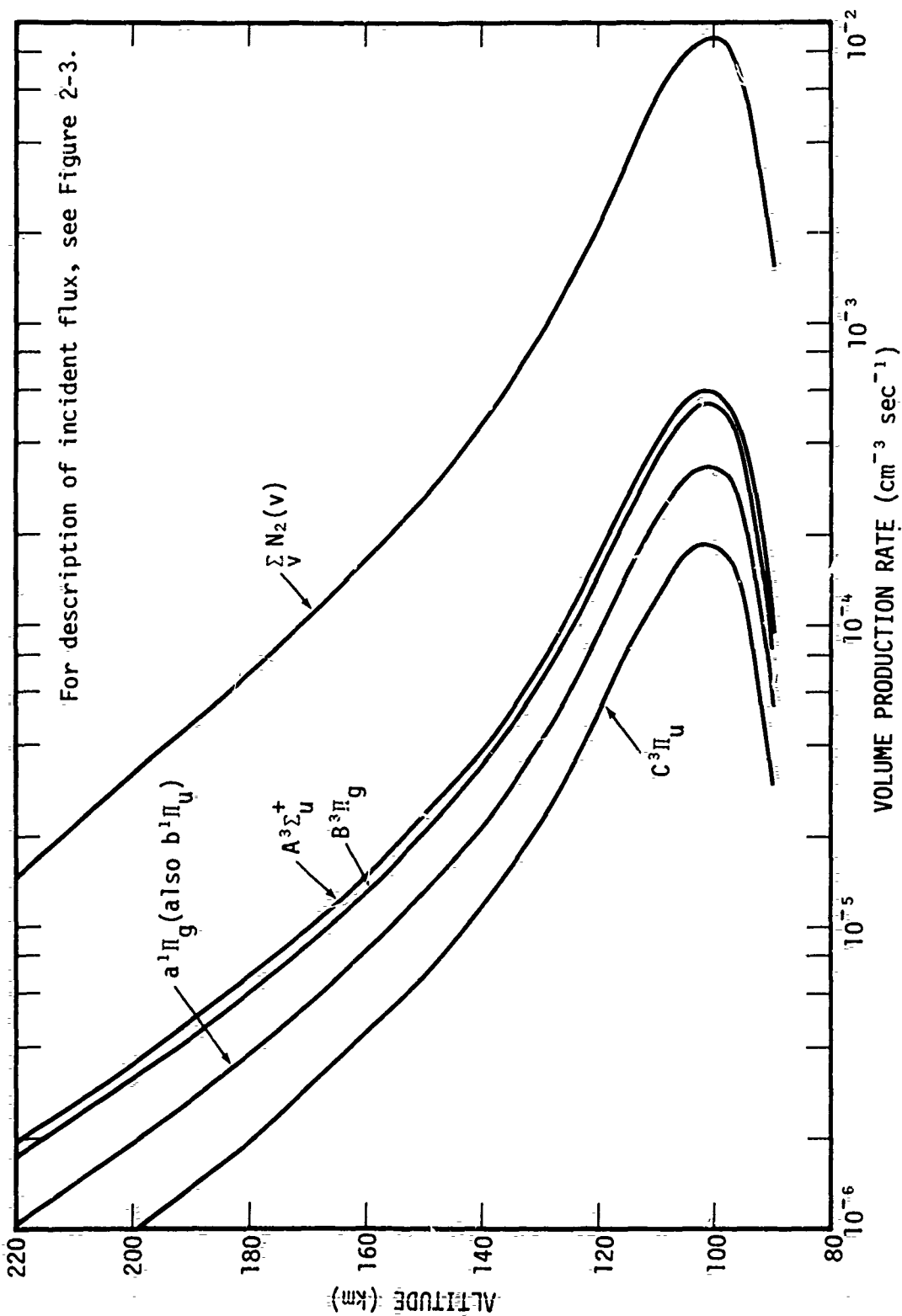
Figure 2-4. Volume production rates for selected states of N_2.

For description of incident flux, see Figure 2-3.
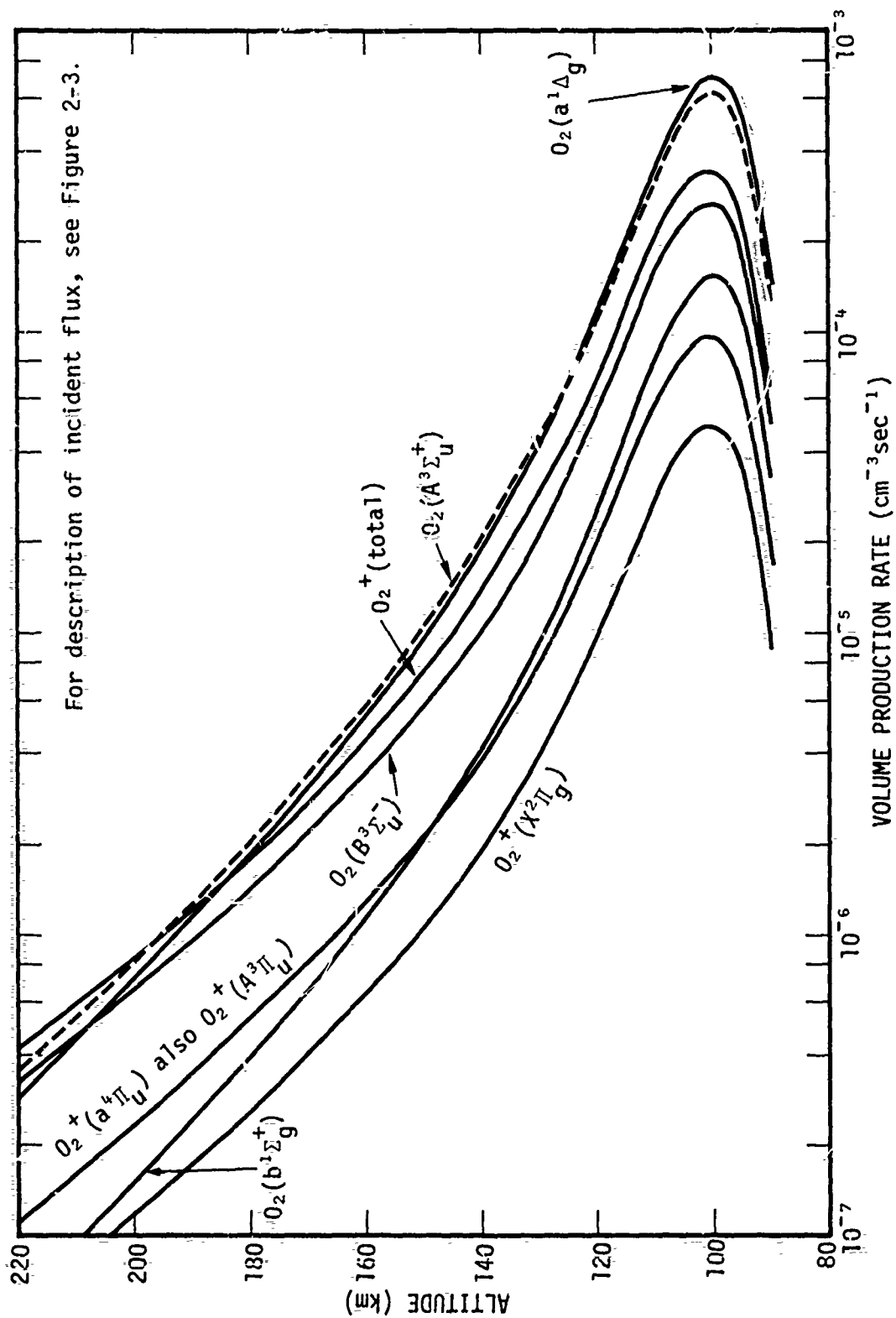
Figure 2-5. Volume production rates for selected states of O_2 and O_2^+.

23

For description of incident flux, see Figure 2-3.
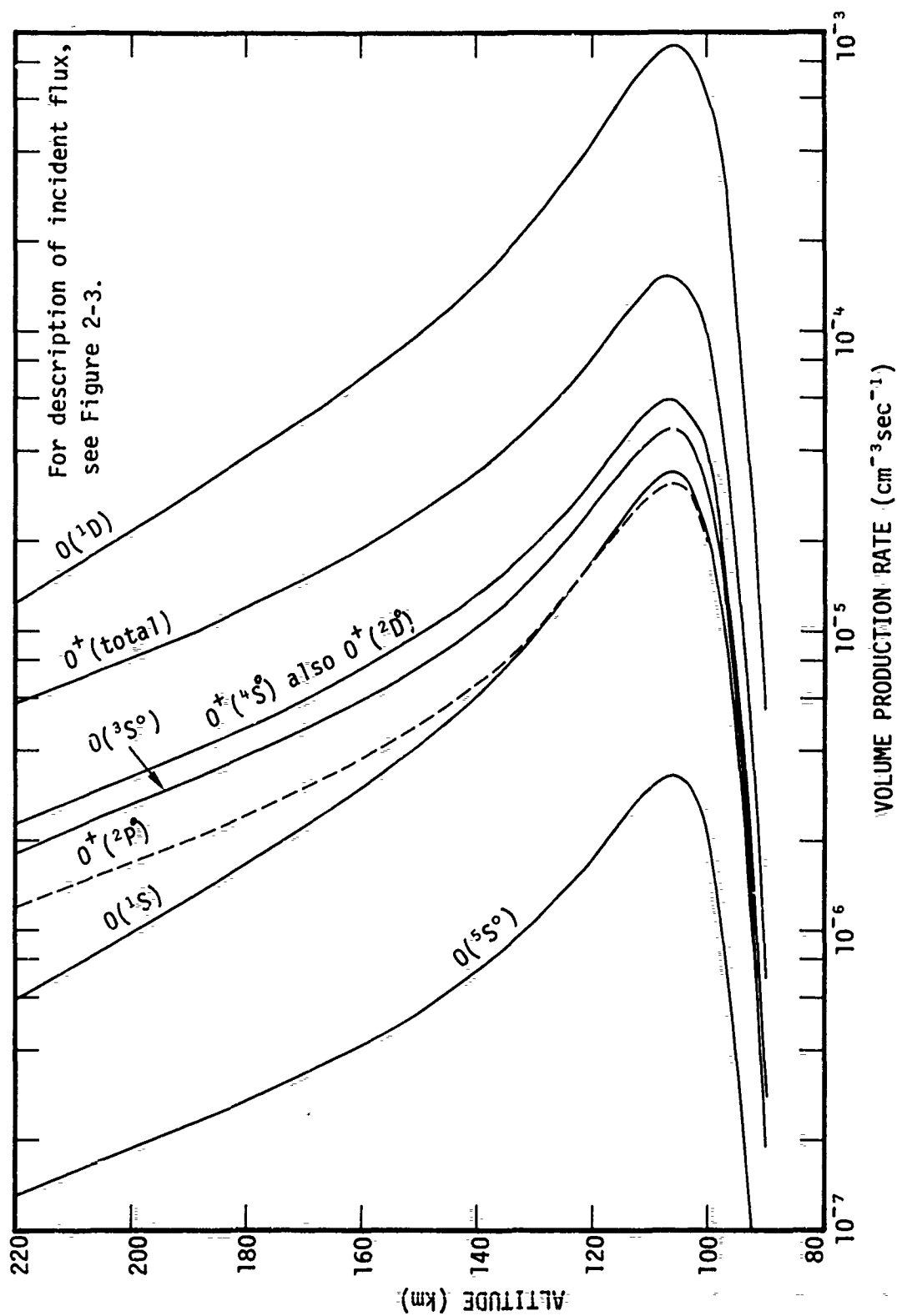
Figure 2-6. Volume production rates for selected states of O and O$^+$.

24

In this subsection we will first give a brief overview of the auroral event, together with a description of the types of data that were taken on it. Next we proceed to set the stage for actual calculations with the ARCTIC code by describing the environment into which the electron flux in the main arc is assumed to be deposited. This description includes a consideration of the relatively soft spectral flux of electrons, that we will call a "drizzle", that is believed to have bombarded the air over a large region for some time prior to the rocket launch. We next go on to deduce some geometrical and dynamical characteristics of the arc itself, and present the data used to describe the incident spectral flux. The calculations are then described and the results, together with data comparisons, are presented. Finally, some conclusions, based on the comparisons, are drawn.

Qualitative Description of Event

A Black Brant rocket (18.205-1) was launched from Poker Flat (PF), Alaska on 27 March 1973 at 0937:45 UT into a bright auroral arc. The geometrical arrangement, including the projection of the rocket trajectory in the magnetic meridian plane and the approximate position of the arc at 91 sec after rocket launch, is shown in Figure 2-7. Details concerning the rocket attitude and trajectory and the on-board instrumentation can be found in Reference 4. The geometry depicted in Figure 2-7 is based on information supplied to us by Photometrics (Reference 5). For altitudes above about 70 km, the rocket axis was nearly vertical, being inclined 3 degrees south (magnetic) from the zenith, and 10 degrees from the magnetic field lines.

Although the rocket was programmed to enter the arc at 100-km altitude, it actually entered between 105 and 110 km and overflew the region of maximum energy deposition (Reference 6). The on-board instrumentation that is relevant to this report included: (1) an electrostatic analyzer to

25
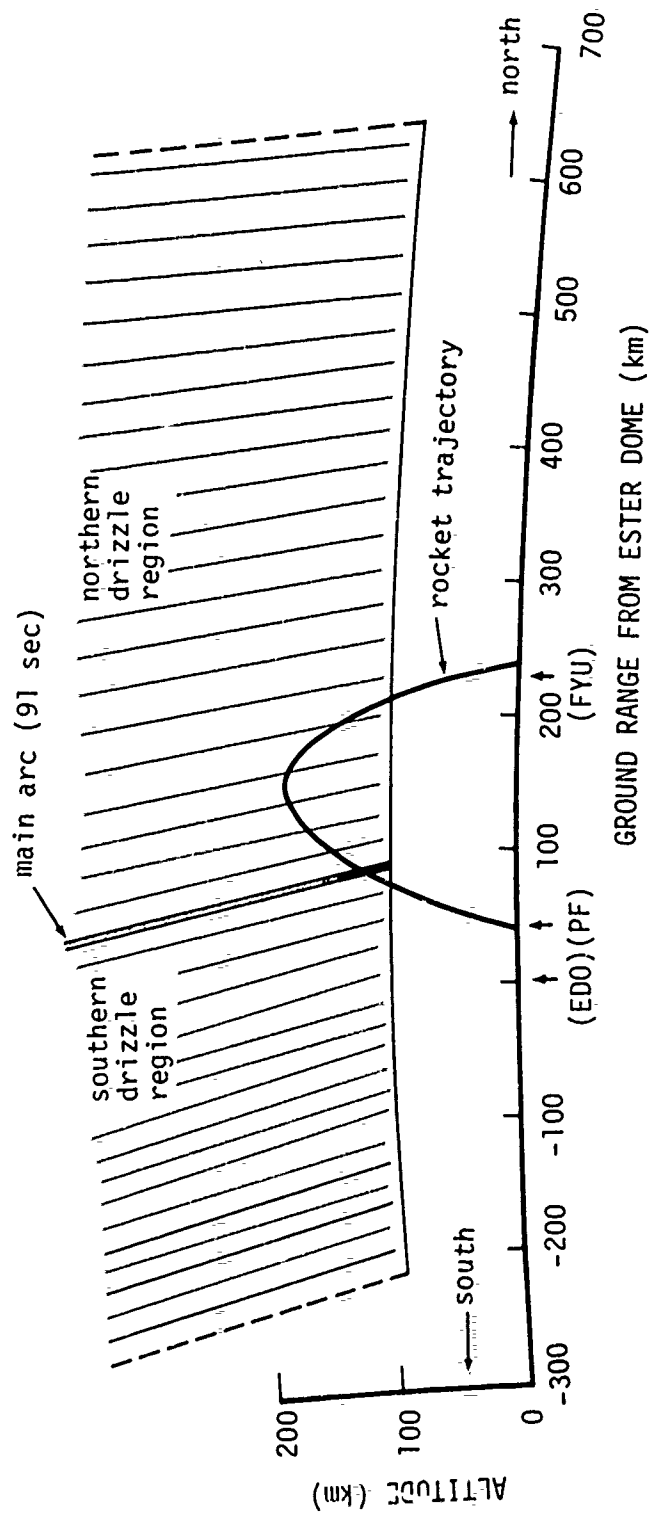
Figure 2-7. Pictorial representation in magnetic meridian plane showing rocket (B.B. 18.205-1) trajectory and assumed auroral environment.

measure the differential electron spectra over the energy range 3 to 30 keV,
(2) a scintillator to measure the energy deposited by electrons with energies
greater than about 3 keV, (3) a positive ion and neutral mass spectrometer,
(4) plasma frequency and Langmuir probes to measure the electron density,
(5) a vertical-viewing photometer at 3914 Å (in the rocket nose), (6) a
vertical-viewing dual channel radiometer at 4.3 and 5.4 μm, (7) a vertical-
viewing CVF spectrometer (8) a side-looking (80° from vertical) dual channel
radiometer at 2.7 and 5.4 μm, and (9) five side-looking (80° from vertical)
optical photometers at 3466 Å, 3800 Å, 3914 Å, 5199 Å, and 5577 Å.

Ground-based instrumentation included 4278 Å- and 5577 Å-scanning
photometers (scanning in the magnetic meridian plane) at Ester Dome and
Fort Yukon (see Figure 2-7) as well as all-sky cameras at both of these
locations.

The general position and motion of the arc, as deduced from the
scanning photometer data at Ester Dome and Fort Yukon (Reference 5) in the
time span from about 10 minutes before to 7 minutes after rocket launch is
as follows. At -10 minutes the arc was nearly overhead at Ester Dome.
It subsequently moved, rather erratically, northward until it reached Poker
Flat at about -9 minutes. It remained slightly north of that position
until about -6.5 minutes when it moved northward again and reached its
most northerly position (about halfway between Ester Dome and Fort Yukon)
at about -5 minutes. It then proceeded to move south until about 95 sec
after rocket launch (approximately the time the rocket entered the main
arc — when the arc was ~ 48 km north of Poker Flat) when it moved northward
again. An erratic movement northward continued until about +4.5 minutes,
at which time the arc was 70 km north of Poker Flat, and a generally south-
ward movement then ensued.

The foregoing description should serve to indicate that a large
air volume, including the measurement space itself, was bombarded sporadically

27

by the arc flux for some time prior to the rocket measurements. In fact, the point where the rocket first penetrated the arc had been irradiated previously at about -5.5 minutes as the arc moved northward through it.

Exo-Arc Environment

It is clear from the above discussion that the photometer- and radiometer-sight paths traversed regions outside the arc that had previously been irradiated in a complex and ill-defined manner. In order to make meaningful comparisons between ARCTIC-code calculations and the data, we have attempted to construct a mean exo-arc environment that may suffice for the purpose. This model environment will now be described.

The assumed initial neutral atmosphere (prior to any irradiation) is shown in Table 2-2.

Table 2-2. Assumed initial nighttime neutral atmosphere.

Quantity	Altitude Range (km)	Values
$[N_2]$, $[O_2]$, $[O]$, T	$\begin{cases} 80 \leq h \leq 120 \\ 120 \leq h \leq 800 \end{cases}$ *	1965 CIRA mean, p.12 1965 CIRA mean, mod.5, hr.0
$[O_3]$	≥ 30	4.5×10^{12} exp $[(30-h)/5.42]$
$[CO_2]$	< 100	3×10^{-4} [molecules]
	≥ 100	3×10^{-4} [molecules]exp$[(100-h)/17.4]$
$[NO]$	< 80	4×10^{-8} [molecules]
	$80 \leq h \leq 110$	4×10^{-8} [molecules]exp$[(h-80)/4.29]$
	> 110	4×10^{-8} [molecules]exp$[6.99+ (110-h)/43.5]$
* h is altitude in kilometers.		

28

The vibrational states of N_2 are assumed to be Boltzmann distributed initially, and the electron temperature is equated to that of the neutral gas.

An error in the assumed vertical distribution of the major species can lead to several sources of error in the calculated chemical and optical environment. Included among these, for example, are errors in the altitude profile of the energy deposition rate, in the energy partition as a function of altitude, and in the rate at which chemical reactions can proceed. Unfortunately, neutral mass spectrometer data for this event are not currently available to us and, consequently, the accuracy of our assumed profiles for the major species is certainly in question.

Considerable evidence is available to suggest that a weak particle bombardment is present in the auroral oval at all times (References 7, 8, 9). In particular, Walker et al., (Reference 8) have fit one set of observations with a bombarding flux of the form $E \exp(-E/0.6)$, isotropic over the lower hemisphere. Using these results, Jones and Rees (Reference 10) have calculated an "ambient" high-latitude nocturnal ionosphere. We have used their results to define relative concentrations for NO^+, O_2^+, and O^+, and have assumed an "ambient" ionospheric model by normalizing these results to those of Walker (Reference 11). Concentrations of all other species are initially set to zero.

The foregoing remarks describe the "ambient" high-latitude atmospheric model assumed. Into this environment must now be superimposed the modifications that arise from the intense, but localized, electron flux into the auroral arc, as well as that from the associated drizzle precipitation that extends well beyond the arc.

The work of Frank and Ackerson (Reference 9) shows that the particle flux outside an arc is associated in a complex way with that of

the arc itself. It is generally not a constant in space but shows considerable structure of the "inverted-V" type. That is, the hardness and strength of the particle spectrum tends to fall off with distance north and south from the arc proper. The arc and its surrounding flux (that may extend for hundreds of kilometers north and south of the arc) evidently constitute a unified event. For convenience we shall refer to the localized region of intense precipitation as the "main arc", and the larger region of complex but weaker precipitation as the "drizzle" region.

Since the main arc generally moves within the drizzle region we shall, for calculational purposes, assume that the two regions are essentially independent and that the drizzle flux serves to determine the background environment into which the main arc flux is deposited.

The only particle flux data available for the drizzle region are those obtained over that part of the rocket trajectory outside the main arc (see Figure 2-7). Samples of such data (Reference 6), corresponding to various times after rocket launch, are shown in Figure 2-8.[*] For calculational simplicity, we have adopted an "average" drizzle flux spectrum shown by the dashed curve in Figure 2-8, and assume that the precipitation is isotropic (in pitch angle) in the downward hemisphere. The adopted spectrum was normalized so as to provide agreement with the measured 4278 $\overset{\circ}{A}$ zenith brightness at Fort Yukon. This flux is assumed to be constant in space and time preceding and during the rocket flight, although the assumption is clearly at variance with the general findings of Frank and Ackerson mentioned above. For this reason we cannot hope to achieve precise agreement with the data from some of the side-looking instruments on board the rocket (especially the 5199 $\overset{\circ}{A}$ and 3466 $\overset{\circ}{A}$ emissions from $N(^2D)$ and $N(^2P)$, respectively) that depend rather sensitively on details of the drizzle.

---

[*] These spectra show many of the characteristics of an intense "inverted V" structure, particularly the progressive softening and weakening of the spectrum as a function of distance from the main arc.
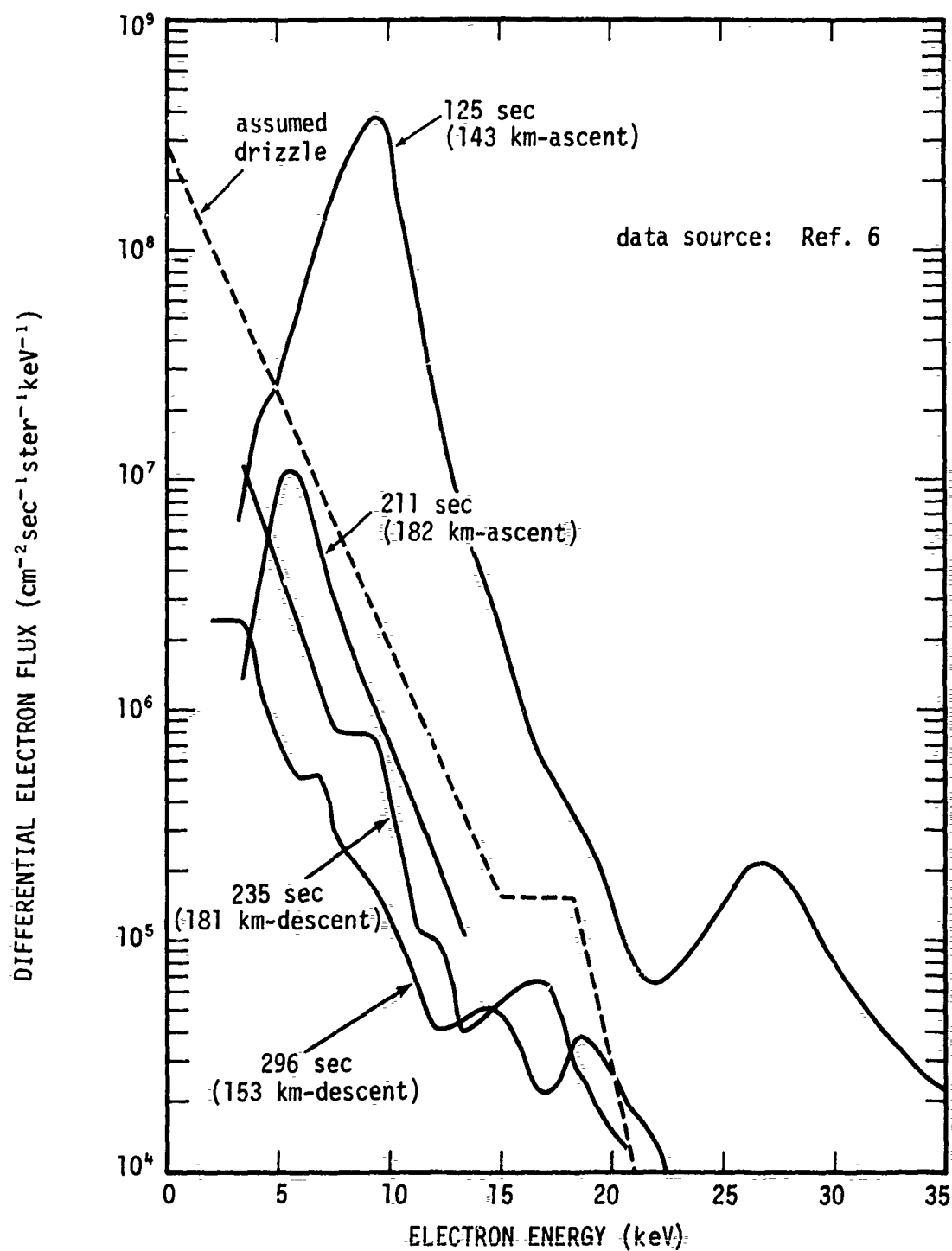
Figure 2-8. Assumed drizzle spectrum compared with rocket (Black Brant 18.205-1) data outside arc.

31

Rather, in these cases, the object is to account for the general magnitude of the observed emissions which, in the absence of an assumed drizzle, we would not otherwise be able to do.

In addition to providing a drizzle spectrum, it is also necessary to specify the time over which it has operated and its spatial extent. Little information is available on the effective duration of the drizzle bombardment, although data from the side-looking photometers on board the rocket provide some guide as to its spatial extent. With respect to the bombardment time, however, we note that for some ten days preceding the event, significant magnetic disturbances with K_p indices ranging from 4 to 7 occurred (Reference 12). In addition, ground-based photometer data (Reference 5) show that a drizzle bombardment probably occurred for at least 1½ hours before rocket launch.

In order to determine the effect on species concentrations due to a long term drizzle precipitation, we ran the ARCTIC code with the drizzle spectrum shown in Figure 2-8 (dashed curve) for times to 10^6 sec. Figures 2-9 and 2-10 show the resulting profiles of O_2, O, and NO for selected drizzle duration times. The results clearly show an NO buildup, especially for 10^6 sec (11.5 days), along with an increase in [O] and a decrease in $[O_2]$. Since the effects due to diffusion, transport, and daytime solar radiation are not included in the calculation, the late-time results are not realistic. However, they do serve to indicate the type of chemical effects that can arise from prolonged bombardment.

Large enhancement of the NO concentration in an auroral environment has been reported by Zipf (Reference 13), and has also been inferred from numerous ion mass spectrometer measurements (eg., References 14, 15). In fact, for the auroral event considered here, we have inferred an enhanced

32
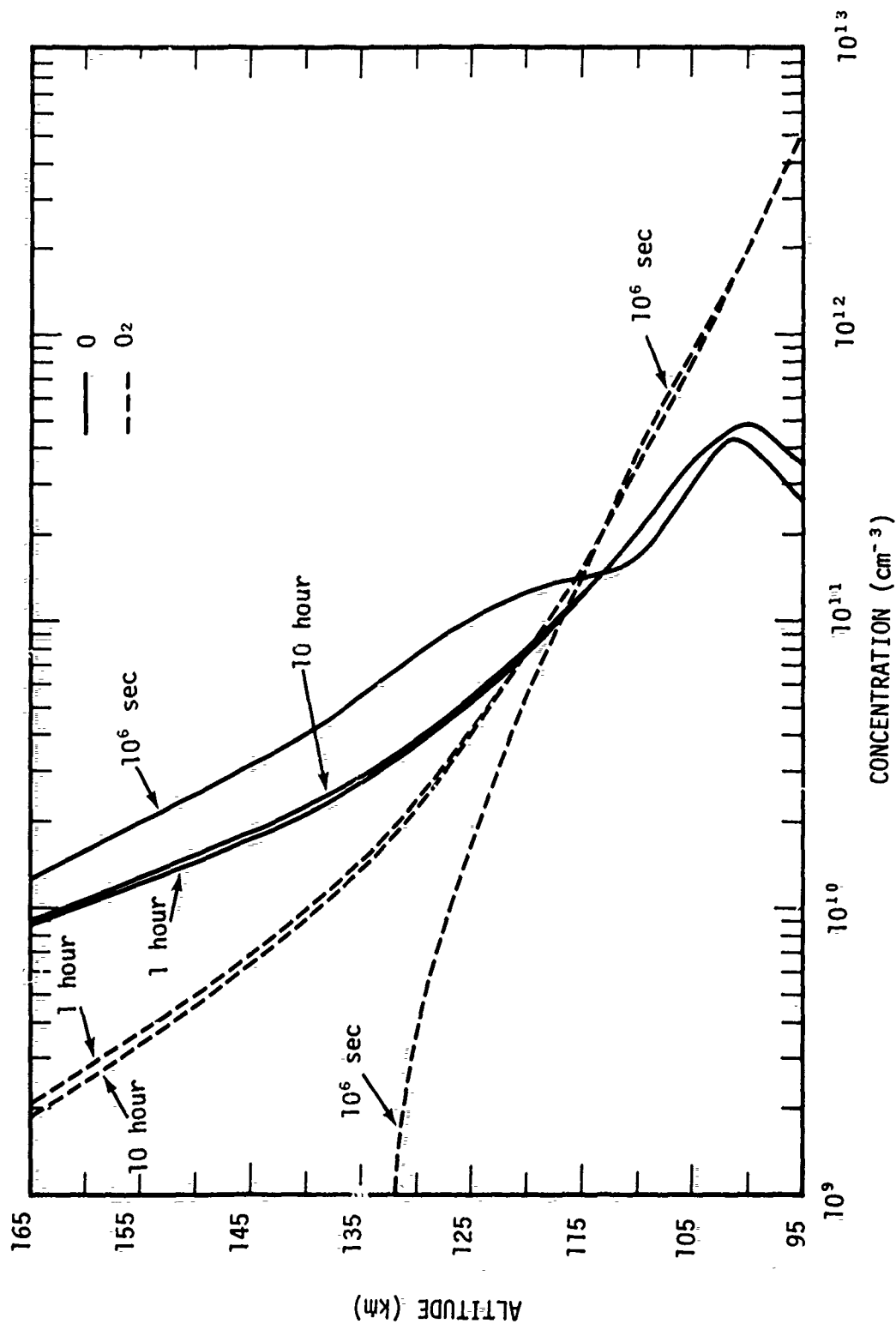
Figure 2-9. Calculated profiles of $[O_2]$ and $[O]$ for selected duration times of drizzle bombardment.

33
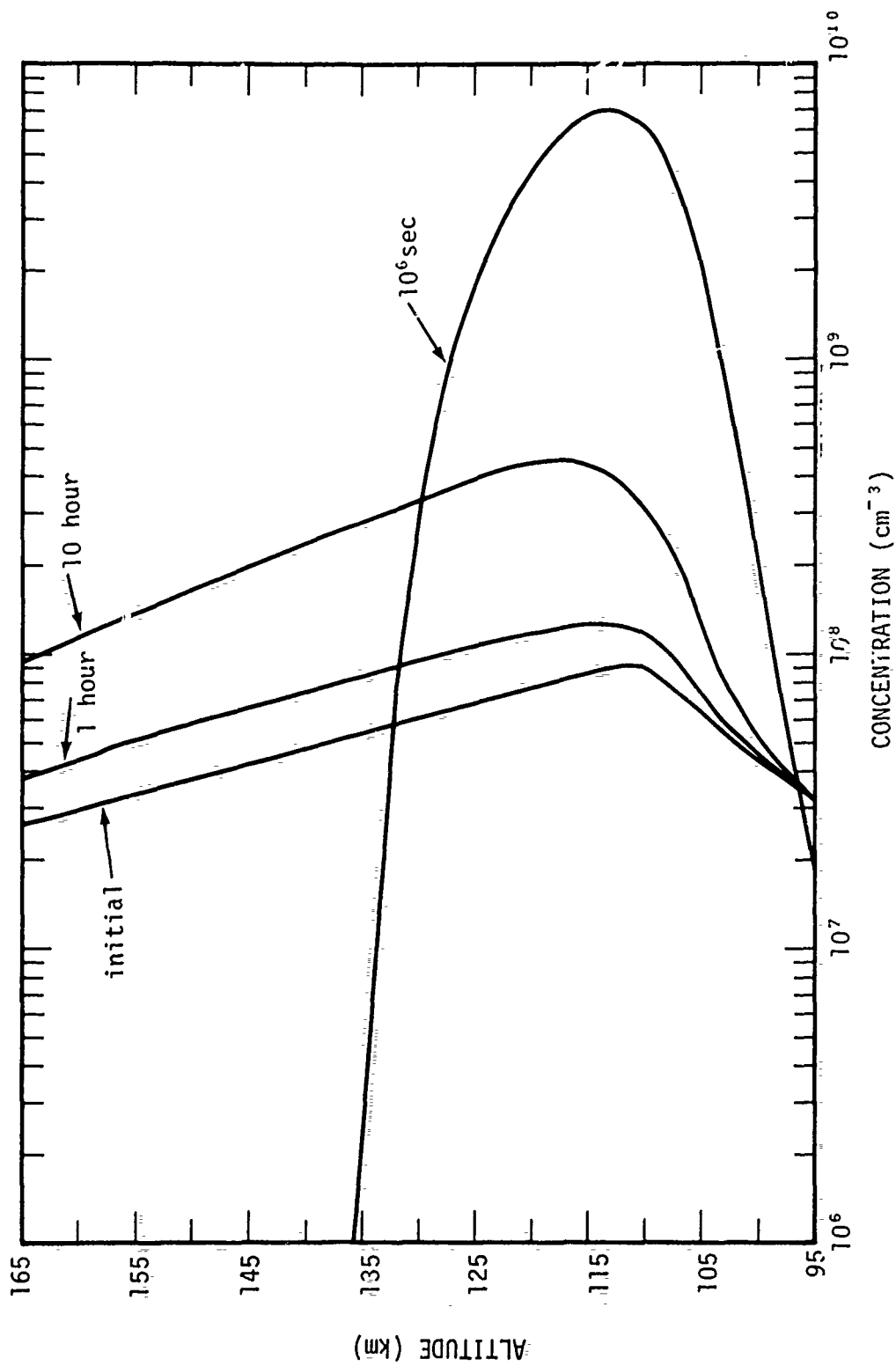
Figure 2-10. Calculated profiles of [NO] for selected duration time of drizzle bombardment.

NO profile using the positive ion mass spectrometer data of Narcisi (Reference 16) and a procedure similar to that described by Swider and Narcisi (Reference 15). Because of rocket spin modulation, the mass spectrometer data show large fluctuations (see Figure 2-39), and the inferred NO profile reflects this ambiguity. However, Figure 2-11 shows an NO profile that is not inconsistent with the mass spectrometer data.[*] Shown for comparison is a measured low latitude profile (References 17, 18). The comparison suggests that the NO concentration in the vicinity of the auroral arc was greatly enhanced above its low latitude values, at least below about 120 km, and attains values $\sim 2 \times 10^9$ cm^{-3} between 100- and 105-km altitude.

In preparing an environment in which to deposit the main arc flux, we have, somewhat arbitrarily, assumed: (1) the drizzle flux is turned on 30 minutes prior to rocket launch, (2) all concentrations, with the exception of NO, are initially specified by the high-latitude "ambient" model described earlier, (3) the NO profile is given initially by the enhanced values shown in Figure 2-11.

Unfortunately, as indicated earlier, errors in the assumed concentrations of O_2, O, and NO can lead to significant differences between the computed and measured environment. For example, the ion concentration ratios, especially NO^+/O_2^+, are sensitive to the NO profile, and detailed agreement between calculations and observations should not be expected in the absence of good data on [NO].

With the foregoing assumptions, the perturbed atmosphere (resulting from 30 minutes of drizzle bombardment) into which the main arc flux is deposited, is shown in Table 2-3.

---

[*] Actually, the inferred values for NO are higher above 120 km than are shown in Figure 2-11. For simplicity, we have extrapolated the enhanced profile above 120 km until it intersects the low latitude curve.

35
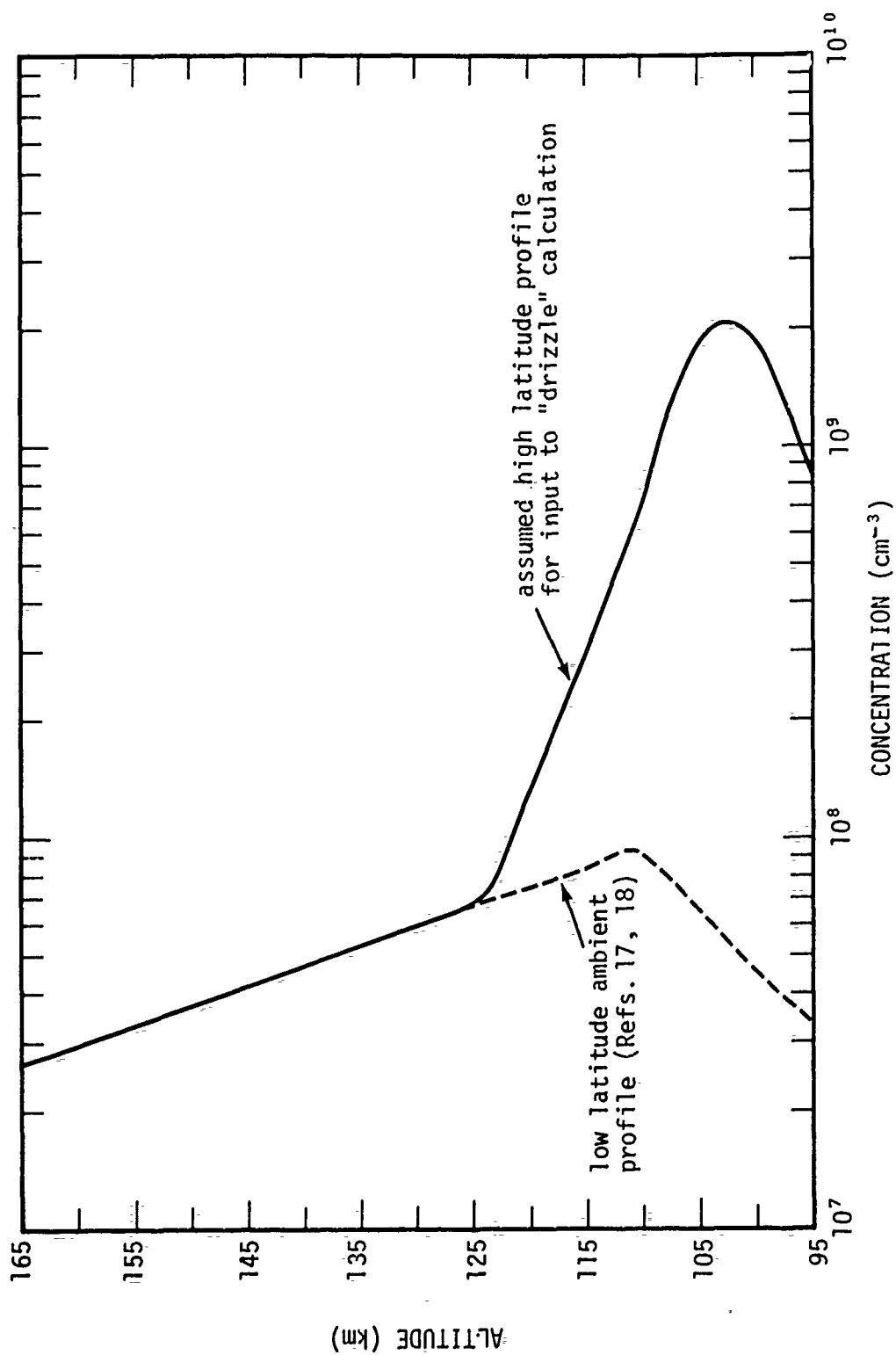
Figure 2-11. Assumed low and high latitude profiles for [NO].

Table 2-3. Perturbed atmosphere following 30 minutes of "drizzle" bombardment.

ALTITUDE (km)	N_2	N_2^+	$N(^4S)$	$N(^2D)$	$N(^2P)$	$N^+(^3P)$	$N^+(^2D)$	$N^+(^1S)$	O_2	$O_2(^1\Delta)$	O_2^+	$O(^3P)$	$O(^1D)$
96.0	1.64^{13}	0	1.69^2	0	0	0	0	0	4.3^{12}	6.5^7	4.0^0	3.9^{11}	0
97.6	1.25^{13}	0	1.13^3	$4.^0$	0	0	0	0	3.18^{12}	4.28^7	2.55^1	4.15^{11}	0
99.3	9.21^{12}	1.7^0	4.78^3	4.95^1	0	0	0	0	2.28^{12}	2.68^7	2.76^2	4.74^{11}	0
101.3	6.58^{12}	5.5^0	1.21^4	1.83^2	2.1^0	0	0	0	1.58^{12}	1.37^7	6.13^2	4.60^{11}	2.3^0
103.5	4.54^{12}	1.68^1	2.89^4	6.14^2	6.9^0	0	0	0	1.06^{12}	6.88^6	1.28^3	3.99^{11}	6.78^0
105.9	3.06^{12}	4.95^1	8.00^4	2.20^3	2.23^1	1.6^0	0	0	6.95^{11}	4.52^6	3.24^3	3.27^{11}	2.32^1
108.5	2.04^{12}	1.29^2	2.47^5	6.14^3	6.61^1	4.2^0	1.9^0	0	4.99^{11}	4.30^6	9.27^3	2.39^{11}	6.49^1
111.5	1.30^{12}	2.80^2	5.19^5	1.39^4	1.44^2	9.1^0	4.0^0	0	2.75^{11}	4.40^6	1.75^4	1.74^{11}	1.49^2
114.8	7.89^{11}	4.88^2	1.21^6	2.64^4	2.71^2	1.69^1	7.4^0	1.3^0	1.60^{11}	4.06^6	3.33^4	1.27^{11}	2.96^2
118.4	4.92^{11}	7.76^2	2.22^6	4.40^4	4.55^2	2.85^1	1.3^1	2.1^0	9.45^{10}	3.68^6	5.00^4	8.93^{10}	5.08^2
122.5	3.09^{11}	1.14^3	3.61^6	6.76^4	7.01^2	4.45^1	1.96^1	3.1^0	5.65^{10}	3.14^6	6.56^4	6.34^{10}	8.04^2
127.0	1.90^{11}	1.53^3	3.98^6	9.86^4	9.91^2	6.44^1	2.85^1	4.4^0	3.31^{10}	2.43^6	6.65^4	4.50^{10}	1.17^3
131.9	1.17^{11}	1.91^3	3.51^6	1.38^5	1.30^3	8.62^1	3.93^1	5.8^0	1.94^{10}	1.77^6	5.85^4	3.22^{10}	1.60^3
137.5	7.63^{10}	2.29^3	3.20^6	1.84^5	1.62^3	1.16^2	5.20^1	7.3^0	1.21^{10}	1.32^6	5.31^4	2.41^{10}	2.11^3
143.6	5.01^{10}	2.65^3	2.93^6	2.41^5	1.93^3	1.50^2	6.76^1	8.8^0	7.60^9	9.73^5	4.82^4	1.82^{10}	2.74^3
150.4	3.33^{10}	2.96^3	2.75^6	3.02^5	2.16^3	1.87^2	8.54^1	1.02^1	4.81^9	6.99^5	4.41^4	1.39^{10}	3.44^3
158.0	2.22^{10}	3.17^3	2.59^6	3.68^5	2.25^3	2.27^2	1.05^2	1.12^1	3.07^9	4.88^5	4.02^4	1.07^{10}	4.22^3
166.4	1.48^{10}	3.31^3	2.48^6	4.35^5	2.21^3	2.71^2	1.28^2	1.17^1	1.95^9	3.32^5	3.68^4	8.29^9	5.11^3
175.7	9.75^9	3.38^3	2.38^6	5.06^5	2.02^3	3.20^2	1.55^2	1.17^1	1.22^9	2.20^5	3.38^4	6.41^9	6.14^3
186.1	6.33^9	3.64^3	2.48^6	6.08^5	1.87^3	4.03^2	2.00^2	1.18^1	7.53^8	1.51^5	3.26^4	4.93^9	7.92^3

Table 2-3 (Continued). Perturbed atmosphere following 30 minutes of "drizzle" bombardment.

ALTITUDE (km)	O(¹S)	O⁺(⁴S)	O⁺(²D)	O⁺(²P)	NO	NO⁺	O₃	NO₂	N₂(v=1)	N₂(v=2)	N₂(v=3)	N₂(A³Σ)	O₂(b¹Σ)	Tₑ(°K)
96.0	7.23^{1}	0	0	0	1.00^{9}	2.08^{3}	2.88^{7}	3.92^{4}	1.27^{6}	1.05^{1}	3.2^{0}	0	7.2^{0}	201
97.6	9.86^{1}	0	0	0	1.40^{9}	6.18^{3}	1.57^{7}	5.14^{4}	3.04^{5}	2.31^{2}	1.08^{2}	2.4^{0}	6.95^{1}	204
99.3	1.41^{2}	0	0	0	1.80^{9}	2.74^{4}	7.95^{6}	6.18^{4}	1.30^{6}	1.16^{3}	5.61^{2}	1.1^{1}	2.49^{2}	207
101.3	1.53^{2}	$2.^{0}$	0	0	2.00^{9}	4.56^{4}	3.64^{6}	6.12^{4}	4.09^{6}	3.96^{3}	1.93^{3}	3.40^{1}	4.04^{3}	215
103.5	1.72^{2}	7.6^{0}	0	0	2.00^{9}	7.03^{4}	1.54^{6}	5.31^{4}	1.25^{7}	1.26^{4}	6.19^{3}	1.03^{2}	8.35^{3}	225
105.9	3.11^{2}	2.73^{1}	0	0	1.71^{9}	1.11^{5}	6.60^{5}	3.89^{4}	3.60^{7}	3.89^{4}	1.92^{4}	2.98^{2}	1.91^{4}	239
108.5	5.90^{2}	7.91^{2}	0	0	1.01^{9}	1.53^{5}	3.41^{5}	1.96^{4}	8.61^{7}	1.00^{5}	4.83^{4}	7.45^{2}	3.49^{4}	262
111.5	9.27^{2}	1.96^{2}	1.7^{0}	0	6.85^{8}	1.92^{5}	1.60^{5}	1.02^{4}	1.49^{8}	2.04^{5}	9.43^{4}	1.44^{3}	4.92^{4}	306
114.8	1.19^{3}	4.28^{2}	3.3^{0}	1.0^{0}	3.39^{8}	2.15^{5}	4.82^{4}	3.50^{3}	1.95^{8}	3.41^{5}	1.49^{5}	2.24^{3}	5.66^{4}	380
118.4	1.32^{3}	8.16^{2}	5.8^{0}	2.0^{0}	1.91^{8}	2.32^{5}	1.09^{4}	1.40^{3}	2.28^{8}	5.15^{5}	2.10^{5}	3.16^{3}	5.75^{4}	487
122.5	1.32^{3}	1.47^{3}	9.2^{0}	3.3^{0}	1.12^{8}	2.47^{5}	9.99^{2}	5.54^{2}	2.52^{8}	7.16^{5}	2.63^{5}	3.97^{3}	5.41^{4}	640
127.0	1.17^{2}	2.49^{3}	1.41^{1}	5.3^{0}	8.44^{7}	2.58^{5}	4.79^{1}	2.80^{2}	2.89^{8}	1.01^{6}	2.97^{5}	4.39^{3}	4.59^{4}	823
131.9	9.71^{2}	3.97^{3}	2.05^{1}	8.1^{0}	7.47^{7}	2.61^{5}	4.2^{0}	1.76^{2}	3.30^{8}	1.52^{6}	3.26^{5}	4.41^{3}	3.67^{4}	1000
137.5	8.10^{2}	5.99^{3}	2.89^{1}	1.18^{1}	6.57^{7}	2.57^{5}	0	1.18^{2}	3.67^{8}	2.44^{6}	3.58^{5}	4.26^{3}	2.99^{4}	1152
143.6	6.66^{2}	8.82^{3}	4.02^{1}	1.69^{1}	5.66^{7}	2.49^{5}	0	8.10^{1}	3.78^{8}	3.51^{6}	4.00^{5}	3.95^{3}	2.42^{4}	1309
150.4	5.37^{2}	1.26^{4}	5.45^{1}	2.34^{1}	4.79^{7}	2.37^{5}	0	5.61^{1}	3.79^{8}	5.10^{6}	4.59^{5}	3.49^{3}	1.91^{4}	1478
158.0	4.29^{2}	1.73^{4}	7.25^{1}	3.15^{1}	3.95^{7}	2.17^{5}	0	3.95^{1}	3.37^{8}	5.95^{6}	5.23^{5}	2.96^{3}	1.49^{4}	1608
166.4	3.35^{2}	2.35^{4}	9.57^{1}	4.19^{1}	3.18^{7}	1.97^{5}	0	2.78^{1}	2.92^{8}	6.57^{6}	6.09^{5}	2.43^{3}	1.13^{4}	1757
175.7	2.61^{2}	3.17^{4}	1.27^{2}	5.51^{1}	2.50^{7}	1.76^{5}	0	1.95^{1}	2.43^{8}	6.96^{6}	7.38^{5}	1.93^{3}	8.49^{3}	1936
186.1	2.15^{2}	4.59^{4}	1.82^{2}	7.78^{1}	1.92^{7}	1.61^{5}	0	1.37^{1}	2.04^{8}	8.00^{6}	1.09^{6}	1.60^{3}	6.72^{3}	2171

As to the spatial extent of the drizzle region, we have made
estimates based on comparisons between calculations and data from the side-
looking rocket-borne photometers and the ground-based 4278 $\overset{\circ}{A}$ instruments.
The result of these comparisons, as shown in Figure 2-7, suggests a drizzle
region extending about 310 km south and 540 km north from the main arc, for
a total north-south extent of about 850 km. The reasonableness of this
conclusion may be judged by comparing it with the previously cited work of
Frank and Ackerson (Reference 9) on other auroral events. They show three
sets of data (Plates 4a, 4b, and 5a) corresponding to K_p indices of 4-,
4, and 4+. For these events, the north-south extent of the associated
drizzle was 800, 1200, and 1400 km, respectively. At the time of the rocket
flight considered here (27 March 1973), a K_p value of about 4 appears to
be appropriate (Reference 12). The inferred extent of our drizzle, therefore,
is not inconsistent with these other auroral data.

Arc Geometry and Dynamics

To proceed farther, the geometry and velocity of the main arc
must be determined as well as the relationship between the arc and the
rocket- and ground-based instruments.

Visual inspection of the flight records of the electrostatic
analyzer reveals several important points concerning the geometry. At
about 91 sec the rocket entered a region of intense particle precipitation
and then left it at about 121 sec. Two typical plots of the measured flux
spectrum (Reference 6) during this time span are shown in Figure 2-12.
The time required to enter and leave this region was very short, indicating
sharp spatial boundaries.

Knowing the altitude at which the rocket entered and left the
arc, we can then determine the horizontal width, ΔW, of the arc (north-south

39
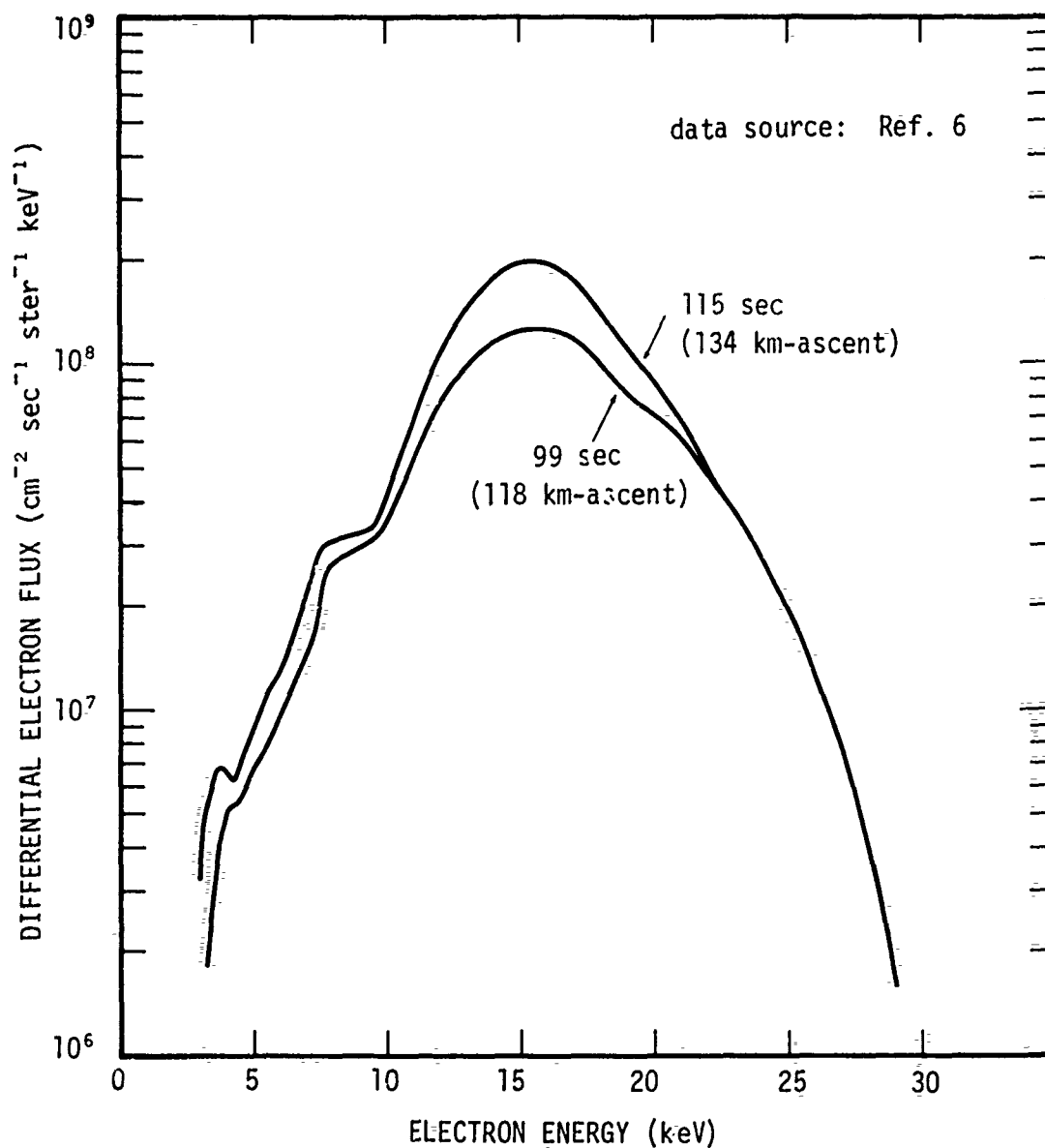
Figure 2-12. Measured electron flux inside arc (Black Brant 18.205-1).

dimension) if the horizontal component of the relative velocity between the arc and the rocket in the magnetic meridian plane is known. In particular,

$$\Delta W = \Delta h / \tan \delta + \int_{91}^{121} V_r \, dt \qquad (2\text{-}1)$$

where Δh is the altitude difference between the points of rocket entry to and exit from the main arc, δ is the magnetic dip angle ($77°$), and V_r is the horizontal component of the relative velocity in the magnetic meridian plane. From the rocket trajectory data supplied to us (Reference 6), Equation 2-1 becomes, for constant V_r,

$$\Delta W \simeq 7.1 + 30 \, V_r \qquad (km) \qquad . \qquad (2\text{-}2)$$

An estimate of the relative velocity, V_r, can be obtained using radiance data from the upward-viewing 3914 $\overset{o}{A}$ photometer in the rocket nose. This is shown in Figure 2-13 along with several simulations of this emission for rocket altitudes below 110 km. Inspection of Figure 2-13 shows that the slope of the calculated radiance values below 110 km is very sensitive to the assumed relative velocity. We have concluded that a value $V_r \simeq -0.07$ km sec^{-1} best fits the data. This implies an average arc velocity northward of 0.61 km sec^{-1}, slightly faster than that of the rocket itself and, from Equation 2-2, a horizontal arc width of 5 km.

It should be emphasized that the deduced arc motion is valid, at best, only over a very limited time span. In fact, the general description given earlier of the arc motion prior to rocket launch indicated that the main arc was actually moving south just prior to the time interval considered here. However, for the time period considered, the deduced arc velocity is in approximate agreement with the ground-based photometer data (Reference 5).
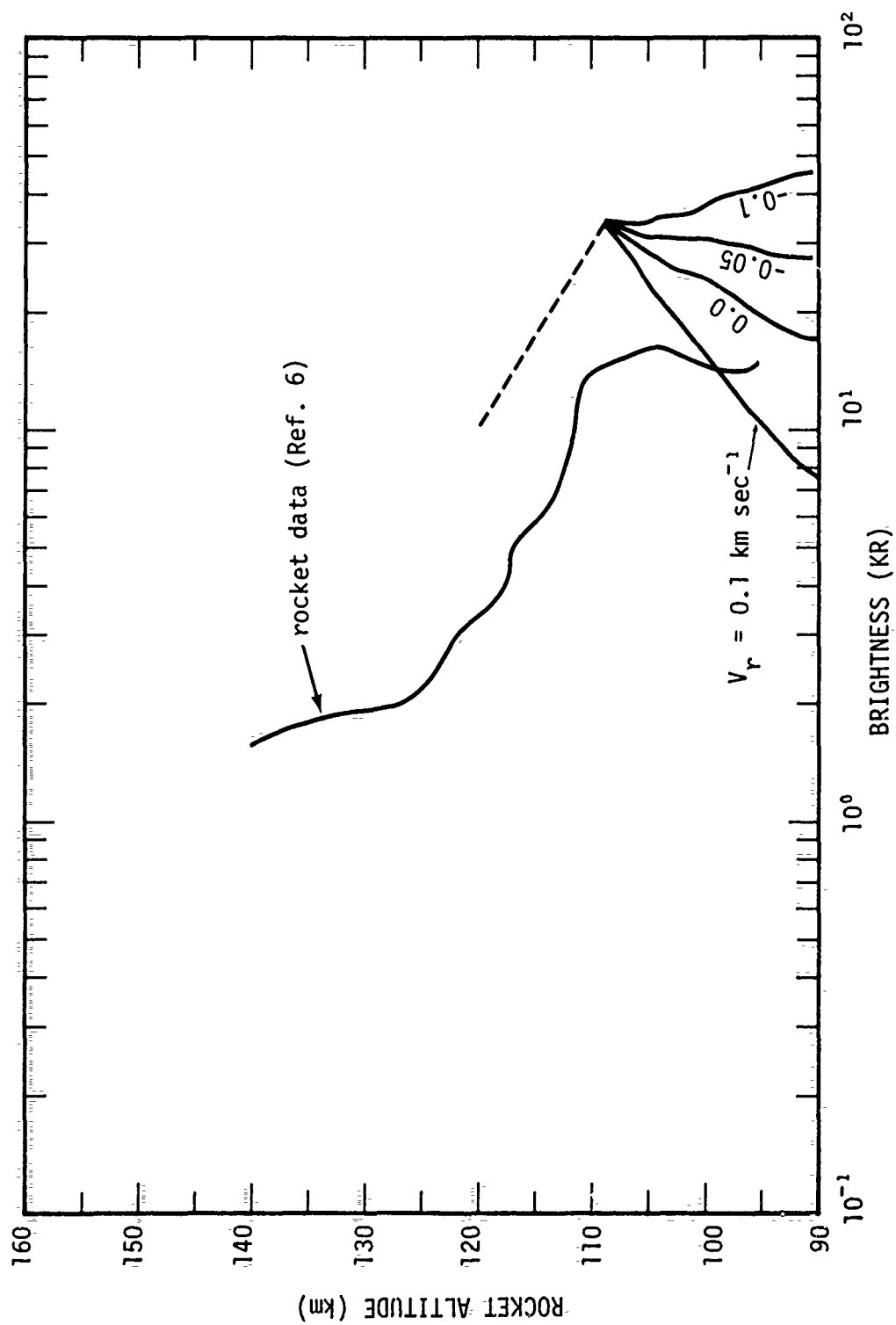
Figure 2-13. Calculated zenith brightness at rocket altitude below 110 km for selected values of V_r (flux spectrum unnormalized).

To summarize, the model of the auroral arc system we have devised is shown in Figure 2-7. It consists of a main arc, approximately 5 km wide (north-south), moving 0.61 km sec^{-1} to the north, imbedded in a drizzle region that extends about 850 km in the magnetic meridian plane. The absolute position of the main arc is determined from a knowledge of the rocket location when it entered the main arc. For the southern magnetic boundary of the arc at 108.7-km altitude, this corresponds to a displacement from Ester Dome of approximately 80 km. Although the drizzle is probably of the "inverted-V" type, we have assumed it to be constant over the entire region.

Electron Flux in Main Arc and Energy Deposition

Consider now the electron flux into the main arc. We have already seen (Figure 2-12) two measured particle spectra for this event. Visual inspection of the flight records at the Air Force Cambridge Research Laboratories (AFCRL) reveals that the spectra were nearly constant while the rocket remained in the arc. However, the ground-based 4278 Å and 5577 Å data show a slow decrease in intensity between +100 sec after rocket launch and termination of the flight at +413 sec (Reference 5), thus suggesting at least a weak time variation of the electron source. We shall ignore any such variations.

The simplest assumption concerning the pitch-angle distribution is that it is isotropic over the downward hemisphere. The limited data in this respect (Reference 6) indicate that, at least over the pitch-angle range from 35° to 55°, this assumption is valid. However, the magnitude of the spectral flux shown in Figure 2-12, based on this assumption, leads to discrepancies with the optical data. In fact, if the magnitude of the particle data is reduced by a factor of 2 to 3, better agreement with the upward-looking rocket-based 3914 Å and ground-based 4278 Å radiances appears to be achieved. Other possible alternatives are as follows. One is to

43

assume an arc width of only 2 km. This would then imply (Equation 2-2), however, an arc velocity of 0.71 km sec^{-1} that is clearly at variance with the data shown in Figure 2-13. Other possibilities are that the pitch-angle distribution is non isotropic or that the photometer data are in error. The recent work of Evans (Reference 19), in fact, shows that precipitating electrons usually exhibit a complex pitch-angle distribution ranging from one that is primarily field aligned to one that is isotropic.

In order to proceed with an ARCTIC code calculation, a definite decision on what to input for the particle flux had to be made. The weight of evidence at the time seemed to suggest that we should use the particle spectra shown in Figure 2-12, reduced by a factor of 2. This, indeed, is what we did. In so doing, greater weight was thus given to the 3914 Å rocket data shown in Figure 2-13. This was done because the ground-based data seemed to be in support of that from the rocket-based photometer.

The assumed arc flux, incident at an altitude of 200 km, is shown in Figure 2-14. It is one half of the 115 sec flux shown in Figure 2-12. No data at energies below 3 keV are available, so we have arbitrarily extrapolated the spectrum at 3 keV down to zero energy, although this procedure is hazardous. It should be pointed out, in fact, that most of the energy deposited above about 125 km is by electrons with energy < 3 keV. Consequently, in the absence of measured particle data for this energy region, results based on the assumed extrapolated spectrum are definitely suspect. Indeed, as we will see later, comparisons between our calculated results and the data suggest that the assumed spectrum (Figure 2-14) below 3 keV is probably an underestimate, while that shown in Figure 2-8 for the drizzle region, is probably an overestimate. Indirect evidence of an enhanced arc flux below 3 keV can be seen from the data curve in Figure 2-13 (also Figure 2-23) where a change of slope occurs at about 125 km.

All results shown below in this subsection, pertaining to the main arc, are based on the input spectrum shown in Figure 2-14 which, as

44
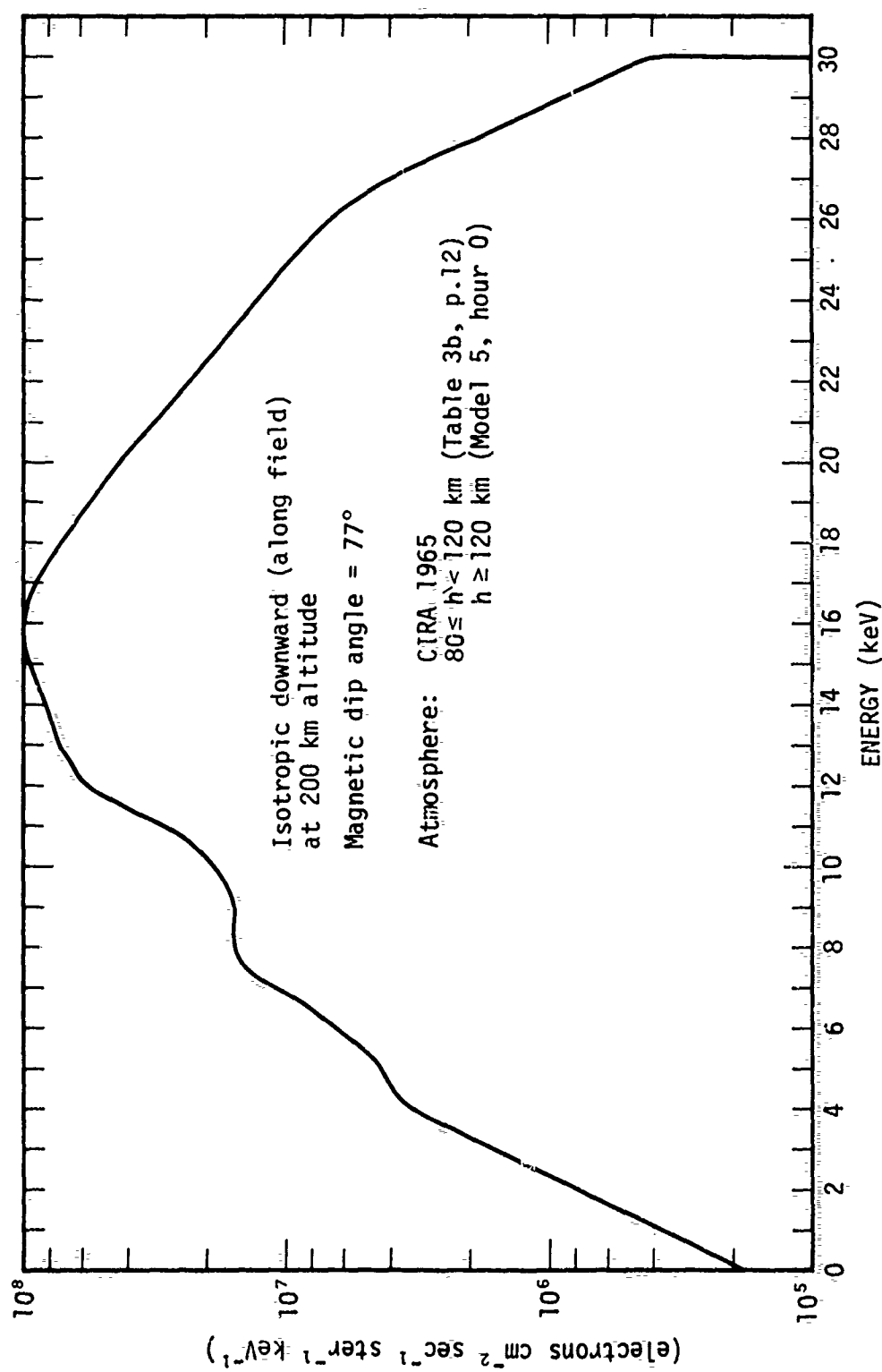
Figure 2-14. Incident electron flux assumed for auroral arc of March 27, 1973 (Black Brant 18.205-1).

45

we have mentioned, is a reduction by a factor of 2 from the reported values.
However, subsequent comparison of our results with data, together with recent
information on the possible importance of aerosol extinction in the lower
atmosphere, leads us now to suspect that the measured particle data may
have been correct and the 3914 photometer data in error. Although the
transmission losses due to aerosol extinction in Alaska at the time of
interest to us are not known, the estimates by Photometrics (Reference 5),
suggest transmission factors at Fort Yukon (due to Rayleigh scattering
and aerosol extinction) of 0.60 and 0.36 for zenith angles $0°$ and $60°$,
respectively. This would then place the ground-based optical data more in
line with the full particle flux data shown in Figure 2-12. As we will
see later, other data, especially those associated with the electron density
and the side-looking photometers, tend also to support the higher flux
values. Time constraints, however, have prevented us from using the larger
particle flux to redo the calculations reported below. The reader should
keep these remarks in mind, although they will be pointed out again at
appropriate places in the text below.

Figure 2-15 shows the energy deposition contours for the auroral
model assumed. The contours bear a superficial resemblance to the emission
(3914 Å and 5577 Å) profiles shown by Romick and Belon (Reference 20) for
other auroral arcs, but they are, in fact, quite different. Romick and
Belon subtract out the "background" in presenting their data while we
include it (the drizzle) in Figure 2-15. From our earlier discussion, it
is clear that the magnitude, character, and even spatial extent of the
"background" is closely related to the main arc, and a proper interpretation
of the auroral event demands that a consideration be given to the entire
system — main arc and drizzle. If we had used a more realistic spatial
distribution of flux in the drizzle region (rather than the constant mean
one) and then subtracted out a constant background, we would have obtained
contour profiles of the Romick and Belon type.

46
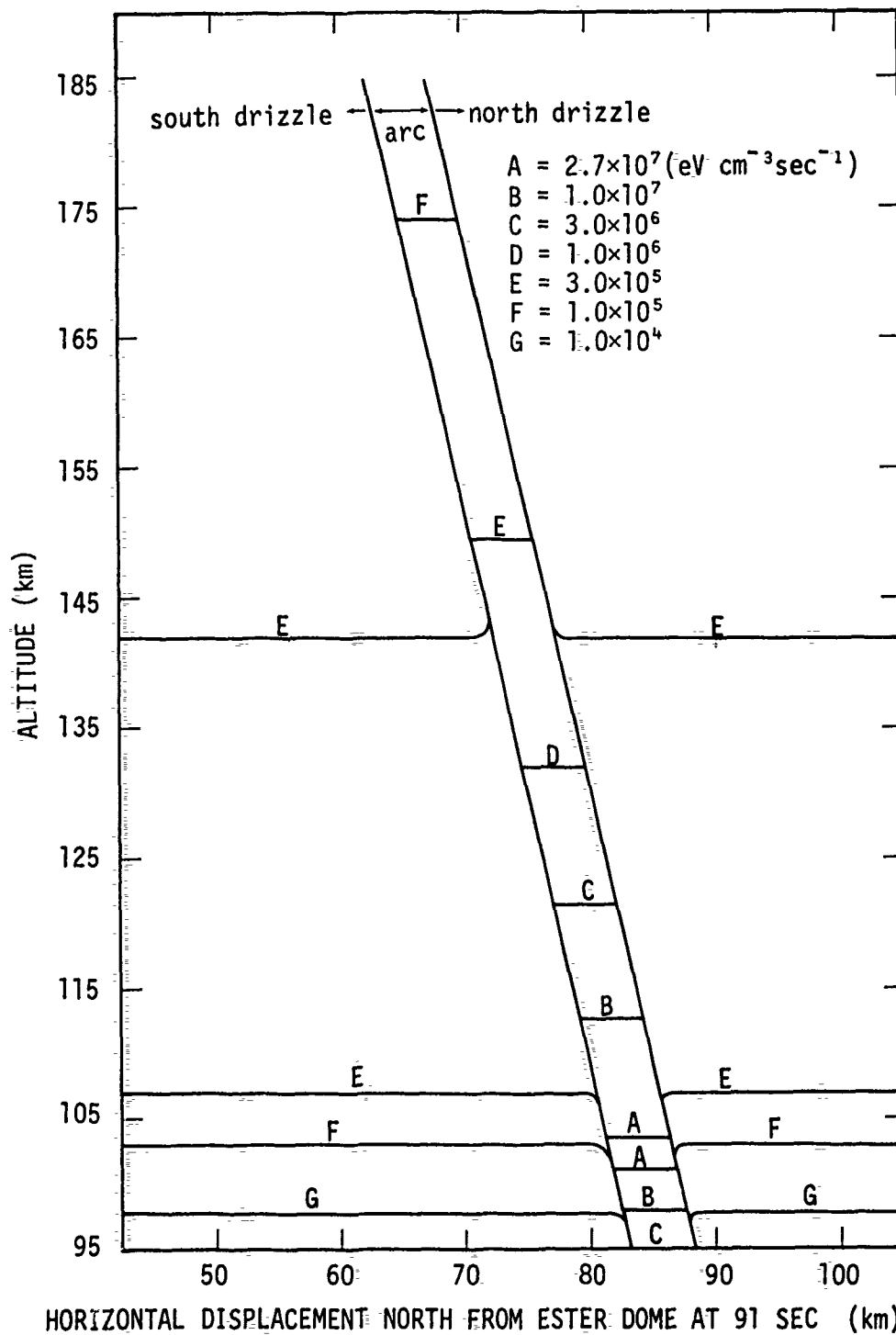
Figure 2-15. Calculated contours of constant energy deposition inside and outside the arc in magnetic meridian plane.

Figure 2-16 shows the calculated energy deposition rate profile inside the arc. Shown, for comparison, are the corresponding results obtained by Lockheed (LMSC). As mentioned earlier, the differences between the two results can be attributed almost exclusively to differences in the assumed elastic scattering cross section.

Figure 2-17 shows the calculated secondary electron production rate spectra at various altitudes in the arc, while Figure 2-18 shows the secondary electron flux spectra for the corresponding altitudes. The secondary flux at 150.5-km altitude is very similar to that at 122.5 km and is not shown in Figure 2-18. The dip that appears in the secondary flux at about 2.5 eV is due to vibrational excitation of N_2 that serves to deplete electrons with energy near that value.

Energy Partition in Arc

The ARCTIC code has been used to compute the volume excitation rate profiles for nearly 200 states of N_2, O_2, O, CO_2 and their ions. Figures 2-19 through 2-22 show selected results for a few of these states.

Calculational Procedure with Respect to
Chemistry and Delayed Emissions

With the exception of the foregoing production rate profiles for the main arc, the results presented in this subsection are formatted in a way to facilitate direct comparison with the rocket- and ground-based data. To do this, it is necessary to take into account the geometrical and dynamical nature of the arc as well as the rocket position and motion relative to the arc. This means that because of arc motion, different points along sight paths (through the arc) that are not field aligned will have been irradiated by the electron flux for different lengths of time. Thus, in computing the radiance along a given sight path through the arc, it is

48
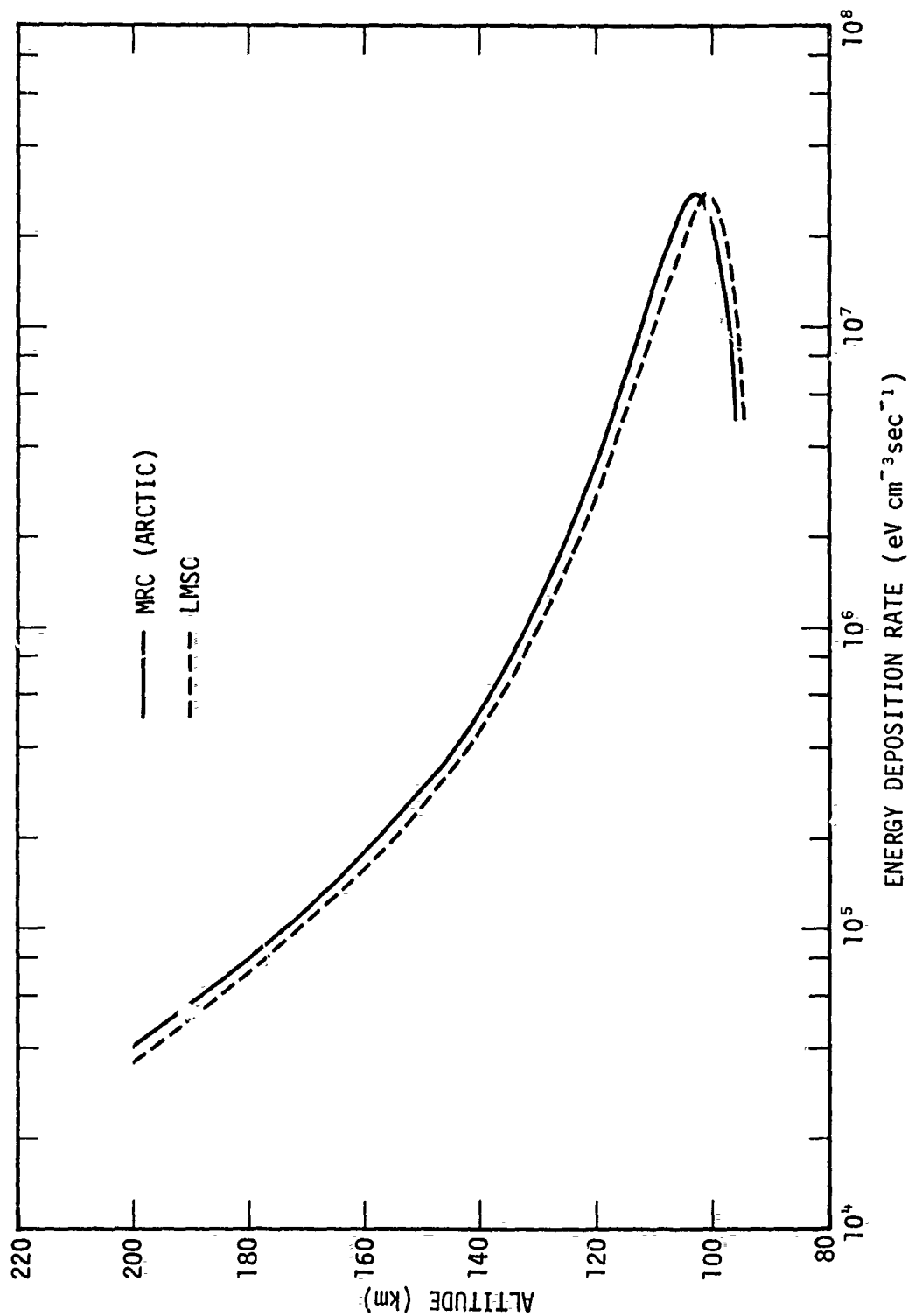
Figure 2-16. Calculated energy deposition rate for auroral arc of March 27, 1973 (Black Brant 18.205-1) using incident flux shown in Figure 2-14.
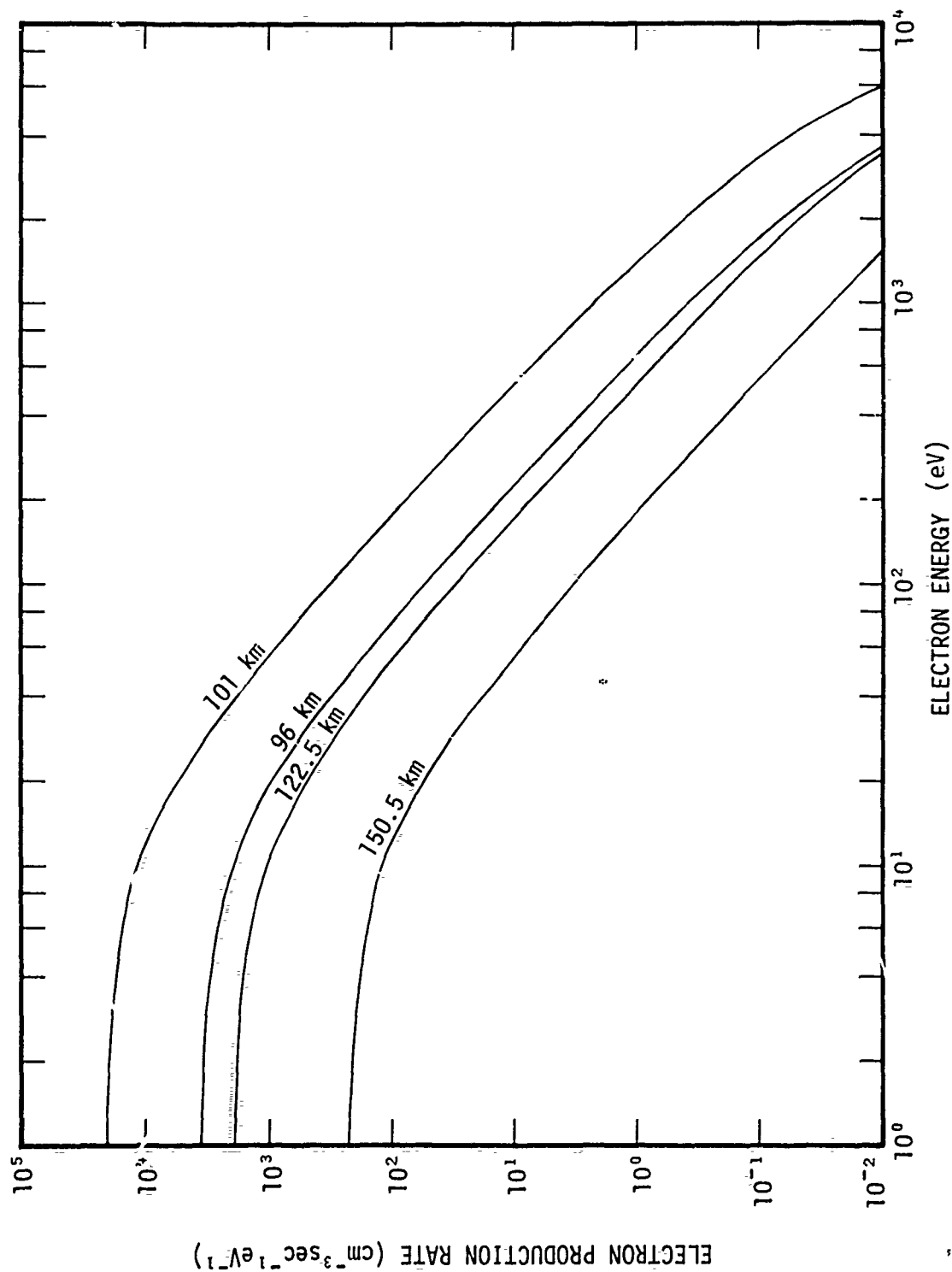
Figure 2-17. Secondary electron production rate spectra (Black Brant 18.205-1).
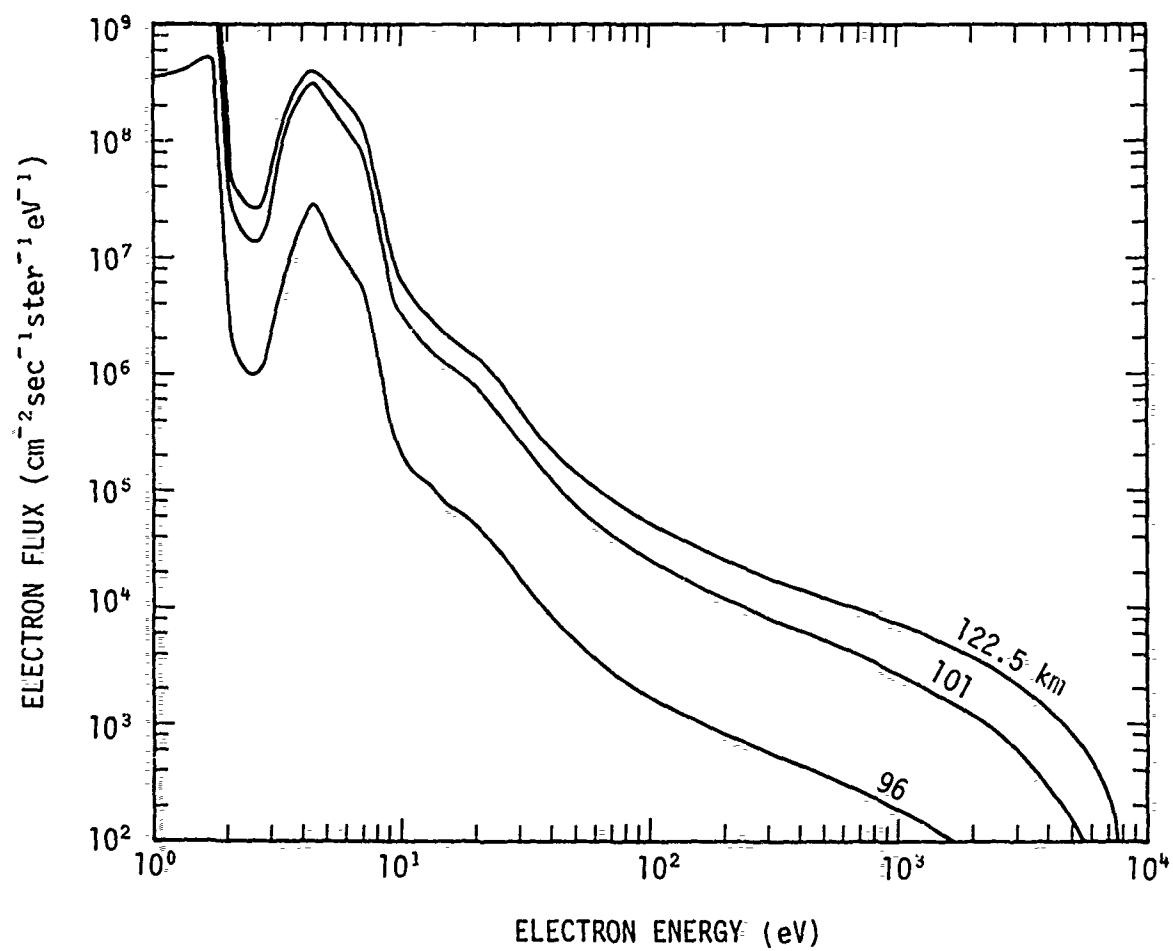
Figure 2-18. Calculated secondary electron flux spectra in auroral arc at
selected altitudes (Black Brant 18.205-1).
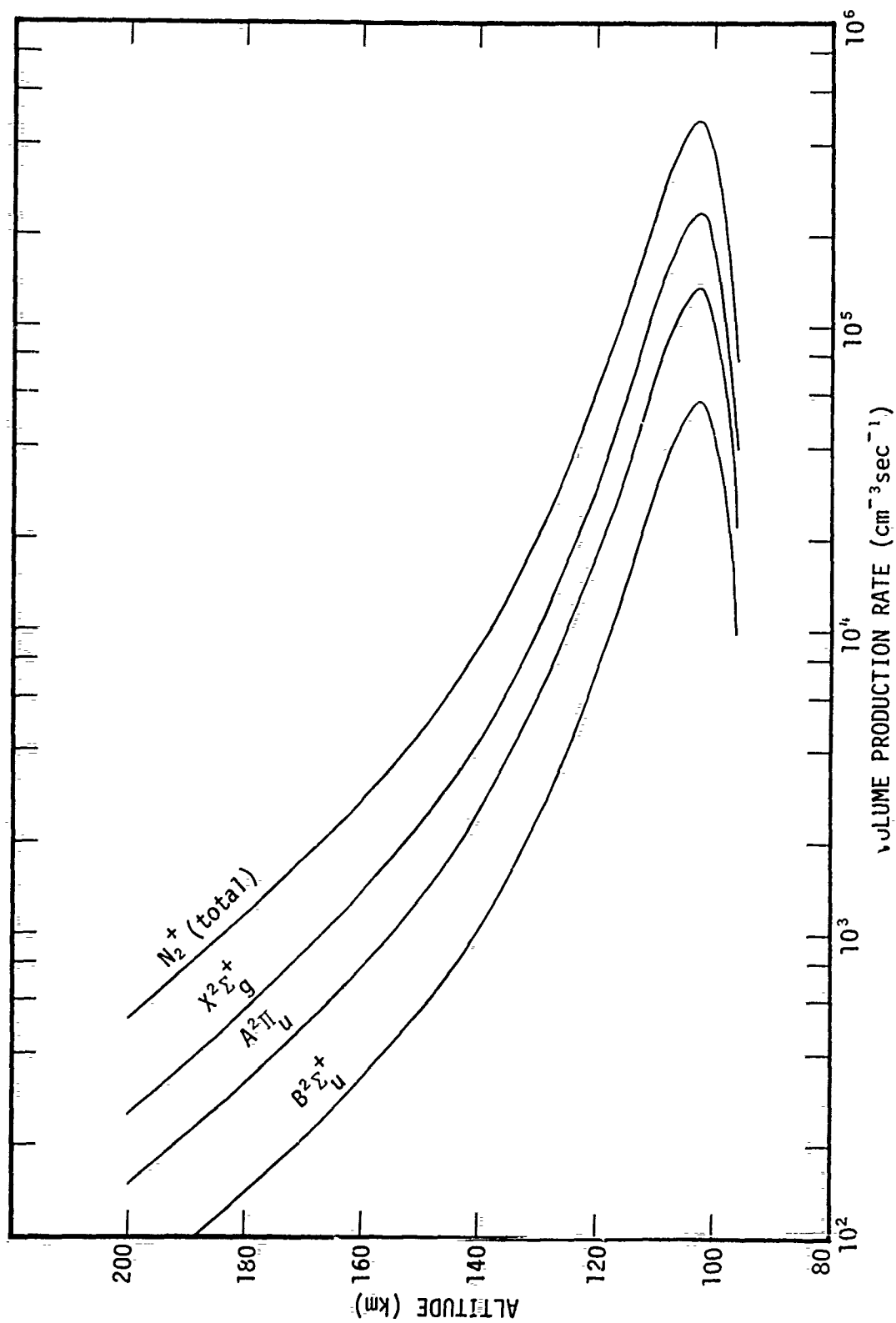
Figure 2-19. Volume production rates for selected states of N_2^+ (Black Brant 18.205-1).

ALTITUDE (km)

VOLUME PRODUCTION RATE ($cm^{-3}sec^{-1}$)

N_2^+ (total)

$X^2\Sigma_g^+$

$A^2\Pi_u$

$B^2\Sigma_u^+$

VOLUME PRODUCTION RATE (cm^{-3}sec^{-1})
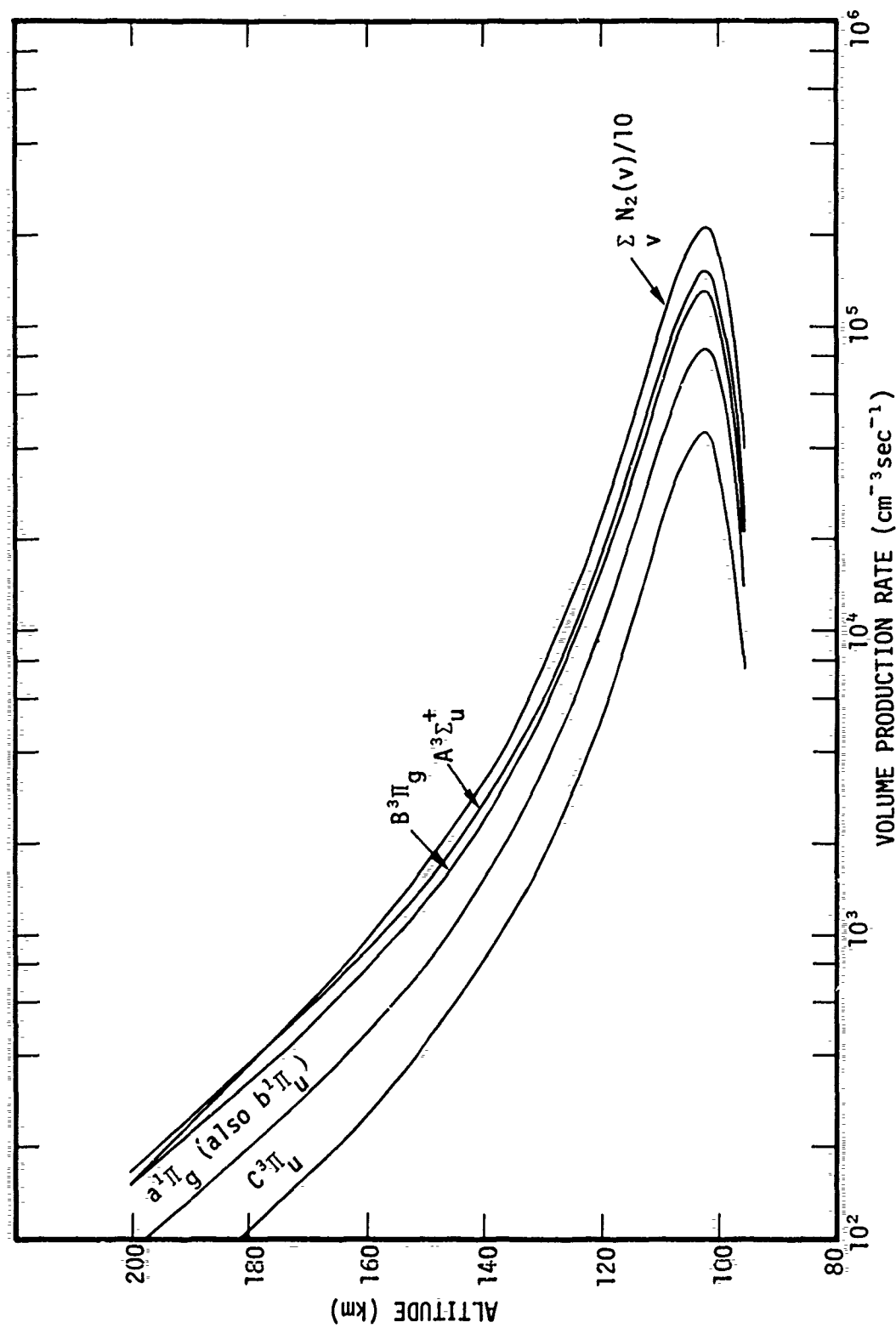
Figure 2-20. Volume production rates for selected states of N$_2$ (Black Brant 18.205-1).
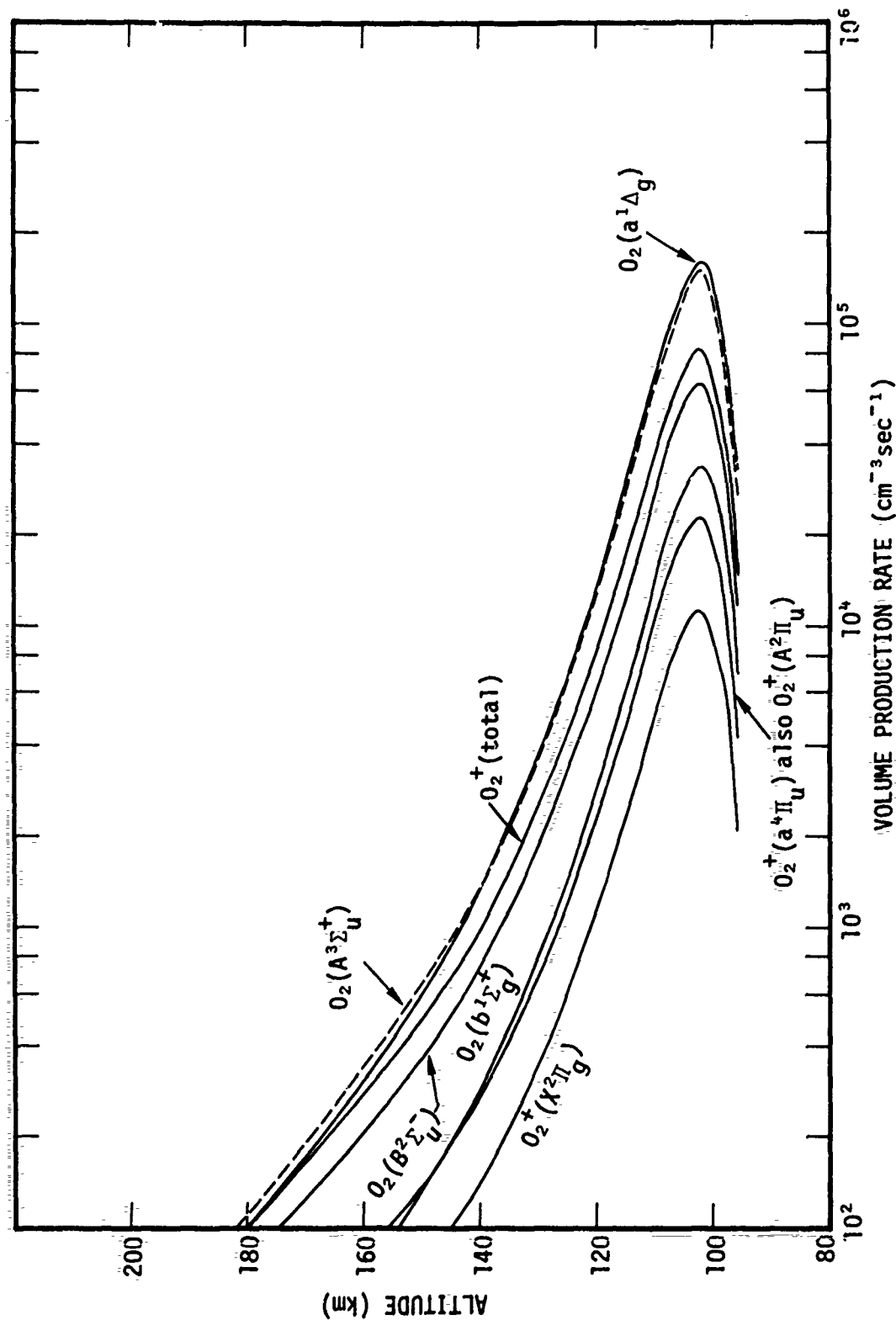
Figure 2-21. Volume production rates for selected states of O_2 and O_2^+ (Black Brant 18.205-1).
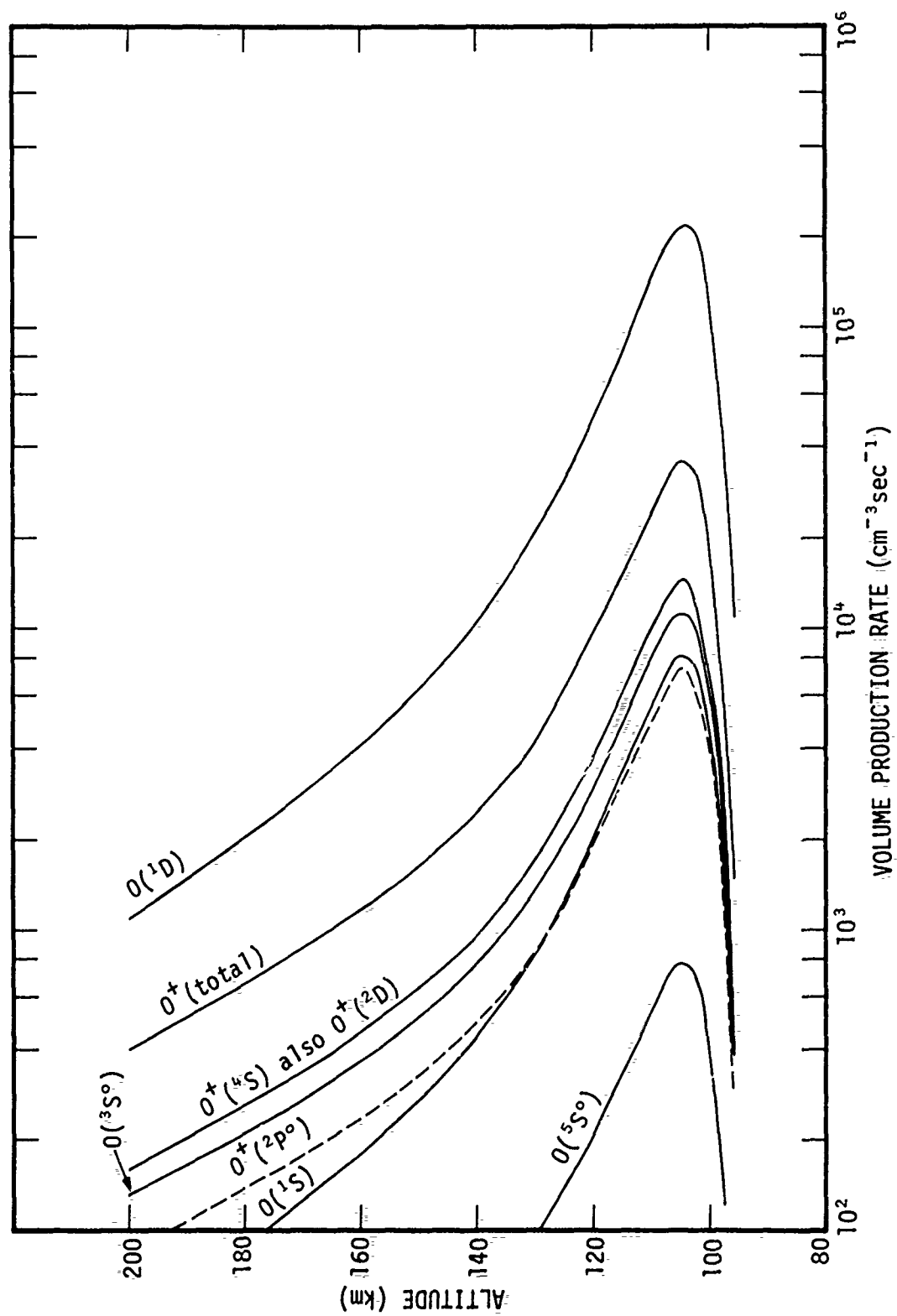
Figure 2-22. Volume production rates for selected states of O and O$^+$ (Black Brant 18.205-1).

necessary to allow for different chemistry times at each point along the
path (except for those prompt emissions, such as 3914 $\overset{o}{A}$ that do not depend
on chemistry). For example, in our model, when the main arc is moving with
constant velocity to the north, the environment at a point just in front of
the arc's leading edge is that provided by our 30 minute drizzle. On the
other hand, the environment at a point on the arc's trailing edge corresponds
to that produced by the arc flux (+ chemistry) operating for a time $\Delta W/V_{arc}$,
where ΔW is the horizontal arc width, and V_{arc} is the arc velocity. For
a different point, at a distance Δx behind the leading edge of the arc,
the chemistry operates for a time, t_{chem}, given by

$$t_{chem} = \Delta x/V_{arc} \quad . \tag{2-3}$$

In general, for an arbitrary point x,y behind the leading edge, where x
is the displacement north from Ester Dome and y is the altitude, Δx
is given by

$$\Delta x = x - [85 + (\Delta t - 91)\ V_{arc} - (y - 108.7)/\tan \delta]\ . \tag{2-4}$$

Here, δ is the magnetic dip angle and Δt is the time elapsed since
rocket launch.

In performing the chemistry calculations for each point along a
given sight path, care must be exercised to see that the arc flux is turned
on while the point is within the arc and is then turned off and the drizzle
flux turned on when the arc has passed.

The results presented below were deduced from ARCTIC code runs
that may be summarized as follows. The drizzle environment was determined
by inputting the drizzle flux (Figure 2-8) at an altitude of 200 km. The
energy deposition and partition were then computed and the chemistry sub-
routine run for times to 30 minutes. The main arc flux (Figure 2-14) was
then turned on in the above-determined drizzle environment, and deposition

56

and partition profiles were calculated. The chemistry subroutine was run
for 8.2 sec with the main flux on and, subsequently, to 60 sec with only
the drizzle flux operating. The calculations, for chemistry times between
8.2 and 60 sec, provide estimates of the decay in the emission rates and
changes in species concentrations that ensue after the main arc has passed
beyond the point in question.

Results and Comparisons with Data

Output from the ARCTIC code, for both the main arc and the drizzle
region, is voluminous. It includes many items, such as species concentra-
tions and volume emission rates, that will not be shown here because of
space limitations. Instead, with one exception[*], we limit the results shown
to those that can be compared directly with data available to us.

Except as noted below, the formulas used to compute the various
emissions are given in Reference 1 (Appendix C) and will not be repeated here.[**]

Figure 2-23 shows the calculated and observed zenith radiance at
3914 $\overset{o}{A}$ as a function of rocket altitude on ascent. As was mentioned earlier,
the abrupt change in slope of the data at 125 km may be indicative of the
presence of a much larger flux of electrons with energy < 3 keV than what
our input spectrum (Figure 2-14) shows. As was also discussed earlier,
the slope change below 110 km is an effect related to the geometry of the
arc and to its motion relative to the rocket.

---

[*] The calculated electron temperature profile is shown in Figure 2-37,
    although no information on measured values are yet available
    (Reference 6).

[**] The reaction numbering in the first column of Table C-1 (Reference 1) is
    in error. From the top down it should read: 68, 74, 75, 71.
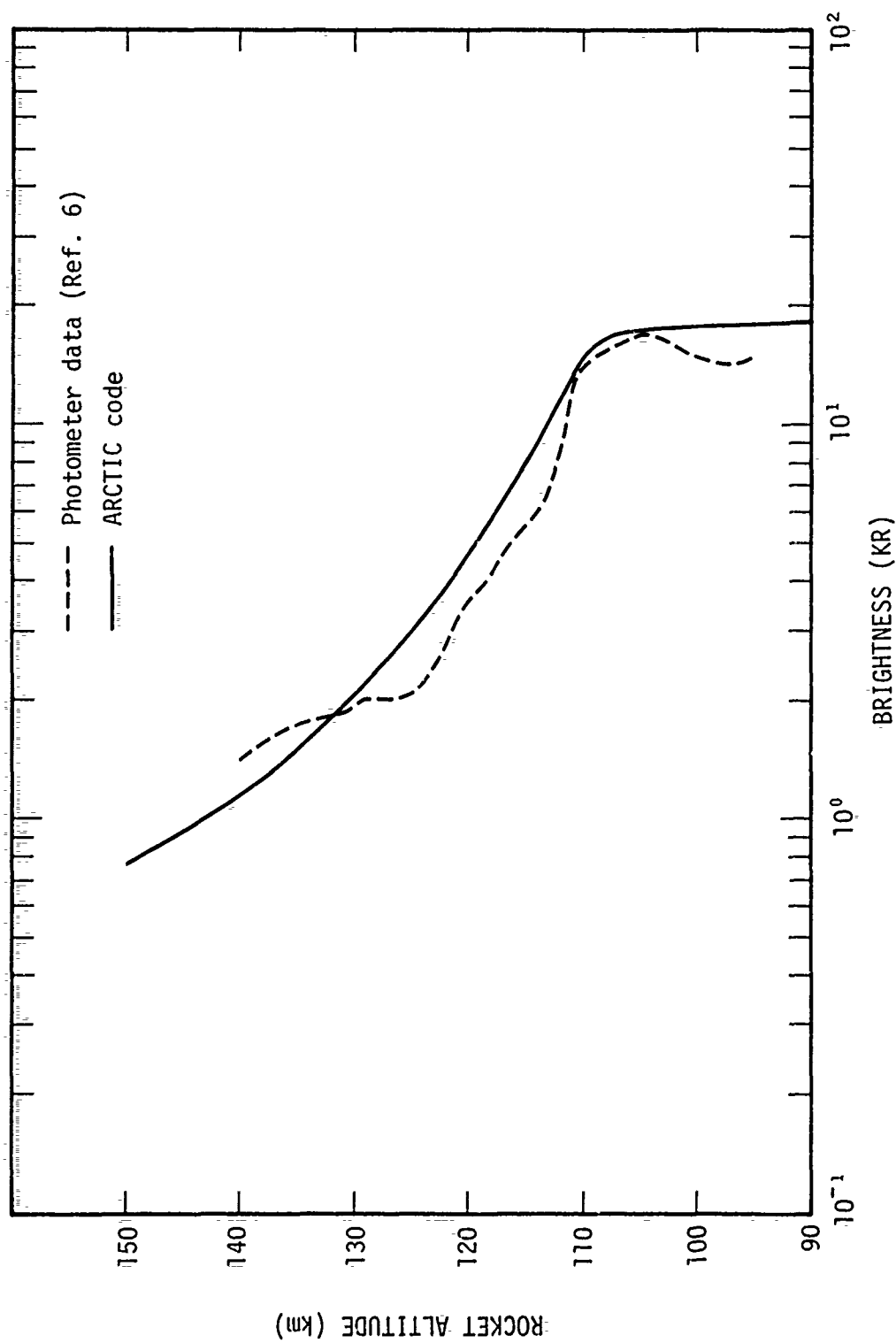
Figure 2-23. 3914 Å brightness viewed vertically upward from Black Brant 18.205-1 on ascent.

Considerable weight was given to the data shown in Figure 2-23 in deciding on the magnitude of the input particle flux. Use of the reported flux spectrum shown in Figure 2-12, rather than the one shown in Figure 2-14, would have led to calculated values for the 3914 Å brightness twice as large as the calculated ones shown in Figure 2-23 — and more than twice as large as the indicated data below 130 km.

Figure 2-24 shows comparisons between the calculated and observed brightness at 4278 Å from ground-based scanning photometers at Ester Dome and Fort Yukon. The instruments scanned in the magnetic meridian plane, and the results, corresponding to times between 92 and 102 sec after rocket launch, are given as functions of the zenith angle.

The data clearly show the presence of a drizzle to the north and south of the main arc. The Fort Yukon data give a rough idea of the northern extent of the drizzle region. The small peak in the Fort Yukon data to the north is probably a geometrical effect due to the long path lengths at large zenith angles.

The calculated full width at half maximum (FWHM) of the arc brightness is narrower than that measured. We have performed parametric studies of the FWHM seen from Fort Yukon and Ester Dome for different arc widths, ΔW, and velocities, V_{arc}. The results show an insensitivity to variations in these parameters. We suspect that the main source of broadening is due to the presence of an "inverted V" structure for the drizzle region rather than the constant one assumed here.

We should point out that the calculated values shown in Figure 2-24 have not been corrected for transmission losses to the ground if these losses are as great as quoted earlier (p.44), the magnitude of our calculated radiances would be smaller than those observed. In fact, if we were to allow for the variation of the transmission factor with zenith
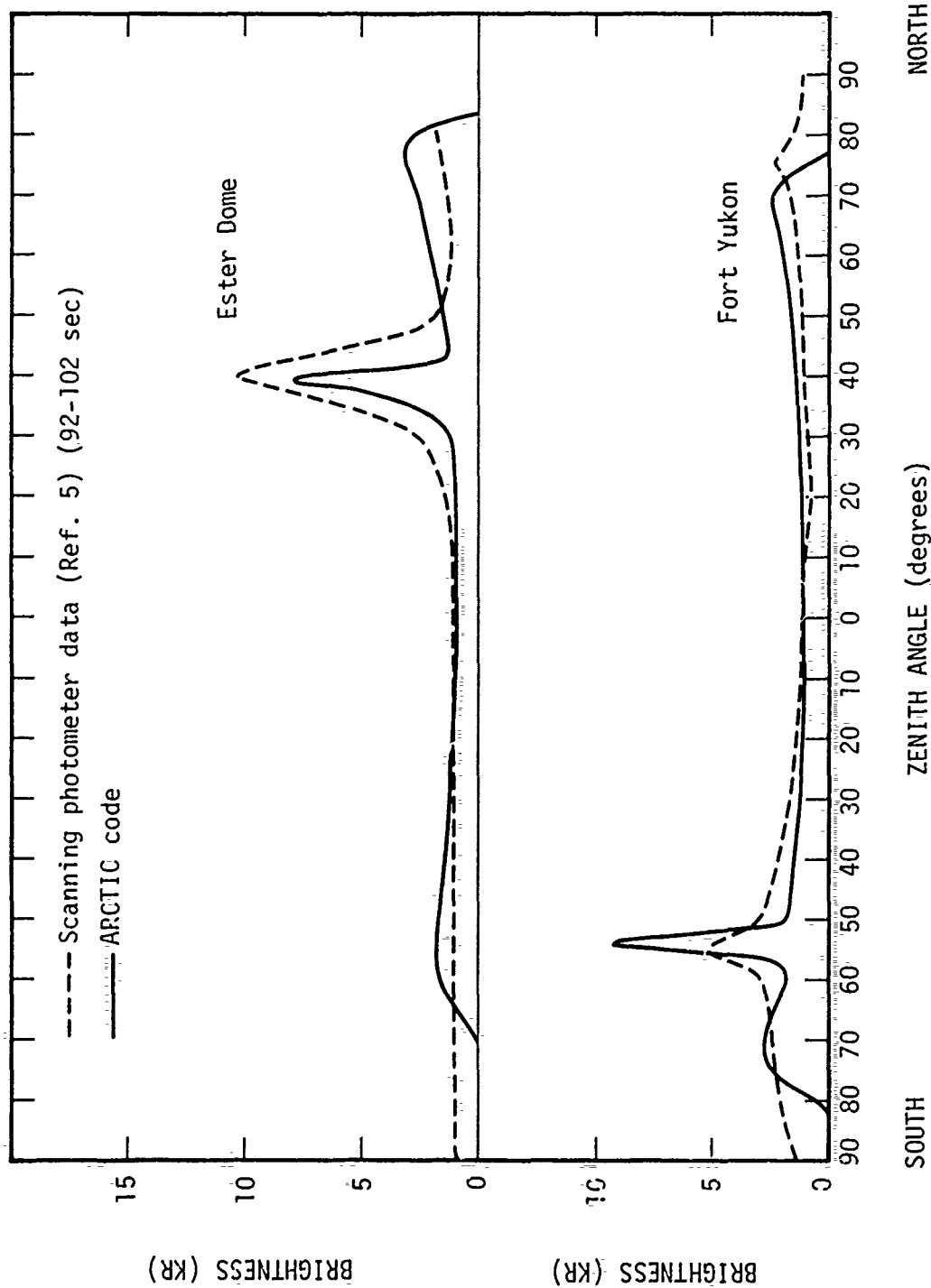
Figure 2-24. 4278 Å brightness at Ester Dome and Fort Yukon, Alaska (auroral event of 27 March 1973).

60

angle, and were to then increase the resulting values by a factor of 2, the magnitude of our results at both Ester Dome and Fort Yukon would appear to be in closer agreement with the data than Figure 2-24 indicates. This would then lend support to the idea that the magnitude of the reported particle flux (Figure 2-12) may be correct and the rocket-borne 3914 $\overset{\circ}{A}$ data (Figure 2-23) erroneous.

Figure 2-25 shows similar comparisons with the ground-based scanning photometers operating at 5577 $\overset{\circ}{A}$ for times between 89 and 99 sec. The calculated volume emission rates are based on the equation

$$\dot{\Phi} \ (5577 \ \overset{\circ}{A}) = 1.34 \ [O(^1S)] \qquad (cm^{-3} \ sec^{-1}) \qquad (2-5)$$

that presupposes a 0.75-sec lifetime for the ^1S state of atomic oxygen. The $O(^1S)$ concentration is determined from the chemistry subroutine, with the assumed production mechanisms shown in Table 3-2 of the next section. The entire chemistry scheme is shown in Reference 1 (Table B-1).[*] In the next section we emphasize that the rate coefficients for (what now appear to be) the dominant production sources of $O(^1S)$ are not at all well known. In our scheme, the quenching of $N_2(A^3\Sigma)$ by $O(^3P)$ is dominant, but other reactions, with uncertain rate coefficients, combine to compete with it. Direct excitation by the bombarding electrons appears to contribute in only a minor way.

The foregoing remarks should serve to indicate that any agreement between calculated and observed radiances at 5577 $\overset{\circ}{A}$ is probably fortuitous.

Figure 2-25 shows that the calculated values are generally high, although the FWIM is approximately correct. The latter agreement may imply that most of the emission is from the main arc. The angular positions

---

[*] The only reaction rate coefficient in Table 3-2 that differs from that in Table B-1 (Reference 1) is for quenching of $N_2(A^3\Sigma)$.
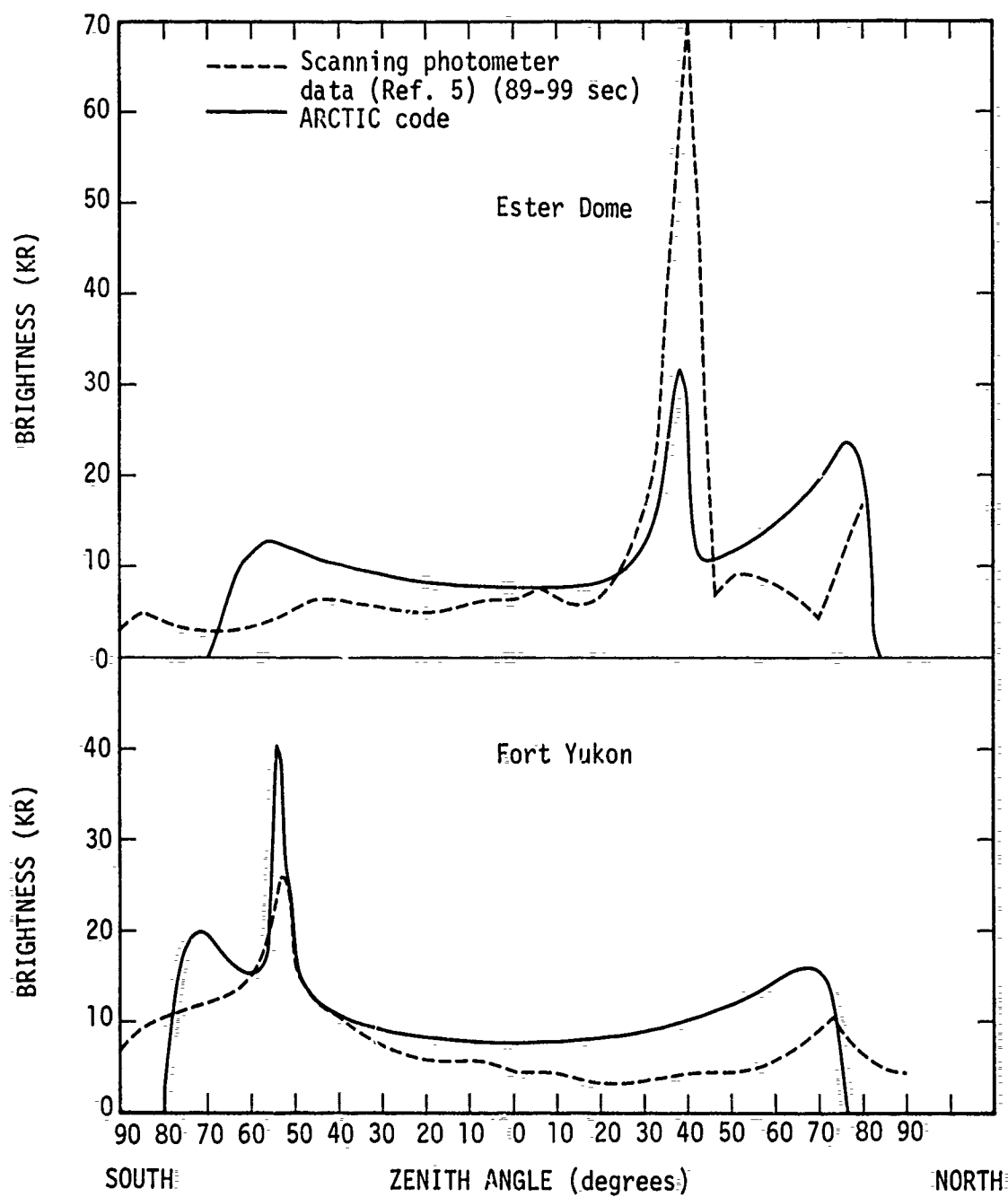
Figure 2-25.   5577 Å brightness at Ester Dome and Fort Yukon, Alaska (auroral event of 27 March 1973).

of the peaks, however, are somewhat different from the measured ones (also at 4278 Å). This may be attributable to a somewhat harder spectrum for the main arc flux. The peak in the data to the north of Fort Yukon is, again, probably a geometrical effect.

Figure 2-26 shows the peak zenith spectral radiance near 5.4 μm observed with the nose-mounted circular variable filter (CVF) spectrometer on board the rocket (Reference 21) together with our computed values. There is considerable scatter in the actual data points, but they lie roughly within the cross-hatched area shown. We do not know what additional spread may exist due to experimental uncertainty associated with the data points themselves. The comparison is shown for both the ascent and descent portions of the flight.

The computed emission is completely dominated by the $N(^2D) + O_2$ chemiluminescent reaction for which photon efficiencies have not been measured. However, we have assumed that the vibrational states of NO are equally populated up to $v = 18$ following each reaction, and the photon efficiencies that result from this assumption are shown in Table C-1 (Reference 1).* On the same basis, we have computed the spectrum of the fundamental- and first overtone-band emissions. The results of this calculation are given in Appendix A.

The ARCTIC code outputs volume emission rates for the entire band being considered — in this case, the NO fundamental at 5.4 μm. In order to compare with the spectrometer data, we used the information supplied to us (References 4, 21) for this instrument, together with the computed spectrum shown in Figure A-1. The wavelength region scanned by the instrument was from 1.6 μm to a maximum of about 5.4 μm. At 5.4 μm the bandwidth of the spectrometer is about 0.18 μm. Thus, from Figure A-1, the peak emission observed with this instrument should occur in the wavelength interval from 5.22 to 5.40 μm. The calculated spectrum (Figure A-1) shows that 16 percent of the total band energy is emitted in this interval.

---

* For correction to this table, see footnote on p. 55 of this report.
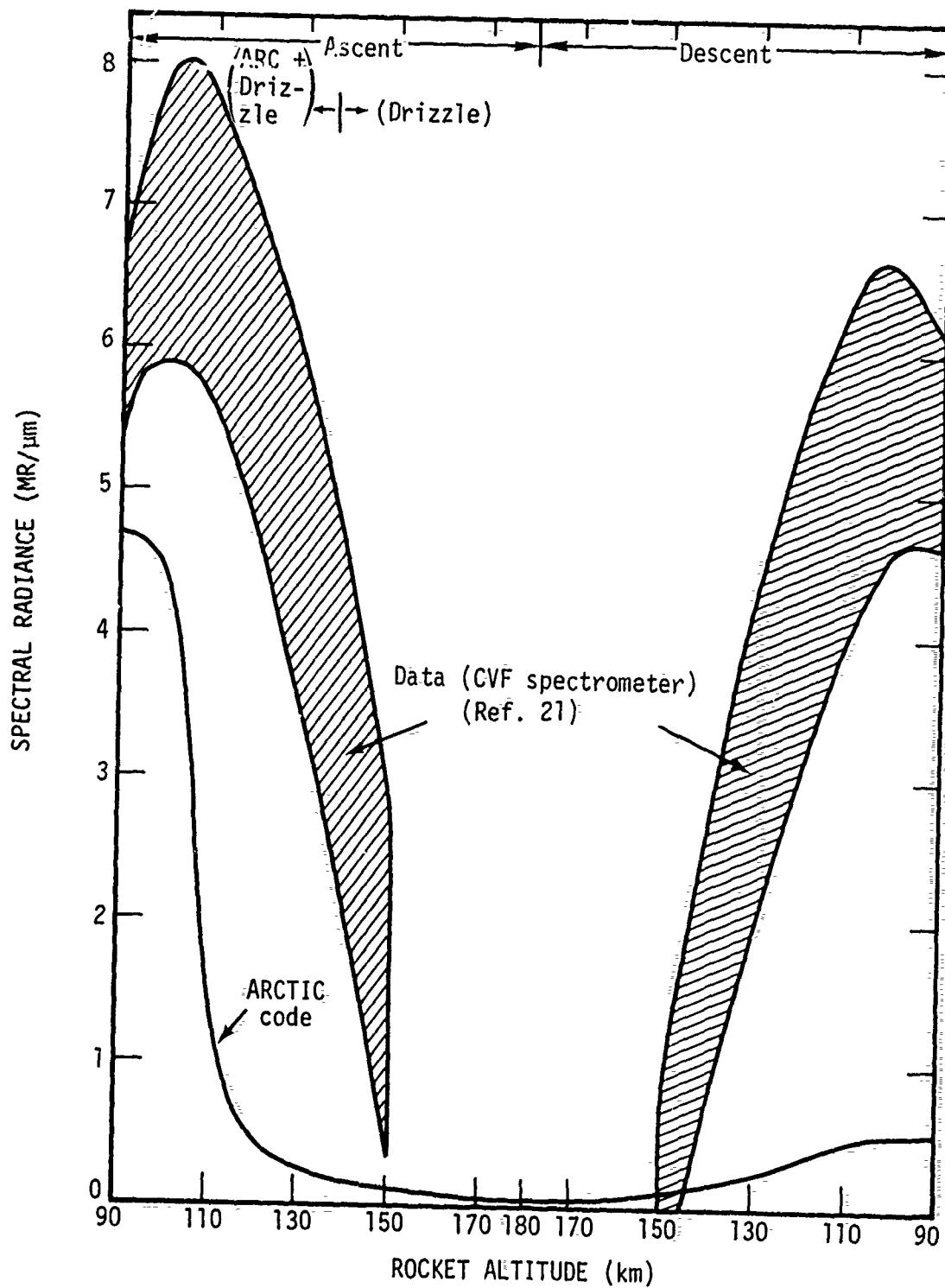
Figure 2-26.   Peak zenith radiance near 5.4 μm (Black Brant 18.205-1).

64

Therefore, to compare our calculated emission rates with the spectrometer data, we have multiplied them by a factor $0.16/0.18 \simeq 0.9$.

Unless recalibration subsequently changes the observed values downward, agreement with calculations is quite poor, especially for the descent portion of the flight where at 90 km we appear to be about an order of magnitude low. It is interesting that the measured radiance on descent (outside the arc) is not much lower than that on ascent, even though a more pronounced arc enhancement would be expected on ascent. Use of the reported particle flux (Figure 2-12) rather than one half of it (Figure 2-14) would have improved the agreement, but not by a sufficient amount. The assumed photon efficiency for the $N(^2D) + O_2$ reaction could be raised, but not by more than a factor of 2 (to preserve energy conservation). It is more likely, indeed, that the value used here is already on the high side. The assumed emission spectrum (Figure A-1) may also put too much energy at wavelengths beyond detectability of the instrument. However, the slopes of the observed and computed curves are different. The effect is as though an additional strong production source of vibrationally excited NO (or of $N(^2D)$) is operating between about 100 and 110 km both inside and outside the arc. Assuming the correctness of the data, we are presently unable to account for the large differences.

Figure 2-27 is another comparison at 5.4 μm, this time with data from the rocket-borne dual channel radiometer in the rocket nose. To make the comparison with the data, we multiplied our code values (for the entire NO fundamental band) by a factor $f = 0.23$. This factor was obtained by multiplying our normalized spectrum, $I(\lambda)$, (Figure A-1) by the instrument relative response function, $R(\lambda)$, (Reference 4) and integrating. Thus,

$$f = \int_0^\infty I(\lambda)\, R(\lambda)\, d\lambda \quad . \tag{2-6}$$

65
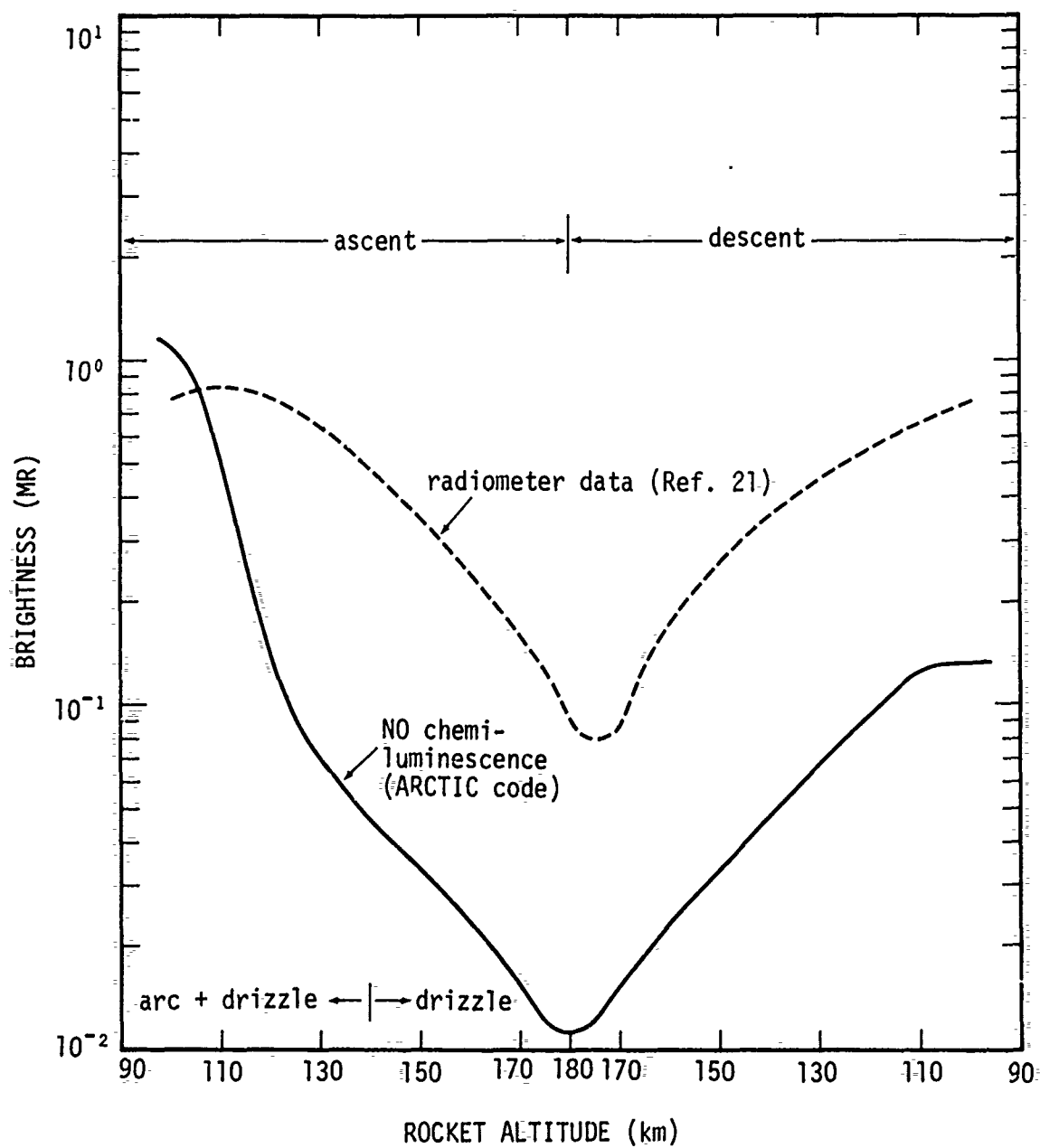
Figure 2-27. Calculated and observed intensity in 5.4-μm band (vertical path) (Black Brant 18.205-1).

Except at altitudes below 110 km on rocket ascent, our computed values are again considerably lower than those observed. Note that these data, like those from the spectrometer, show descent radiances nearly as high as those measured on ascent, contrary to our calculations and expectations.

Figure 2-28 compares the calculated values for the peak zenith radiance near 4.3 µm with those measured by the CVF spectrometer. The theoretical values include contributions from NO^+ chemiluminescence, CO_2 vibraluminescence, and ambient (earthshine excited) CO_2 emission. The NO^+ and CO_2 (vibraluminescence) curves in Figure 2-28 were computed with the ARCTIC code; the ambient CO_2 curve was deduced from the work of Kumer and James (Reference 23).

Details concerning the NO^+ chemiluminescence model in ARCTIC can be found in Reference 1 and in Appendix B of this report. Calculations based on this model show that most of the NO^+ chemiluminescence arises from the reactions

$$O_2^+ + NO \rightarrow O_2 + NO^+$$

$$N_2^+ + O \rightarrow N + NO^+$$
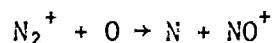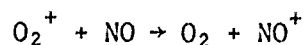
that are sufficiently exothermic to populate the tenth vibrational state of NO^+. With the assumption that each state up to $v = 10$ is populated with equal probability, we have computed a spectrum for the emitted photons. The results are shown in Appendix B (Figure B-1).

The spectral resolution of the spectrometer at 4.3 µm is about 0.16 µm (Reference 4). As the spectrometer sweeps in wavelength over the spectrum shown in Figure B-1, the maximum power it will detect will occur in a 0.16-µm interval from 4.28 to 4.44 µm, representing about 40 percent of the total band emission. In order to compare our calculations with the

67
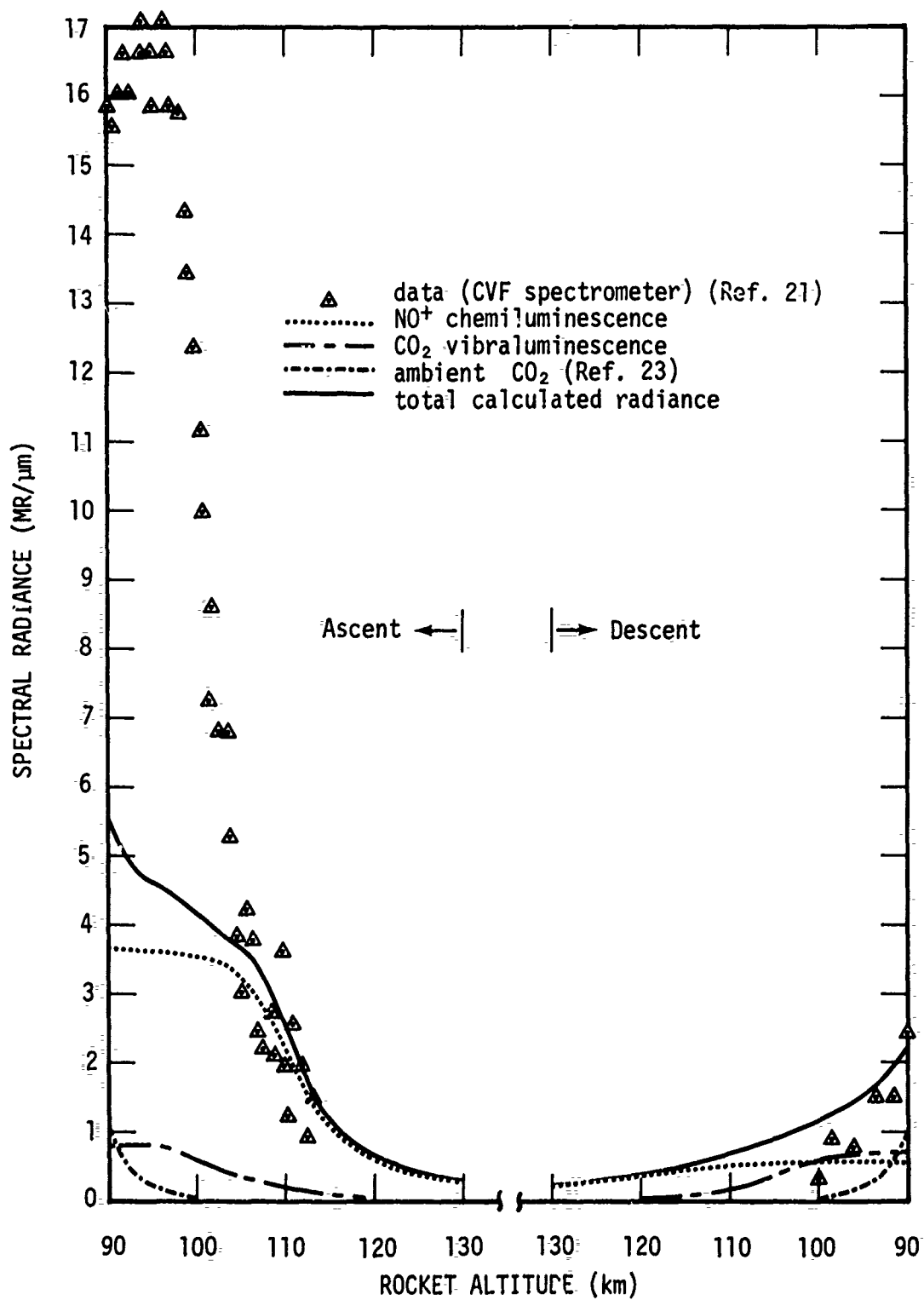
Figure 2-28. Peak zenith radiance near 4.3 µm (Black Brant 18.205-1).

spectrometer observations, therefore, we have multiplied them by 0.40/0.16 = 2.5, which then places our radiances on a "per micrometer" basis.

As for the CO_2 vibraluminescence (4.3-μm band), we have assumed a spectral profile similar to that for thermal emission at 300 °K. Our low resolution (0.02 μm) approximation to the computed spectrum of Malkmus (Reference 24) is shown in Figure 2-29. As the spectrometer sweeps across this spectrum, with a 0.16-μm resolution, virtually all of the band power will be detected. Therefore, to compare our CO_2 vibraluminescence values with the spectrometer data, we have multiplied them by 1/0.16 = 6.2.

The solid curve in Figure 2-28 is a sum of the three contributions described above. No corrections for radiation transport, self absorption, resonance scattering, etc., have been made, although we don't believe these could serve to enhance the calculated values.

From Figure 2-28 we see that the total calculated radiance on ascent is larger than that for the descent portion of the rocket flight, but not nearly as much as the data show. Although the comparisons between 105 and 112 km (where the data end) on ascent are quite favorable, the computed values below 100 km are low by as much as a factor of 4. Considering the many uncertainties inherent in the calculation, this may not be bad, but the rapid fall off in the ascent data above about 98 km is more than we can account for. The descent data (only available below 110 km), however, are in reasonably good agreement with the calculations.

Figure 2-30 is a comparison between our calculated zenith brightness at 4.3 μm and data (Reference 21) from the rocket-borne radiometer on both ascent and descent. There is considerable spread in the data that lie approximately within the cross-hatched areas. The theoretical values again include contributions from the three sources described above and indicated in Figure 2-30.
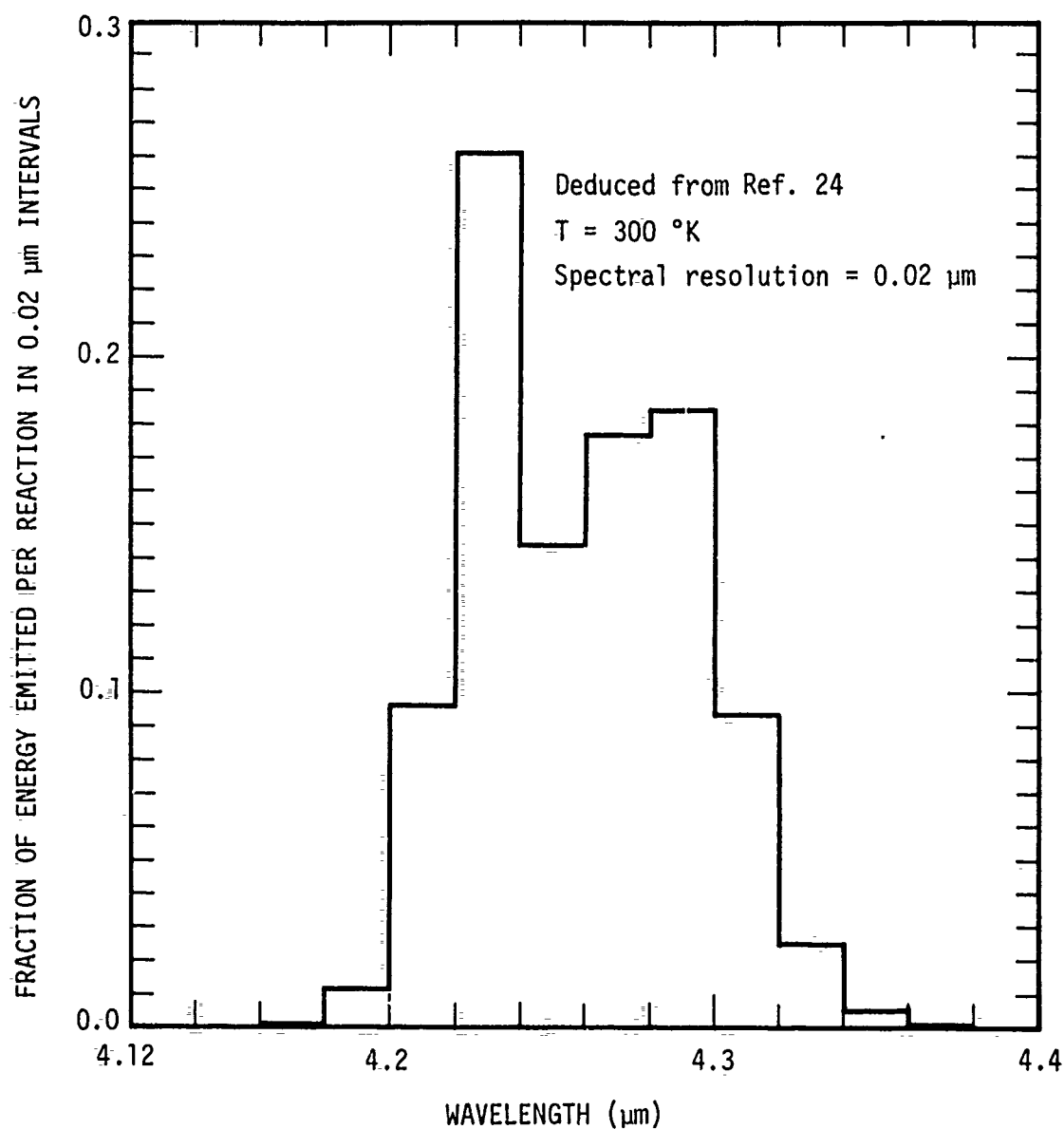
Figure 2-29. Estimated spectral distribution of CO_2 vibraluminescence from the reaction $N_2(1) + CO_2(000) \rightarrow N_2(0) + CO_2(001)$.
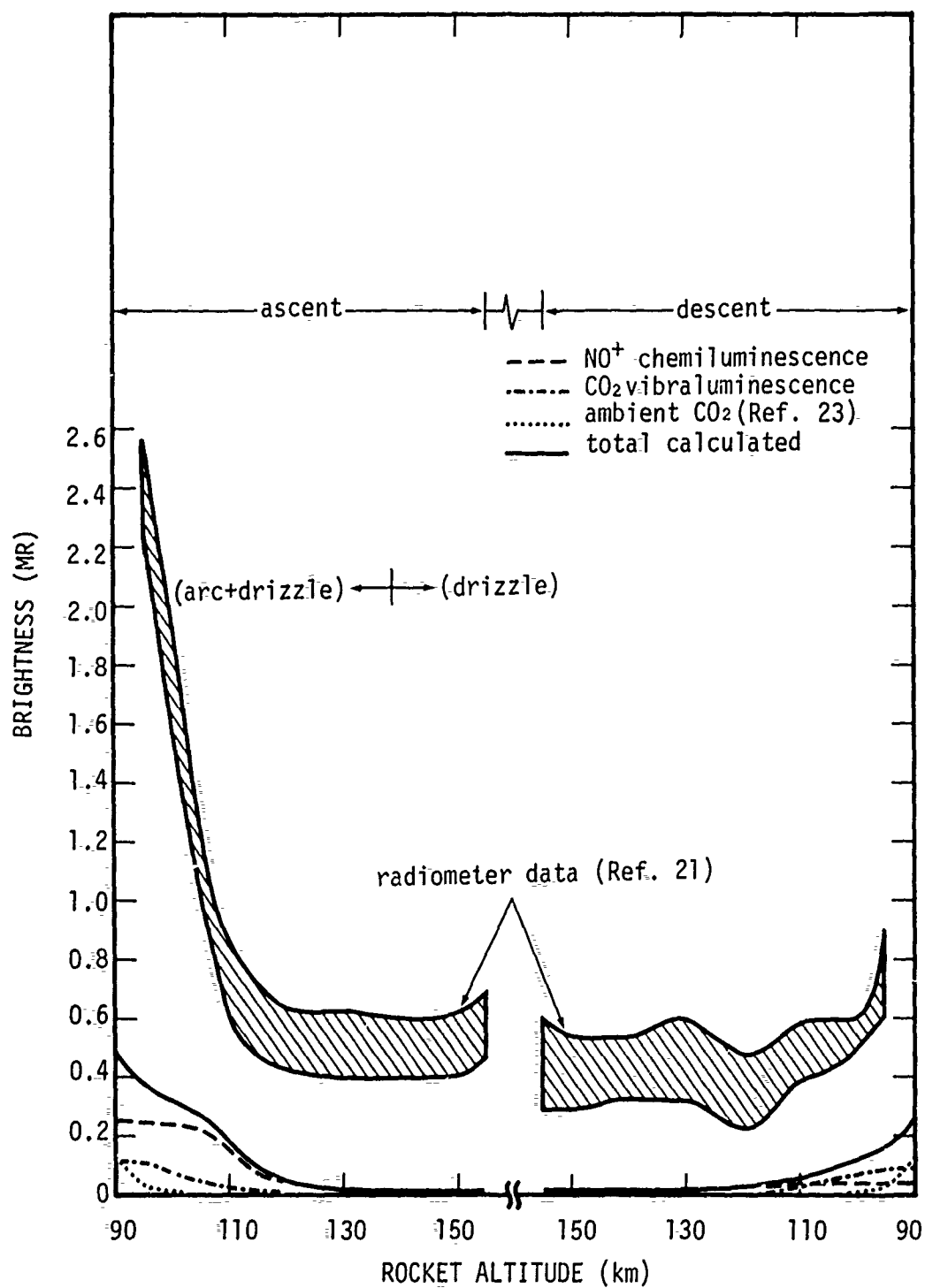
Figure 2-30. Calculated and observed intensity in 4.3-μm band (vertical path) (Black Brant 18.205-1).

71

To compare the code values (for the entire bands) with the radiometer data, we have folded the instrument relative response function (Reference 4) with the respective emission spectra (Figures B-1 and 2-29) according to Equation 2-6. The resulting correction factors applied to the calculated NO^+ chemiluminescent and CO_2 emissions are 0.16 and 0.79, respectively. With these corrections, the total calculated values are seen to be lower than the reported ascent data by factors ranging from about 6 at 100 km to 4 at 110 km to 20 or so at 130 km. The comparison on descent is only slightly better. It is interesting to note that our (full) band radiances, without applying the above-mentioned correction factors, would have put us in much better agreement with the data.

A peculiar feature of the radiometer data shown in Figure 2-30 is its apparent constancy above about 120 km rather than a monotonic decline as would be expected. The spectrometer data (Figure 2-28) are inadequate to confirm this because they do not extend to altitudes above about 112 km.

An increase by a factor of 2 in the assumed particle flux into the arc would certainly improve our agreement with the ascent portion of this flight, although it would be insufficient by itself to account in full for the differences.

We turn now to comparisons with the side-looking instruments on board the rocket. These consisted of five visible photometers and a dual-channel radiometer operating in the 5.4- and 2.7-µm bands. Each instrument was mounted with its viewing axis 10° above the normal to the rocket axis. If the rocket attitude were vertical at all times, the viewing sight paths would be 10° above the horizontal. However, as mentioned earlier, the rocket axis was inclined about 3° south (magnetic) from the vertical. As the rocket spun, therefore, the sight paths to the south and to the north were elevated about 7° and 13°, respectively, from the horizontal.

72

The data supplied to us (Reference 6) included uncalibrated strip charts of voltage output as a function of time for each of the instruments, and calibrated versions of these charts (except for the 5.4-μm channel) for four specific rocket spins corresponding to altitudes between 95 and 103 km on ascent. Because of rocket spin, the data are continuous plots of the radiance as functions of azimuth and elevation angle. From the four calibrated spins available to us, we have attempted to pick out radiance values corresponding to sight paths toward magnetic north (through the arc) and toward magnetic south (away from the arc) and have performed our calculations for these same sight paths.

Before comparing the data and calculations, we emphasize again that the sight paths in question include long segments through the drizzle region and (except for the east-west directions not considered here) relatively short segments through the main arc. In fact, the radiances measured to the south exclude the arc emissions entirely, at least until the rocket entered the main arc at about 108-km altitude. Since details of the drizzle region are largely unknown, we can not , a priori, expect our assumed model to provide agreement in every detail with the observations. Rather, the hope is that the model can account, at least qualitatively, for the observed features.

Figure 2-31 shows our computed brightness at 2.7 μm for the northward- and southward-viewing paths. Only one north-viewing data point and two south-viewing ones are shown because so many spikes appear in the records it is hard to pick out representative values. In addition, it should be mentioned that the side-looking radiometers (2.7 and 5.4 μm) detected large signals that are believed to be thermal emission from ejected pieces of the rocket (such as "clamshells" and other instrument covers). For this reason we do not presently have data from these radiometers that we can, unequivocally, attribute to the atmosphere. However, the data points shown in Figure 2-31 are believed to be aurorally produced.

73

Figure 2-31. 2.7-μm brightness (≈horizontal) viewed toward magnetic north and south from Black Brant 18.205-1 on ascent.

74

The computed emission arises almost exclusively from the $N(^2D) + O_2$ reaction. For comparison purposes, the total band radiance (calculated) has been reduced by a factor of 0.63 to allow for the limited system response. This correction was determined from Equation 2-6, using the computed spectrum (Figure A-2) and the relative response function reported in Reference 4.

The results suggest that our calculated values between 90 and 100 km are low by more than an order of magnitude.

Figure 2-32 shows the corresponding results calculated for the 5.4-µm band. They have been corrected for the instrument relative response as described above (see description of Figure 2-27). Corresponding data for this band are not yet available to us.

Figure 2-33 compares the calculated and observed radiance at 3914 Å. In this figure, as well as in the succeeding four figures, we have attempted to extrapolate the four calibrated data points (for both the north- and south-viewing sight paths) to higher altitudes (dashed curves) using the uncalibrated strip charts mentioned above. Although this procedure leads, perhaps, to the correct trend, it should be realized that the magnitudes shown by the dashed curves are by no means certain.

In Figure 2-33, the "hump" in the calculated northern radiance between 95 and 110 km is due to the main arc. A rather similar hump appears in the corresponding data although larger in magnitude by a factor of about 2. This may, indeed, be evidence to support the larger (by a factor of 2) measured flux values (Figure 2-12) for the main arc, instead of those (Figure 2-14) actually used in the calculation. Another alternative, however, is the presence of an "inverted-V" type of drizzle that would serve to broaden and increase the magnitude of the calculated "hump".

Figure 2-32. 5.4-μm brightness (≈horizontal) viewed toward magnetic north and south from Black Brant 18.205-1 on ascent.

Figure 2-33. 3914Å brightness (≈horizontal) viewed toward magnetic north and south from Black Brant 18.205-1 on ascent.

The calculated brightness above 120 km arises primarily from long path lengths through the drizzle region, and the results would appear to be in reasonable agreement with the extrapolated data.

The 5577 Å comparisons shown in Figure 2-34 are not so favorable, especially above 115 km where the extrapolated data appear to decrease faster with increasing rocket altitude. This may be evidence for the presence of too many electrons with energy < 3 keV in our assumed drizzle spectrum. The "hump" in the calculated northern brightness is again due to the main arc and is in reasonably good agreement with the data. As we have mentioned before, however, the production rate of $O(^1S)$ atoms is quite uncertain because the main mechanisms involved in the present calculations are chemical and quenching reactions whose rate coefficients are little more than guesses.

The 5199 Å comparisons shown in Figure 2-35 present an enigma to us. The calculated brightness curves are based on the assumption that the emission is from $N(^2D)$,* with the volume emission rate given by

$$\dot{\Phi}\,(5199) = 1.23 \times 10^{-5}\,[N(^2D)] \quad . \tag{2-7}$$

The portion of the sight path to the north that intersects the main arc occurs at altitudes sufficiently low so that the $N(^2D)$ should be severely quenched by reaction with O_2 (to form NO). As a result, almost all the calculated radiance arises from long paths through the high-altitude portions of the drizzle region. That is why our calculated curve (north) is so flat and shows no arc enhancement. By contrast, the (north-viewing) data clearly show a "hump" at about 100 km, somewhat similar to that exhibited by the 3914 Å data in Figure 2-33. This result would appear to suggest a strong contribution from the arc.

---

* Most of the $N(^2D)$ atoms arise from dissociative recombination with NO^+. Contrary to Table B-1 (Reference 1), the calculations in this report assume that the nitrogen atoms from this source are all in the ^2D state.

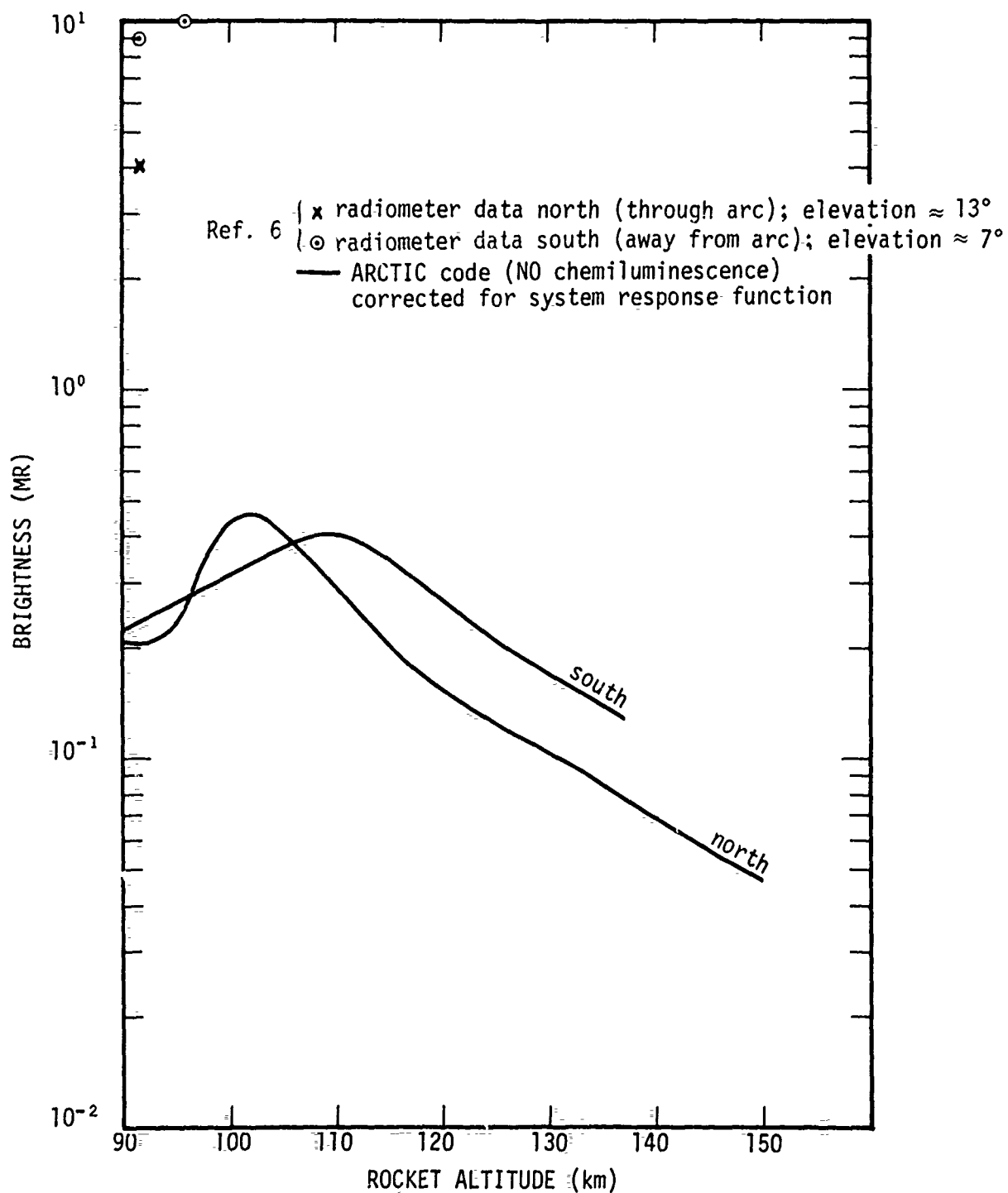Figure 2-34. 5577Å brightness (≈horizontal) viewed toward magnetic north and south from Black Brant 18.205-1 on ascent.

79
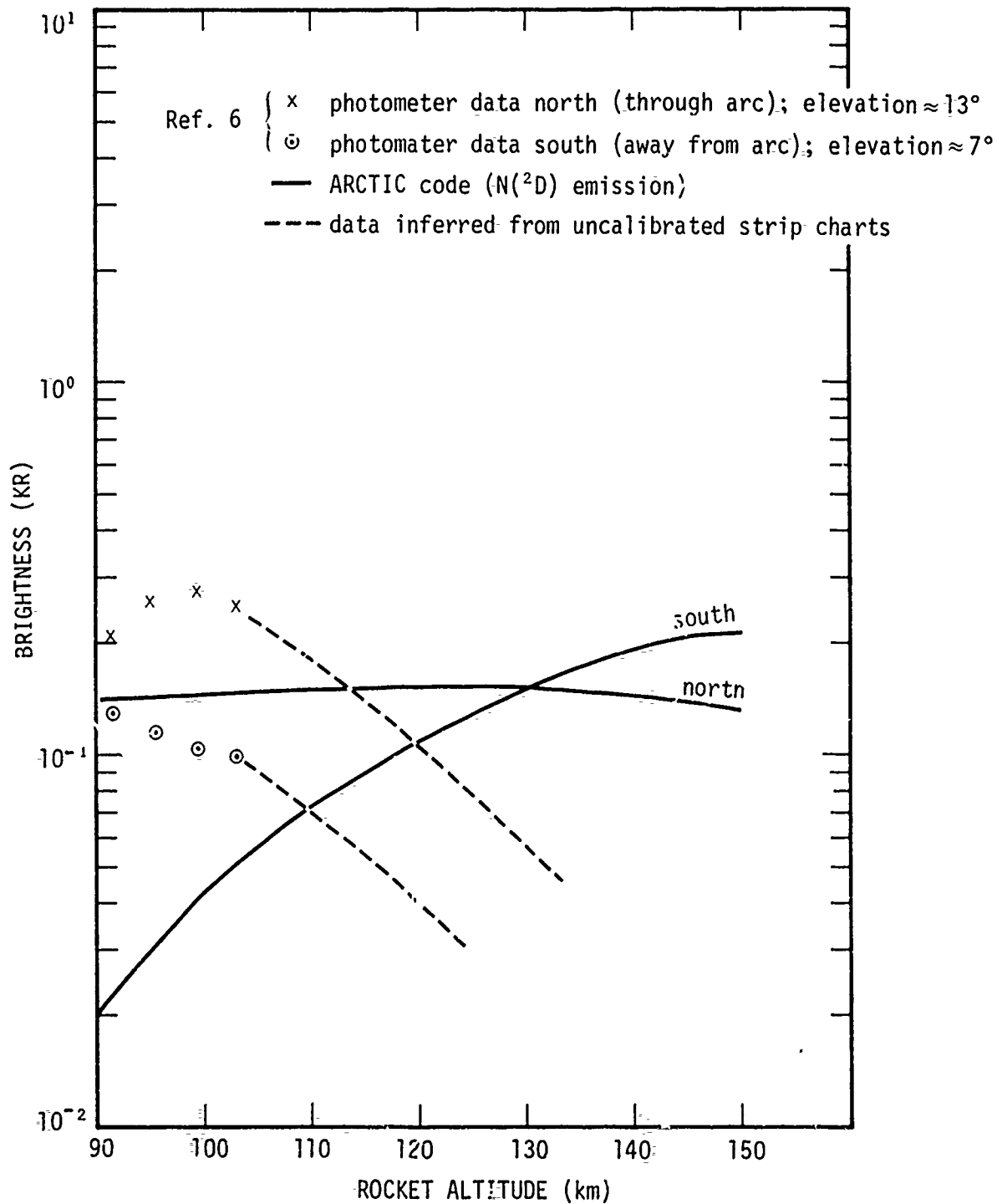
Figure 2-35. 5199Å brightness (≈horizontal) viewed toward magnetic north and south from Black Brant 18.205-1 on ascent.

The calculated brightness to the south shows a monotonic increase with increasing rocket altitude as the sight path traverses regions of increasing $N(^2D)$ concentration. Again, by contrast, the observed (south-viewing) radiance appears to exhibit the opposite character, actually decreasing monotonically with increasing altitude.

Although our model accounts for the magnitude of the 5199 Å emission seen to the north (at least below about 115 km) it clearly does not account for the slope of the observed emission either to the north or the south. The observations seem to imply the presence of a strong low-altitude (~ 100 km) source of $N(^2D)$ both inside and outside the main arc. In this connection we note, as mentioned on p. 63, that such a source would also result in better agreement with the observed zenith radiance at 5.4 μm. Further insight into this problem may be gained when the data for the descent portion of the flight are available.

With respect to the 5199 Å radiation, we have also investigated the possibility that it may arise partly from sources other than $N(^2D)$. The photometer bandpass covers the wavelength interval from about 5195 Å to 5212 Å (Reference 4). Permitted transitions at 5201.8, 5199.5, and 5206.7 Å from N, N^+, and O^+, respectively, fall in this wavelength interval (Reference 25). These emissions can, presumably, be excited by dissociative excitation and/or dissociative ionization. The O^+ emission could also be excited by direct ionization of atomic oxygen. The strongest of the above three emissions is likely to be the first one at 5201.8 Å $(2p^2 5d\,^2P \rightarrow 2p^2 3p\,^2S^0)$ from atomic nitrogen because the energy of the upper state involved (13.98 eV) is considerably lower than that for the other two emissions. In this case the total excitation energy for the dissociative excitation process would be 23.74 eV. The cross section for dissociative excitation of this emission has not been measured. However, if we use, as a guide, the measured dissociative excitation cross section in N_2 for 1177 Å emission (threshold at 23 eV) we find, from the ARCTIC code, brightness curves about 1.3×10^{-2} of

81

those shown in Figure 2-33 for the 3914 $\overset{\circ}{\text{A}}$ emission. This would then provide values in close agreement with the observed 5199 $\overset{\circ}{\text{A}}$ radiance, especially to the north, and would account for the observed "hump" in the data. At the present time, however, this possibility is only a conjecture, because excitation cross sections for the above-cited emissions are not known.[*]

Figure 2-36 shows the comparisons at 3466 $\overset{\circ}{\text{A}}$. The calculations assume that the emission arises from $N(^2P)$. Unfortunately, the production mechanisms (mainly chemical reactions) for $N(^2P)$ are not well known nor, indeed, are the quenching mechanisms. The production and destruction mechanisms assumed here are given in Reference 1.

As in the case of $N(^2D)$, discussed above, our calculations show that the 3466 $\overset{\circ}{\text{A}}$ emission from the side-looking photometer should be dominated by the drizzle region, with only a negligible contribution (along the northern path) coming from the main arc. In the southern direction, our agreement with the low-altitude data is quite good although, at higher altitudes, the larger calculated values may imply, again, an overestimate of our assumed drizzle flux for electron energies < 3 keV. The northern data seem to exhibit the same type of "hump" seen at 5199 $\overset{\circ}{\text{A}}$ and 3914 $\overset{\circ}{\text{A}}$ although, perhaps, not quite so pronounced. It is not clear whether this hump arises from an increased production rate of $N(^2P)$ in the main arc or from an "inverted-V" type of drizzle.

We have also considered the possibility that the 3466 $\overset{\circ}{\text{A}}$ emission may receive contributions from other sources. The photometer bandpass covers the region from about 3450 $\overset{\circ}{\text{A}}$ to 3480 $\overset{\circ}{\text{A}}$ (Reference 4). Included in this region are permitted transitions from O^+ (3471 $\overset{\circ}{\text{A}}$), Ar (3461 $\overset{\circ}{\text{A}}$), Ar^+ (3454 $\overset{\circ}{\text{A}}$), the (4,6) band at 3457 $\overset{\circ}{\text{A}}$ of the O_2 Herzberg I system, the (10,10) band at 3466 $\overset{\circ}{\text{A}}$ of the O_2^+ (I NEG) system, and the (3,4) band at 3469 $\overset{\circ}{\text{A}}$ of the N_2 (2 POS) system. The molecular bands appear to be much too weak to play a part,

---

[*] Furthermore, auroral spectrograms do not clearly show the presence of a line at 3201.8 $\overset{\circ}{\text{A}}$.
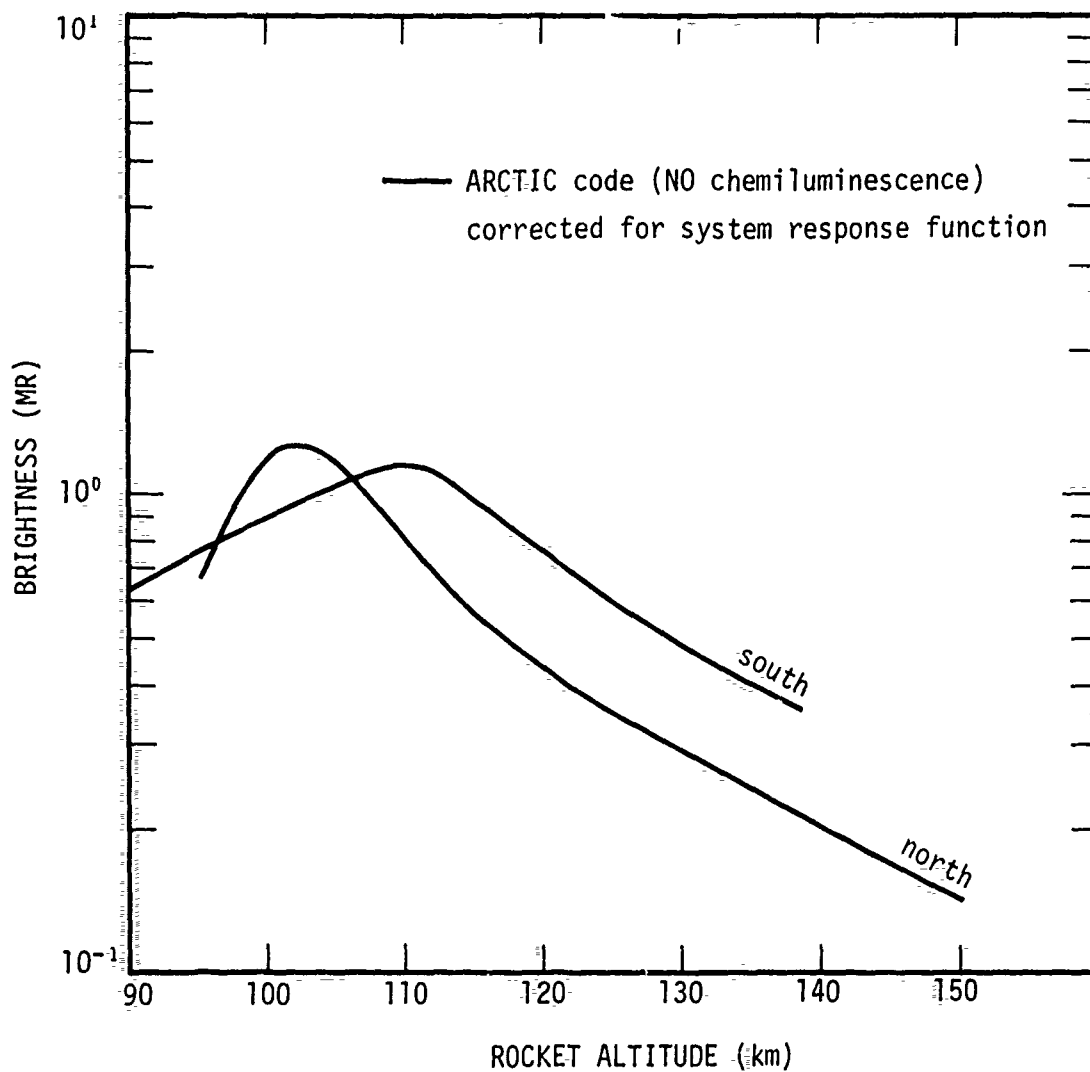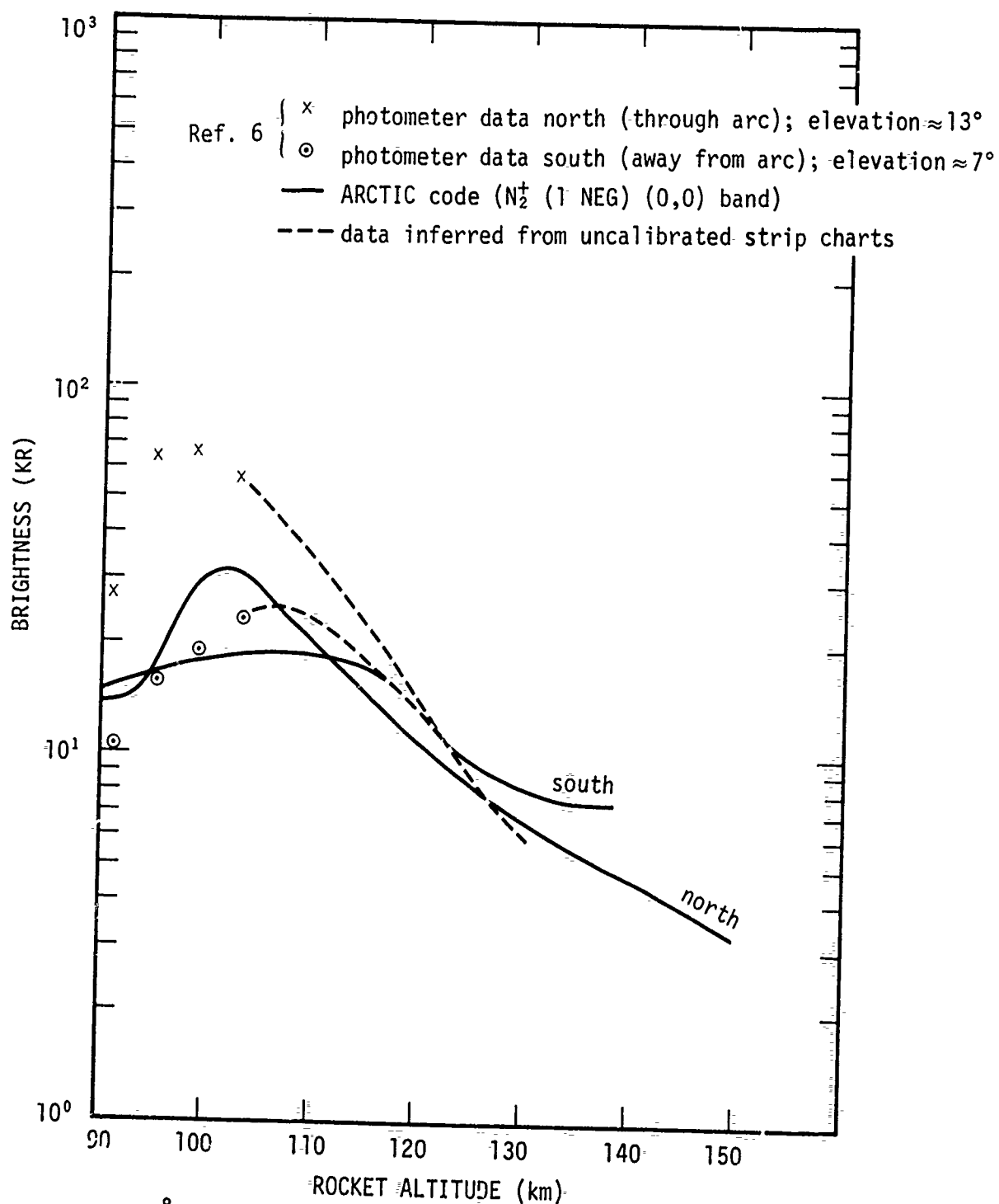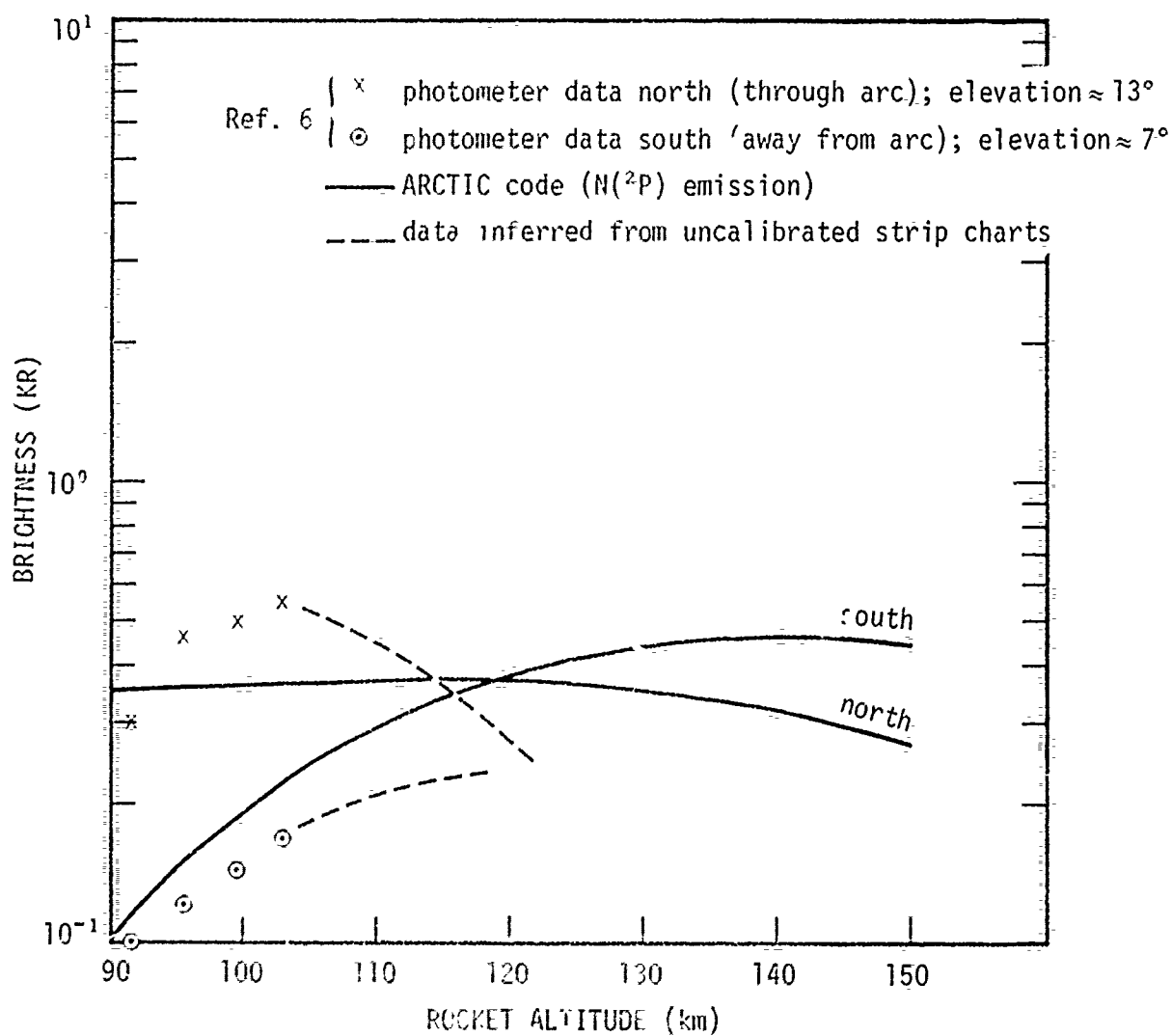
Figure 2-36. 3466Å brightness (horizontal) viewed toward magnetic north and south from Black Brant 18.205-1 on ascent.

although it is conceivable that the atomic lines could contribute. Cross sections for their excitation are not available and we have not attempted to estimate their possible magnitude. However, the possibility of a significant contribution from one or more of these lines cannot be ruled out at the present time.

The comparison at 3800 $\overset{\circ}{A}$, shown in Figure 2-37, is the final one for the side-looking instruments. The calculated brightness is based on emission from the (0,2) band of the $N_2(2\text{ POS})$ system. The shapes of the observed and theoretical curves are roughly similar, although our calculated values are low by factors ranging from about 2 to 5. Again, use of the full particle flux spectrum for the arc (Figure 2-12) would have improved the agreement.

Figure 2-38 shows the calculated electron temperature, T_e, as a function of rocket altitude. The values at altitudes between about 108 and 140 km correspond to those in the arc; other values are those appropriate to the assumed drizzle region. Data are not yet available for comparison. Also shown in Figure 2-38 is the adopted profile of the neutral gas temperature.

If the full measured arc flux (Figure 2-12) had been used as input to the ARCTIC code, the calculated values for T_e in the arc would have been larger than those shown in Figure 2-38.

A comparison between the calculated ion concentrations on rocket ascent and the mass spectrometer data of Narcisi (Reference 16) is shown in Figure 2-39. The jagged appearance of the data is modulation due to rocket spin; their absolute values were obtained by normalization to the electron density profile deduced from the plasma frequency probe (Reference 16).
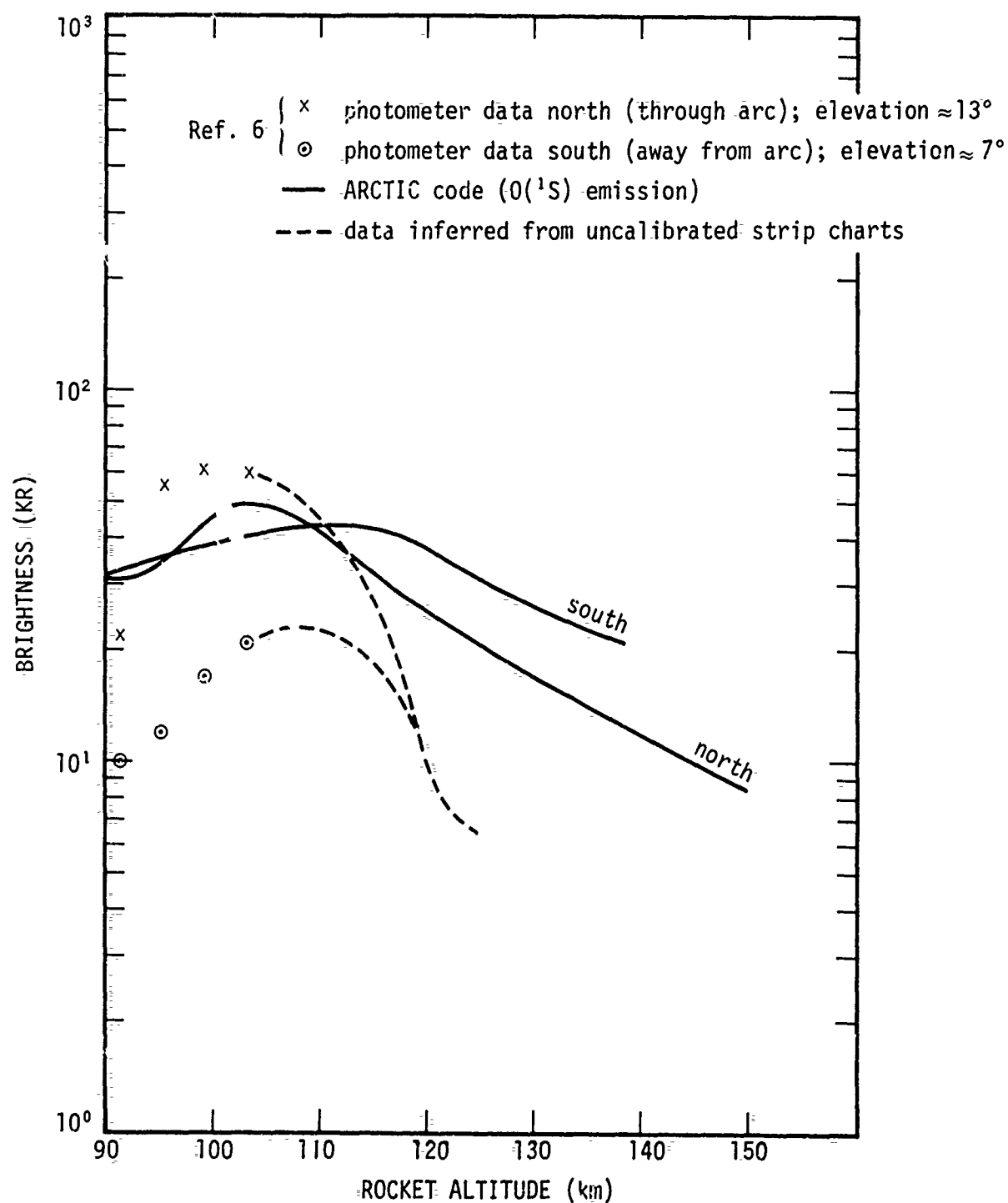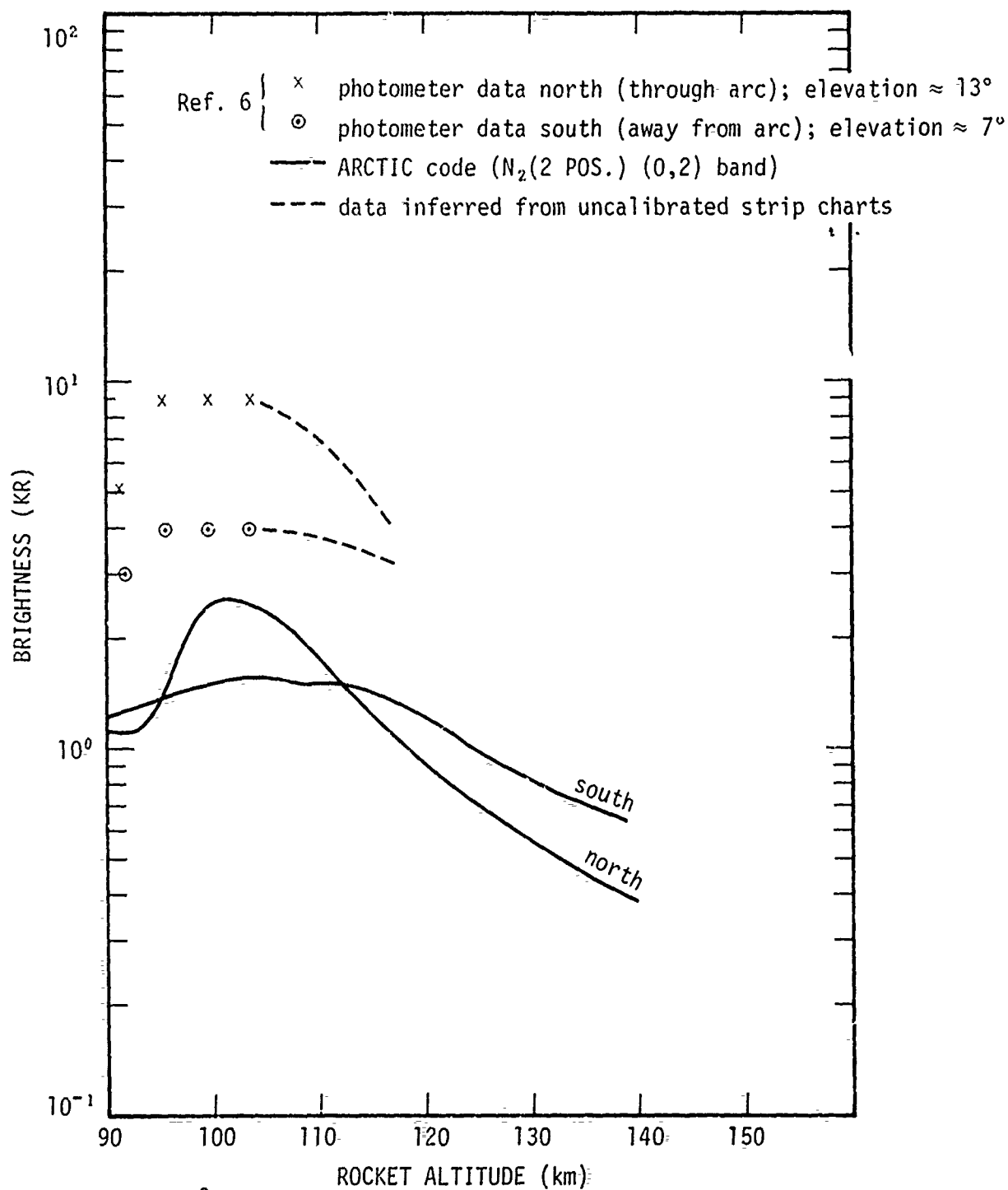
Figure 2-37. 3800Å brightness (~horizontal) viewed toward magnetic north and south from Black Brant 18.205-1 on ascent.
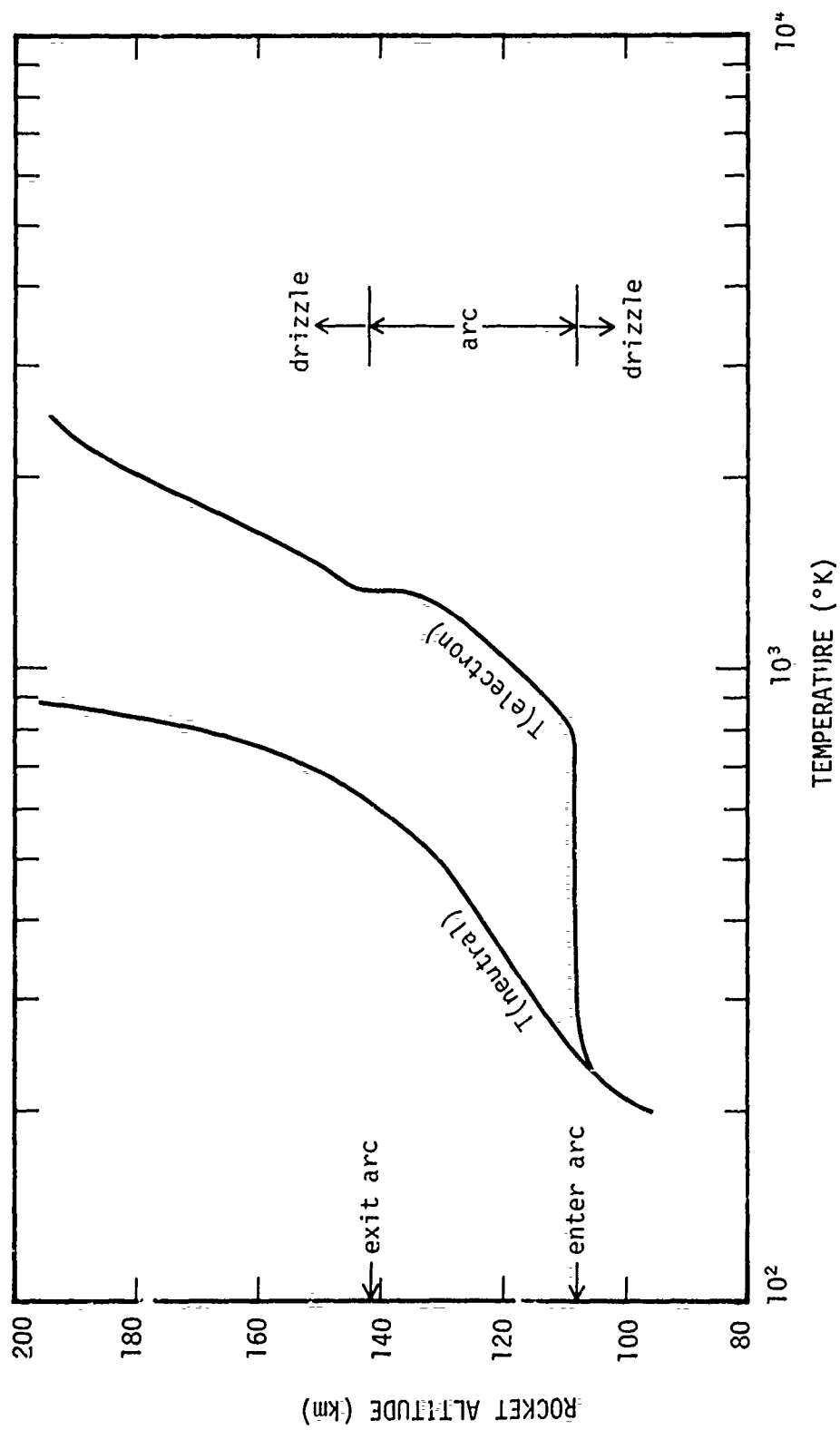
Figure 2-38. Calculated electron temperature at rocket (Black Brant 18.205-1) location on ascent.
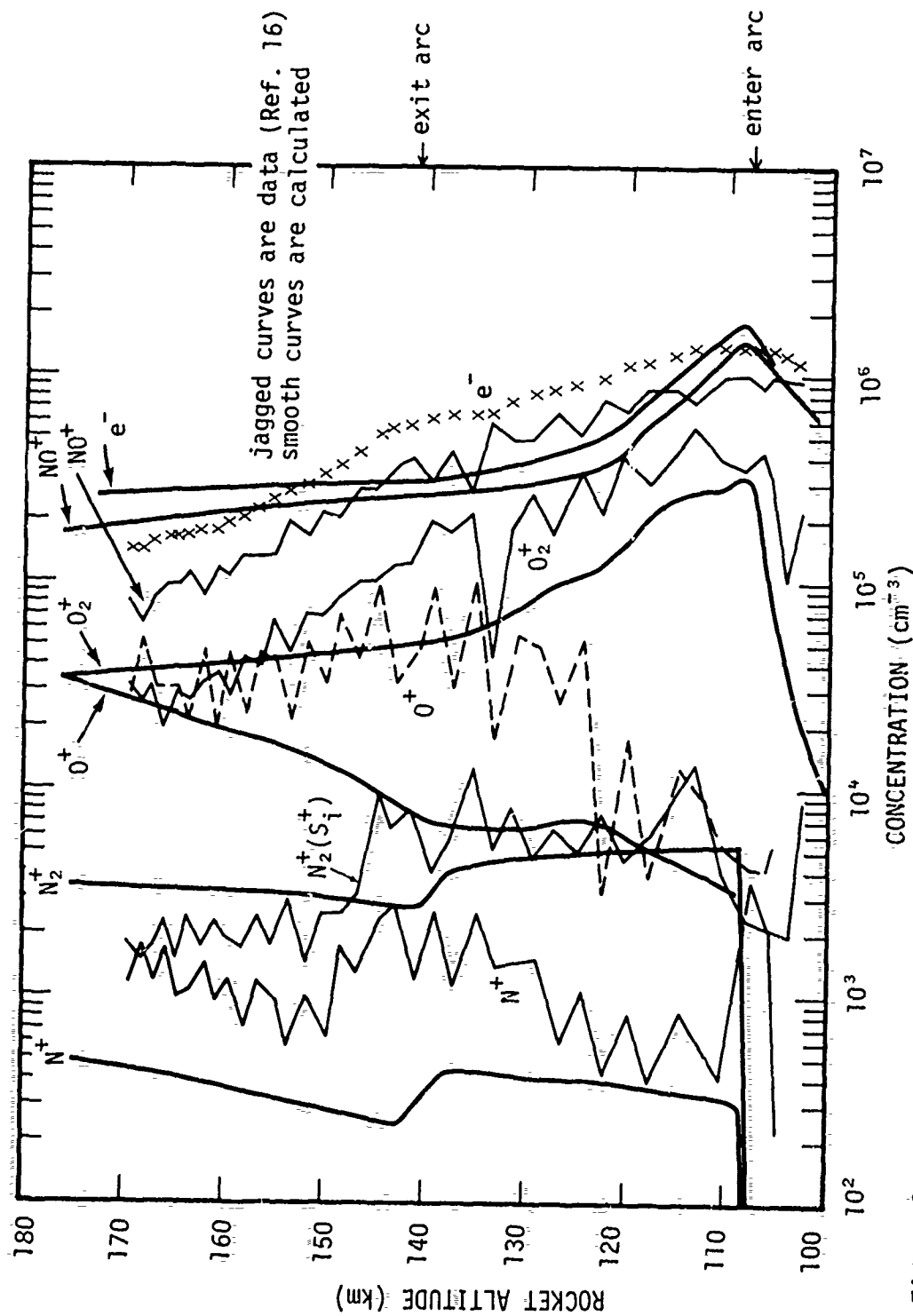
Figure 2-39. Ionization as a function of rocket (Black Brant 18.205-1) altitude on ascent; data and calculations compared.

Before describing the comparisons shown in Figure 2-39, we empha-
size again the fact that the computed concentrations are based on chemistry
times, at each point, determined by the effective duration of the electron
flux. This time, in turn, depends on the geometry and velocity of the arc
as well as on the type, strength, and prior history of the drizzle. The
electron density, in fact, is rather sensitive to these parameters which, as
we have pointed out before, are not at all well established.

Consider now the computed and observed electron density profiles
shown in Figure 2-39. Below about 112 km, the agreement is reasonably good.
Between about 115 and 150 km, however, the theoretical values are lower
than the measured ones by as much as a factor of 2; above 152 km they exceed
the measured values. As we noted earlier, energy deposition above about
120 km occurs mainly by electrons with energies < 3 keV. This is precisely
the region where particle flux data are absent. Our assumed primary
spectrum (Figure 2-14) for this region is a pure guess. The measured
electron density profile above 115 km in the arc (Figure 2-39) suggests that
the arc flux spectrum should increase toward lower energies below 3 keV
(in Figure 2-14) rather than decrease as we have assumed. On the other hand,
the rather abrupt change in slope of the measured profile (unlike that for
the calculated curve) at about 145 km, after the rocket has left the arc,
suggests that we have overestimated the flux of low-energy primary electrons
in the drizzle spectrum (Figure 2-8).

In summary, several factors combine to render calculation of the
ion and electron concentrations uncertain, especially above about 120 km.
These include (1) the unknown incident flux of electrons with energy < 3 keV,
(2) the unknown history of prior electron bombardment, and (3) the uncertain
geometry and dynamics of the arc itself.

88

The lower (calculated) values of the electron density above about 112 km in the arc may also suggest that the full flux values (Figure ?-12) should have been used rather than the reduced (by a factor of 2) ones actually employed. This would have increased the calculated values of electron density by about $\sqrt{2}$, although the resulting values near 108 km would then be nearly a factor of 2 larger than those measured.

The foregoing remarks are also apropos to a description of the ion concentrations. The "kinks" that occur in the calculated N^+, N_2^+, and O^+ profiles at ~ 140 km, as the rocket leaves the arc, are also seen in the data, but they then occur at a somewhat higher altitude and are not so pronounced. This is probably due to the spatial variation of the drizzle near the main arc.

Figure 2-40 compares the $[NO^+]/[O_2^+]$ ratio on rocket ascent. The calculated values on rocket descent in the drizzle region are also shown. The comparison shows that the calculated ratios are somewhat higher than the measured ascent values.

It can be shown (see, for example, Reference 15) that, in equilibrium, the $[NO^+]/[O_2^+]$ ratio is dominated by the quantity $k_1[NO]/(k_2 n_c)$ where n_c is the electron density, and k_1 and k_2 are rate coefficients for the reactions

$$O_2^+ + NO \rightarrow O_2 + NO^+$$

and

$$NO^+ + e \rightarrow N + O \qquad ,$$
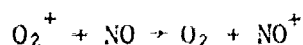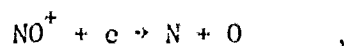
respectively. Larger values for n_c and/or smaller values for $[NO]$, therefore, would serve to lower our ratios more in line with the data. As we have discussed earlier, use of the full particle flux (Figure 2-12) would, indeed, increase the calculated values for n_c and improve the agreement. As for the NO concentration, large uncertainties are inherent in its determination

89
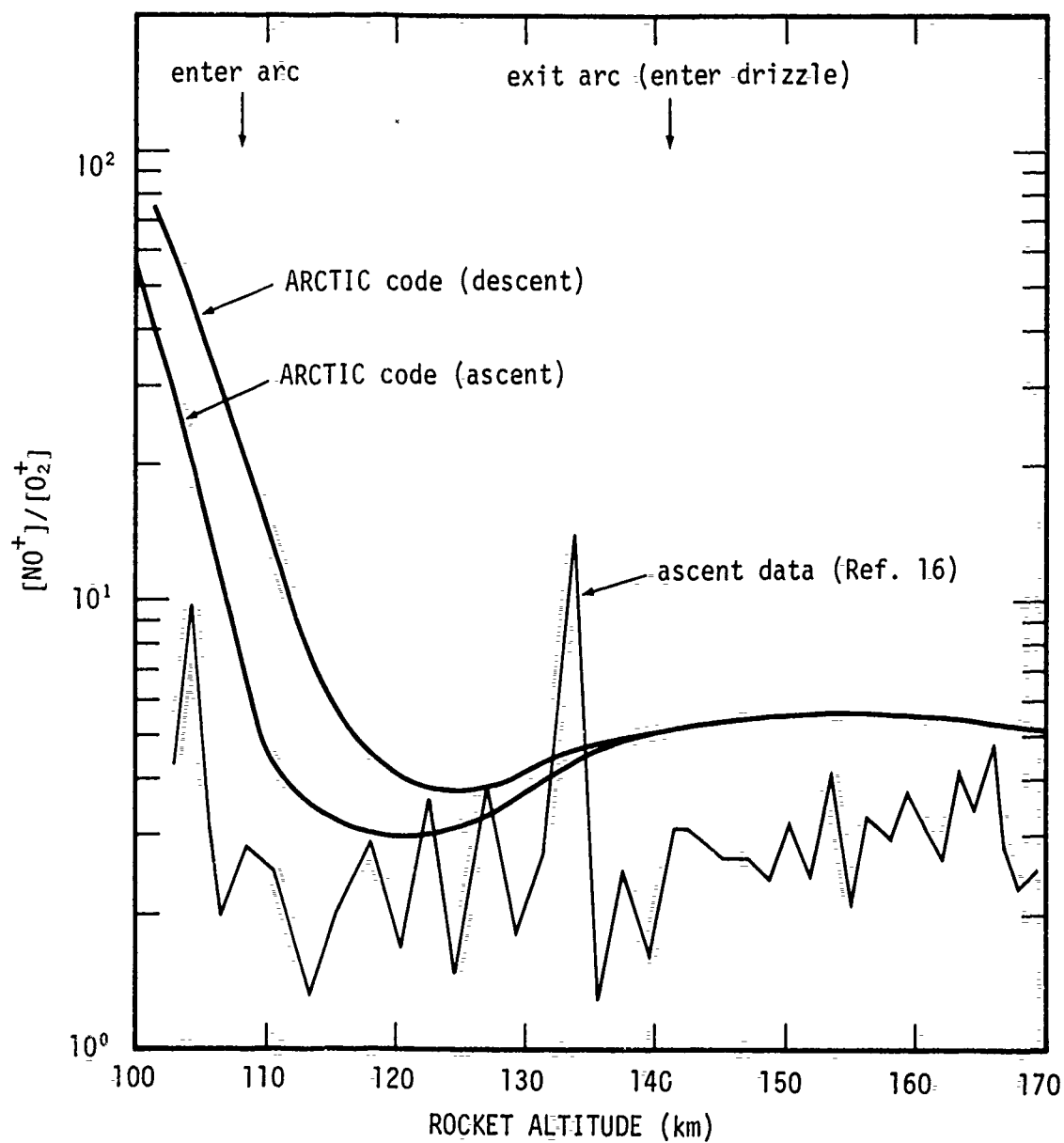
Figure 2-40. $[NO^+]/[O_2^+]$ ratio as a function of rocket (Black Brant 18.205-1) altitude; data and calculations compared.

(as previously described) because its magnitude depends on the prior bombardment history (see Figure 2-10). The assumed "initial" profile of [NO] prior to onset of the drizzle (Figure 2-11) is somewhat arbitrary. A different profile would have resulted in different values for the $[NO^+]/[O_2^+]$ ratio.

The sensitivity of the $[NO^+]/[O_2^+]$ ratio to the strength and duration of the bombardment flux is illustrated in Figure 2-41. This figure shows how the ratio varies with time at an altitude of 103.5 km under the following conditions: After 30 minutes of continual drizzle bombardment, the arc flux is turned on at $t = 0$ sec and remains on for 8.2 sec. At 8.2 sec the arc is turned off but the drizzle remains on. The results can be described as follows. At $t = 0$, the arc flux ionizes O_2 and drives the $[NO^+]/[O_2^+]$ ratio down from its initial value of about 55 to a low of less than 2 when charge transfer with NO brings it back to a stabilized arc value of about 6. When the arc flux is removed, $[O_2^+]$ decreases by charge transfer with NO faster than the NO^+ can decrease by dissociative recombination and the ratio is then driven to values exceeding 100. Although not shown in Figure 2-41, the ratio must eventually (~ 10 sec) settle back to its steady state drizzle value of about 55.

In view of the uncertainties associated with the bombardment history of the region, agreement much better than that shown in Figure 2-40 can hardly be expected.
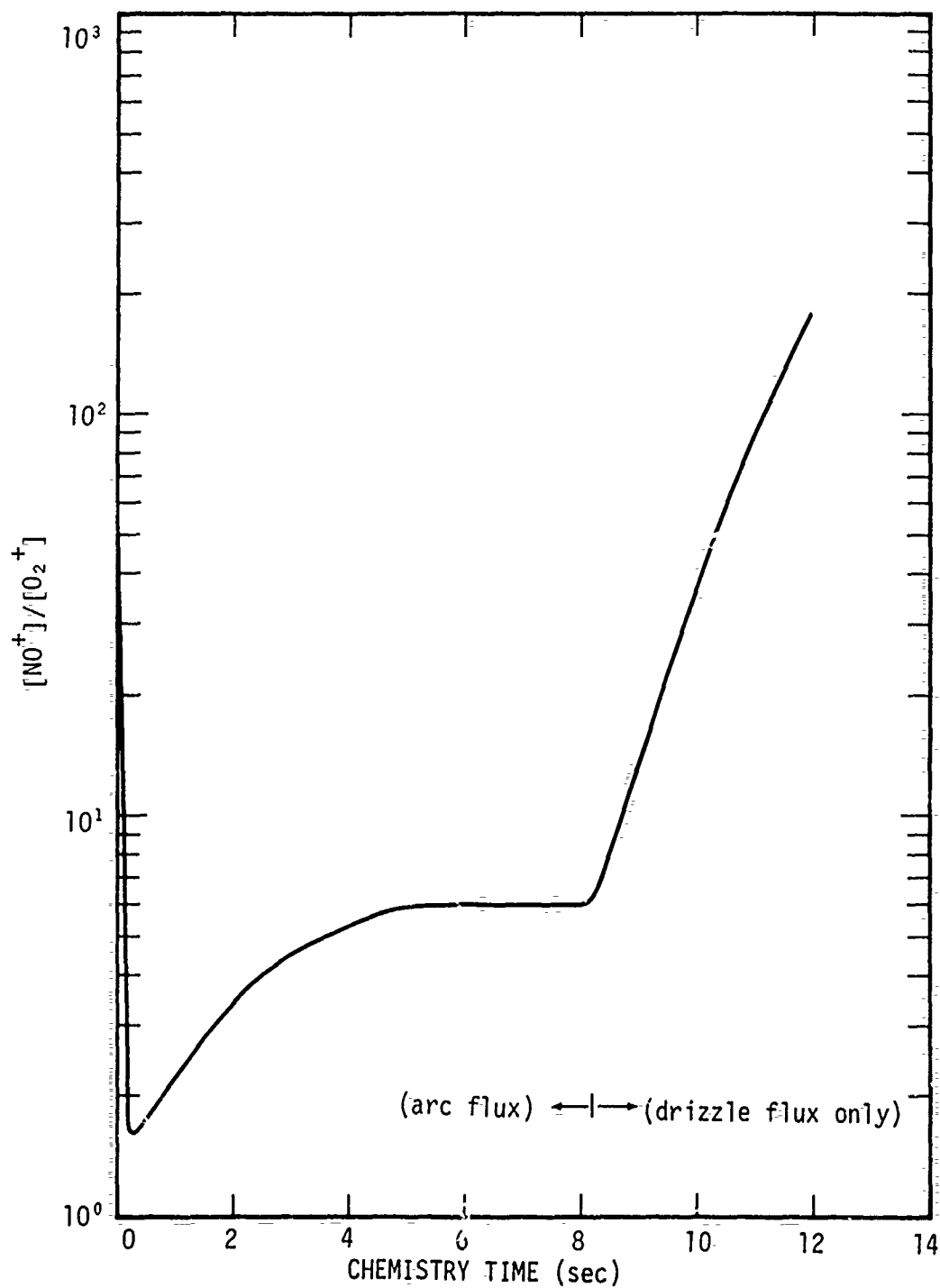
Figure 2-41. Time history of $[NO^+]/[O_2^+]$ ratio at 103.5-km altitude in drizzle environment when arc flux on from t = 0 to t = 8.2 sec.

Summary and Conclusions

A summary of our work and conclusions, based on a study of the auroral event of 27 March 1973 near Poker Flat, Alaska, is presented below. It should be emphasized that the data upon which much of this work was based have not yet been formally published, but have been made available to us on a preliminary (subject to change) basis. Consequently, the conclusions should likewise be considered preliminary, pending final confirmation of the data.

The summary and conclusions are as follows:

(1) The event consisted of a thin arc (~ 5 km thick) with IBC coefficient at least II+, imbedded in a surrounding drizzle region approximately 850 km in north-south extent. The arc moved erratically north and south in a region between Ester Dome and Fort Yukon, irradiating the atmosphere in a manner, ill-defined, except in the limited air space surrounding the rocket trajectory.

(2) A model to describe the event, including the arc geometry, dynamics, and accompanying drizzle environment, was devised. The ARCTIC code was run, for this model environment, and comparisons were made with the preliminary data.

(3) Data from the upward-viewing rocket-borne 3914 $\overset{o}{A}$ photometer are inconsistent with the particle flux measurements. Either the particle flux is too high by a factor ≈ 2, or else the photometer data are low by a corresponding amount. Ground-based photometer measurements, uncorrected for transmission losses, support the rocket photometer data. However, if the ground-based data are corrected for Rayleigh scattering and aerosol extinction, the weight of evidence shifts more in favor of the particle flux data. Comparison with data from other rocket-borne instruments (especially

the side-looking 3914 Å and 3800 Å photometers) lends additional support to the particle data and suggests that the (zenith) 3914 Å rocket data are in error.

(4) The calculated zenith radiance near 4.3 μm is about four times lower than the (ascent) CVF spectrometer data below 100 km, although the agreement is reasonably good for rocket altitudes between 105 and 112 km on ascent and also for altitudes down to 90 km on rocket descent. Agreement with the (zenith) radiance data from the dual channel radiometer (4.3 μm), however, is not so good, with the observed brightness above 120 km about 20 times larger than the calculated values. The apparent constancy of the radiometer data above 120 km with increasing rocket altitude remains unexplained.

(5) The zenith radiance observed near 5.4 μm, with both the rocket-borne CVF spectrometer and the dual channel radiometer is not significantly different on ascent (through the arc) and descent (outside the arc). This contrasts with the calculated results that show a much higher relative brightness from the arc than from the drizzle region outside the arc. Furthermore, the observed brightness is about an order of magnitude larger than the theoretical values. The data seem to suggest the presence of a source for vibrationally excited NO, both inside and outside the arc, much greater than the calculated $N(^2D) + O_2$ reaction can provide.

(6) Data at 5.4 and 2.7 μm from the side-looking rocket-borne radiometer are contaminated with thermal emission from ejected instrument covers. However, the detected radiance at 2.7 μm that is (believed to be) aurorally produced, is at least an order of magnitude larger than our theoretical values. This appears to be consistent with the discrepancy noted in Item 5 above.

(7) Rocket data at 5199 Å are hard to reconcile with the calculated $N(^2D)$ emission. Suggested possibilities are (i) an additional strong source of $N(^2D)$ operating at low altitudes (~ 100 km) inside and

94

outside the arc (which would also be consistent with Items 5 and 6 above), (ii) contributions from direct excitation of permitted line radiation (N, N^+, O^+) that falls within the bandpass of the photometer. Dissociative excitation of such emissions appears plausible.

(8) The shape of the observed (northward) 3466 Å radiance curve is also somewhat difficult to reconcile with the calculated $N(^2P)$ emission. Additional sources for $N(^2P)$ within the arc, or contributions from other sources, are suggested.

(9) Comparison with the observed electron density profile, and also with the zenith radiance at 3914 Å, implies that our assumed particle spectrum at energies < 3 keV contains too few electrons in the main arc and too many electrons in the drizzle region.

$O_2(^1\Delta)$ EMISSION

Enhancement of $O_2(^1\Delta)$ emission (1.27 μm) in auroras has been the subject of controversy for several years. No data at 1.27 μm are available from the ICECAP program. However, we have made a comparison between the calculated emission from $O_2(^1\Delta)$ for the auroral arc of 27 March 1973 with observations reported in the literature by Gattinger and Vallance Jones (Reference 26) for a different auroral event that occurred on 27 January 1973.

Although the two events are different, one having occurred near Poker Flat, Alaska, the other at Fort Churchill, Manitoba, the Poker Flat event was evidently more intense and so, presumably, for equal deposition times, it would give rise to at least as much emission from $O_2(^1\Delta)$ as would the weaker event. It is instructive to see if this premise is indeed correct and whether electron bombardment can account for the observed enhancement of 1.27-um emission.

Observations were made (toward the zenith) from the ground at 5577 Å and at 1.27 μm into IBC Class II+ activity. The 5577 Å emission was irregular, but can be described approximately as having a peak intensity of about 50 KR near onset and a subsequent exponential decay with a time constant ~15 minutes. For comparison, we note that the observed (and calculated) zenith intensity at 5577 Å for the Poker Flat arc was about 70 KR. Therefore, if we perform our calculations for the Poker Flat arc and allow the flux to decay in the exponential manner described above, the results should overestimate the 1.27-μm enhancement produced by precipitating electrons for the Fort Churchill event.

The significant processes controlling the concentration of $O_2(^1\Delta)$ above about 100 km are believed to be electron excitation*

$$e + O_2(X^3\Sigma) \rightarrow e + O_2(a^1\Delta) \qquad (2-8)$$

and radiative deexcitation

$$O_2(a^1\Delta) \rightarrow O_2(X^3\Sigma) + h\nu \qquad . \qquad (2-9)$$

Collisional quenching by $O_2(^1\Delta)$ with a rate constant of about $2.4 \times 10^{-18} cm^3$ sec^{-1} should not be important above about 90 km. Thus, ignoring any transport effects, the concentration of $O_2(^1\Delta)$ is determined by the simple equation

$$\frac{d}{dt}[O_2(^1\Delta)] + A[O_2(^1\Delta)] = q(t) \qquad . \qquad (2-10)$$

Here, A is the radiative decay rate $(2.5 \times 10^{-4} sec^{-1})$, and $q(t)$ is the volume excitation rate $(cm^{-3} sec^{-1})$ of $O_2(^1\Delta)$.

---

* Chemical excitation has also been proposed (Reference 27).

In accordance with observations, we take

$$q = q_0 \, e^{-\alpha t} \qquad . \tag{2-11}$$

The solution to Equation 2-10 is then

$$[O_2(^1\Delta)] = \frac{q_0}{A - \alpha} \, (e^{-\alpha t} - e^{-At}) \qquad . \tag{2-12}$$

A decay time of 15 minutes for the source implies $\alpha = 7.7 \times 10^{-4} \, \text{sec}^{-1}$. With this value for α, Equation (2-14) then provides a peak concentration for $O_2(^1\Delta)$ (and emission rate at 1.27 μm) about 35 minutes following auroral onset. This is consistent with the observations of Gattinger and Vallance Jones (Reference 26).

The volume emission rate in the (0,0) band at 1.27 μm is given by

$$\dot{\phi}(1.27 \ \mu\text{m}) = A_1 [O_2(^1\Delta)] \tag{2-13}$$

where A_1 is the transition rate for the (0,0) band (2.55 $\times 10^{-4} \, \text{sec}^{-1}$). Thus, the intensity seen from the ground is

$$\begin{aligned} I(1.27 \ \mu\text{m}) &= \eta \int_0^\infty \dot{\phi}(1.27 \ \mu\text{m}) \ dz \\ &= \left(\frac{A_1}{\alpha - A}\right)\eta \ (e^{-At} - e^{-\alpha t})\int_0^\infty q_0 \ dz \end{aligned} \tag{2-14}$$

where η is the transmission factor.

Calculations by Evans et al., (Reference 28) as well as estimates based on the calculations of McClatchey and Selby (Reference 29) suggest that $\eta \approx 0.05$. From the ARCTIC code, we also find

$$\int_0^\infty q_0 \ dz = 2.0 \times 10^{11} \ (\text{cm}^{-2} \ \text{sec}^{-1}) \qquad . \tag{2-15}$$

97

Equation 2-14, together with the parameter values cited above lead to the results shown in Figure 2-42. Shown for comparison are the observations of Gattinger and Vallance Jones. The measured maximum ground enhancement at 1.27 μm is seen to be about 5 times larger than that calculated. The two curves can be brought into approximate agreement if it is assumed that the transmission factor is > 0.25. However, the weight of evidence seems to preclude such a large value for η.

Although our calculation was not based on the precise environmental conditions prevailing at the time of the ground measurements, the results, nevertheless, suggest that electron bombardment alone is insufficient to account for the magnitude of the observed enhancement at 1.27 μm.
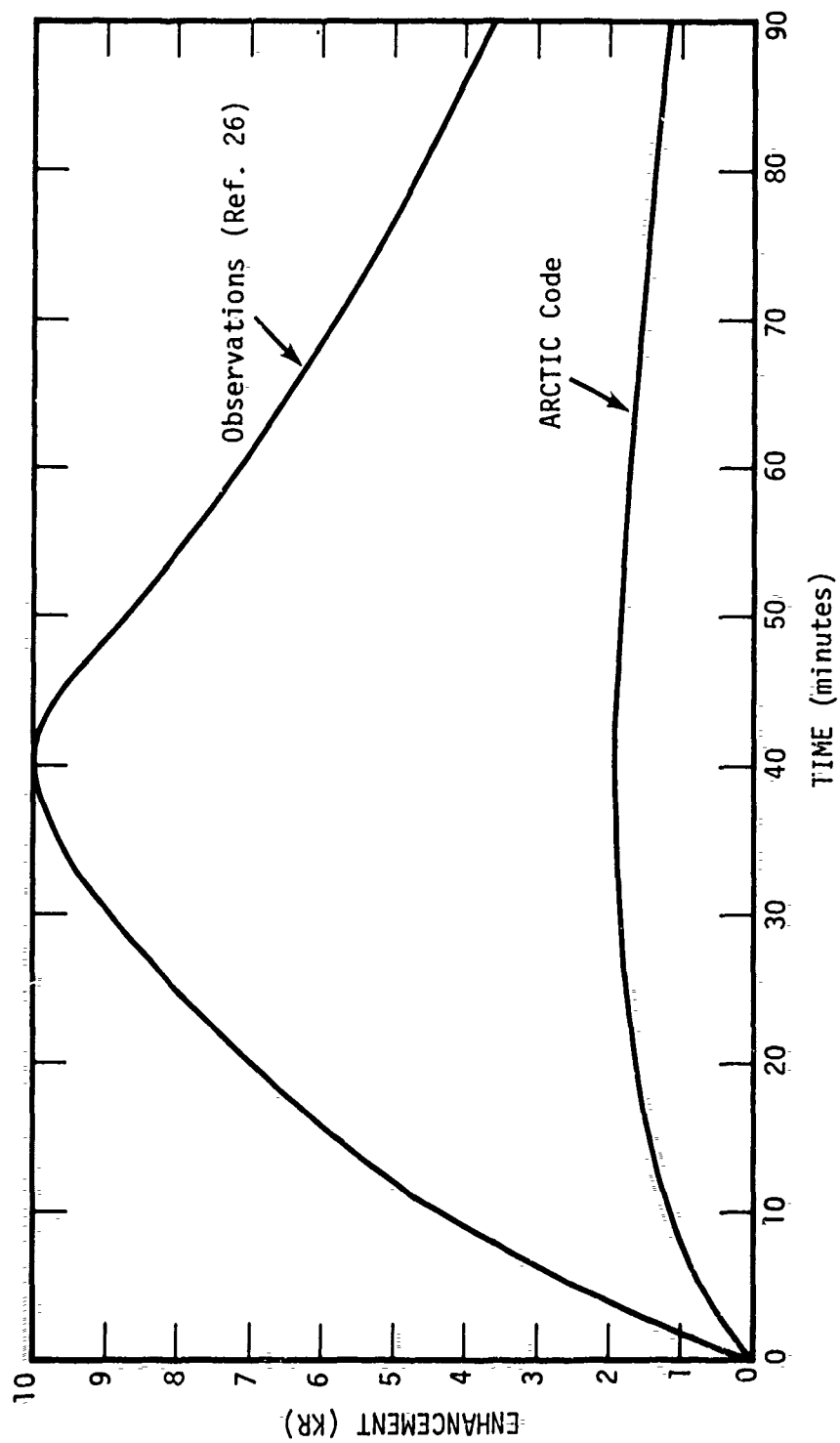
Figure 2-42. Auroral enhancement of $O_2(^1\Delta)$ emission (1.27 μm) ; ground-based observations and calculations compared.

99

SECTION 3
STUDIES RELATED TO LWIR PRODUCTION
AND TO EUV EFFECTS IN THE AURORA

Part of the work performed under the present contract has been a
continuation of the efforts initiated previously (Reference 1) with respect
to effects produced in the atmosphere by ultraviolet (UV) and extreme
ultraviolet (EUV, $\lambda \lesssim 1000$ Å) radiation generated by auroral electrons.
The motivation for these studies was twofold. First, if trapping of a
sizeable fraction of the EUV radiation in high-lying states occurs, as has
been suggested by Zipf (References 30 to 33), then leakage of energy into
the LWIR might be significant. In particular, we sought to explore the
possibility that such leakage could account for the spectral band features
observed near 8, 9.2, and 12 µm in ICECAP and other auroral experiments.
Second, if the chemistry and emission properties of auroral arcs are signi-
ficantly altered by absorption of these short wavelength radiations, as
has also been suggested by Zipf, then a proper interpretation of ICECAP
and other auroral data would have to make allowance for such effects.

A brief account of the work performed and conclusions reached in
these two areas is now presented.

LWIR EMISSION FROM ELECTRONIC TRANSITIONS IN N_2

Our efforts to account for the LWIR features (near 8, 9.2, and
12 µm) observed at high altitudes in certain rocket experiments (References
34, 35) have centered upon a study of the high-lying states of the N_2
molecule. It was felt that N_2, being the dominant molecular species, would

100

be the most likely source of EUV and, possibly, of the observed LWIR bands that might arise from transitions between closely adjacent states at high energies.

The states of N_2 that we surveyed are described and tabulated in Reference 1 (Tables 5 and 6). Over 200 states at energies above 12.4 eV were assembled, mainly from UV absorption data. Differences were taken between those states, connected by allowed transitions, that might give rise to the observed LWIR features. A considerable number of possibilities were found, although the uncertainty in wavelength of many of them is large because the uncertainty in energy of the levels involved is often as great as the energy of the LWIR photons themselves.

The conclusions we have come to, based upon a further study of the states involved, are as follows:

(1) With the possible exception of the (0,1) band of the $w^1\Delta_u \to a^1\Pi g$ system (9.5 µm) no states at energies below about 12 eV appear capable of generating the observed bands. Even the above band is usually weak or absent under dc discharge conditions in N_2 (Reference 36) and is, therefore, an unlikely candidate.

(2) Most of the states observed in UV absorption studies that lie above about 12 eV, but below the first ionization limit at 15.6 eV, are strongly predissociated (Reference 37). Those states that are observed in emission (and hence not predissociated) do not have suitably adjacent states with which to connect to produce the observed LWIR bands.

(3) For states lying above the first ionization potential, high resolution absorption studies have shown that the rotational lines involved, although varying in width, are of the order of 0.01 to 0.1 Å wide (Doppler width ≈ 0.002 Å). This corresponds to lifetimes of $\sim 10^{-11}$ to 10^{-12} sec and implies that the states are strongly autoionized and/or predissociated (Reference 38).

101

If leakage of trapped EUV energy into the LWIR is to account for the observed features, then not only should suitably adjacent states exist in the molecular system, but also the cross sections for UV absorption into and radiation from them should be large. The foregoing observations, however, appear to preclude the satisfaction of these conditions, and we conclude that the N_2 molecule is not the source of the LWIR features.

The attempts outlined above to explain the LWIR bands were predicated on the assumption that they are aurorally produced. However, observation of the features under aurorally quiet conditions above Poker Flat, Alaska in February 1974 suggests that this may not be the case. Consequently, no further study of the bands was made pending clarification of the circumstances surrounding their occurrence.

UV GENERATION AND ITS EFFECTS ON 5577 Å EMISSION

The generation of UV and EUV radiation by precipitating auroral electrons, and the subsequent effects upon the chemical and optical properties of auroras, is not well known, to say the least. Good laboratory and field data on the EUV spectrum are much needed for this purpose. References 39 to 41 give some information, but it is far from adequate. The expected data from the University of Pittsburgh are not yet available. Consequently, firm conclusions regarding the importance of the effects cannot yet be made.

We have, nevertheless, performed a cursory investigation of certain aspects of the problem. First, an attempt was made to estimate the fraction of precipitated electron energy that may go into EUV radiation by studying the energy partition calculated using the ARCTIC code. This is, admittedly, rather crude because the cross sections for excitation of the higher-lying states of the major species are not well known nor, indeed, is the ultimate fate of the excitation energy. Second, we have considered the influence of

EUV radiation on the excitation of $O(^1S)$ and the subsequent emission at 5577 Å. This green-line emission from atomic oxygen is a standard reference in auroral work, including the ICECAP program, and it is important, therefore, to understand the mechanisms involved in its generation.

A brief summary of the results of this work are as follows:

Estimated Fraction of Precipitated Electron Energy
Radiated at $\lambda \leq 1000$ Å.

In order to estimate the fraction of precipitated electron energy radiated in the EUV above 100 km, the ARCTIC code was used to calculate the energy partition resulting from the stopping of primary electrons in an air mixture consisting of 73% N_2, 14% O_2, and 13% O. This mixture corresponds to an altitude of about 120 km.

The partition into 187 different states was determined for primary electron energies ranging from 1 eV to 100 keV. The detailed results are not presented here, although a somewhat condensed version for an N_2/O_2 mixture is shown in Table 2-1.

The history of many of the states following their excitation is not well known. States of N_2 and O_2 that predissociate and preionize may ultimately lead to radiation from the product atoms or atomic ions. The fraction of such energy radiated and its spectrum are presently unknown. Fortunately, however, only a relatively small part of the incident electron energy is deposited in states such as these.

Table 3-1 is our best guess of the fraction of energy radiated in the EUV and the approximate wavelengths involved. It is based on the partition determined for the stopping of a 10 keV electron, although the detailed partition is actually rather insensitive to the primary energy for

103

values above about 1 keV. Most of the radiation is seen to arise from Rydberg transitions in N_2 and from the $b'^1\Sigma_u^+$ state of N_2. The indicated fraction radiated by the latter state is probably an upper limit because some of the higher vibrational states associated with it are not observed in emission and are evidently predissociated. Direct excitation of atomic oxygen appears to contribute only negligibly to the EUV.

The conclusion from the foregoing (rather crude) analysis is that not more than about 10 percent of the precipitated electron energy is radiated in the EUV.

Table 3-1. Estimated fraction of incident electron energy (10 keV) radiated in the EUV.

Wavelength ($\overset{\circ}{A}$)	Radiating Species	Process	Fraction Radiated
900-970	$N_2(b'^1\Sigma_u^+)$	direct excitation	1.7^{-2} (upper limit)
~ 960	N_2 (Rydberg)	direct excitation	6.0^{-2}
~ 865	N_2 (Rydberg)	direct excitation	1.8^{-2}
916	N^+	dissoc. ioniz. of N_2	1.4^{-3}
776	N^+	dissoc. ioniz. of N_2	7.7^{-4}
747	N^+	dissoc. ioniz. of N_2	5.6^{-4}
672	N^+	dissoc. ioniz. of N_2	6.3^{-4}
533	N^+	dissoc. ioniz. of N_2	4.9^{-4}
879	0	dissoc. excit. of O_2	9.0^{-5}
990	0	dissoc. excit. of O_2	1.8^{-4}
833	O^+	dissoc. ioniz. of O_2	2.1^{-4}
717	O^+	dissoc. ioniz. of O_2	9.2^{-5}
		TOTAL	$\approx 1.0^{-1}$

Possible Effects of EUV radiation on 5577 Å Emission

Two possible effects of EUV radiation on the 5577 Å emission from atomic oxygen were considered. One deals with the peculiar observations reported by Romick and Belon (Reference 3-13) that shows that the thickness of an auroral arc measured at 5577 Å is only about half as large as that measured at 3914 Å. The other deals with the importance of $O(^1S)$ excitation by photodissociation of O_2 as compared to other excitation mechanisms.

Arc Width at 5577 Å

Auroral excitation of $O(^1S)$ and subsequent emission of the 5577 Å line is normally considered to arise from a combination of direct plus chemical processes. The ARCTIC code, for example, predicts that nearly half of the excitation arises from the quenching reaction

$$N_2(A^3\Sigma_u^+) + O(^3P) \rightarrow N_2(X^1\Sigma_g^+) + O(^1S). \qquad (3-1)$$
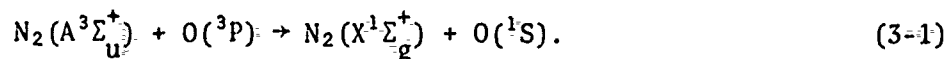
Most of these processes, however, including Reaction 3-1, should produce an excitation rate nearly proportional to the energy deposition rate. This means that the emission rate from $O(^1S)$ should be nearly proportional (except for lifetime considerations) to that from N_2^+ at 3914 Å which arises from direct electron excitation. Therefore, photometers viewing upward along the magnetic field lines and scanning across an auroral arc, should see about the same intensity fall-off from the center to the edge of the arc at both 5577 Å and 3914 Å. The results of Romick and Belon, however, show that the brightness at 5577 Å falls off from the arc center faster than does that at 3914 Å.

According to Zipf (Reference 32), the dominant excitation mechanism for $O(^1S)$ in the aurora is photodissociation of O_2 by aurorally-generated EUV. We therefore sought to explore the possibility that trapping of EUV radiation near the arc center, with subsequent photodissociation of O_2, might account for the Romick and Belon result.

105

A detailed treatment of radiation trapping in an arc is clearly complex and involves a consideration of radiation transport. We attempted, instead, to determine the plausibility of the idea by estimating the (relative) energy density of EUV radiation across an arc based on a one-dimensional random walk model for the photons. In particular, we assumed a gaussian profile for the volume production rate of EUV photons across the arc. Each photon was then allowed to random walk in one dimension with a probability a_1 of resonant scatter and $(1 - a_1)$ of absorption at each scattering. Thus, if the volume production rate of EUV photons, as a function of distance x from the arc center, is given by

$$P(x) = P(0) \, e^{-x^2/2x_0^2} \quad , \tag{3-2}$$

it can then be shown that, for the simple model considered, the photon number density across the arc is determined from the equation,

$$n_\phi = \frac{P(0)}{nc\sigma_T} \sum_{m=1}^{\infty} a_1^{m-1} \sqrt{\frac{\lambda_0^2}{m\lambda_0^2 + x_0^2}} \exp\left(-\frac{x^2}{2(m\lambda_0^2 + x_0^2)}\right). \tag{3-3}$$

Here, n is the molecular concentration, c the speed of light, σ_T the total scattering cross section, and λ_0 the radiation mean free path.

Equation 3-3 is a superposition of gaussian functions each of which is broader than the volume production rate profile 3-2. Consequently, the energy density of the radiation field falls off more slowly from the arc center than does the photon production rate. But the photon (EUV) production rate should be proportional to the production rate of 3914 Å photons since both are proportional to the energy deposition rate. But if the 5577 Å emission is excited mainly by (EUV) dissociative excitation of O_2, then its volume emission profile should behave like that of the EUV energy density. The result should then be a broadening of the arc width seen at 5577 Å relative to that seen at 3914 Å, contrary to the observations of Romick and Belon.

The conclusion, subject to the limitations of the simple model adopted, is that the Romick and Belon observations cannot be accounted for through photodissociative excitation of $O(^1S)$ by trapped EUV photons.

Photo-Dissociative Excitation of $O(^1S)$

The quantum yield of $O(^1S)$ atoms resulting from the process

$$O_2 + h\nu \rightarrow O + O(^1S) \tag{3-4}$$

has been measured by Lawrence and McEwan (Reference 42). For wavelengths outside the range $850 \text{ Å} \lesssim \lambda \lesssim 1200 \text{ Å}$ the yield was found to be negligible. The peak yield occurs for $\lambda \sim 1050 \text{ Å}$ and attains a value of about 10 percent. This means that about 10 percent of the photons ($\lambda \approx 1050 \text{ Å}$) that are absorbed by O_2 are effective in producing $O(^1S)$ atoms. The average value over the indicated wavelength range is about 5 percent.

An upper limit to the volume excitation rate of $O(^1S)$ atoms by process 3-4 can now be estimated as follows. Let

$\dot{\mathscr{E}}$ = energy deposition rate by bombarding electrons

η_1 = fraction of energy radiated in interval 850 Å to 1200 Å

η_2 = fraction of the radiated energy absorbed by O_2

η_3 = quantum yield of $O(^1S)$ atoms

The excitation rate is then given by

$$\left\{ \frac{d[O(^1S)]}{dt} \right\}_{UV} \approx \eta_1 \eta_2 \eta_3 \, \dot{\mathscr{E}} \big/ \overline{h\nu} \tag{3-5}$$

where $\overline{h\nu}$ is the average photon (UV) energy.

Reliable estimates for η_1 are not available. However, study of our results on energy partition in an N_2, O_2, O mixture (mentioned above) leads us to assign a value of about 0.14.[*] This is very likely an upper limit. Other upper limits are $\eta_2 = 1$, and $\eta_3 = 0.1$. For an average photon wavelength of 1000 Å (12.4 eV), Equation 3-5 then leads to the result

$$\left\{\frac{d[O(^1S)]}{dt}\right\}_{UV} < 1 \times 10^{-3}\,\dot{\mathscr{E}} \quad . \tag{3-6}$$

As an example, consider the auroral arc of 27 March 1973 described in Section 2. At the altitude of peak energy deposition (≈ 101 km), we have $\dot{\mathscr{E}} = 2.7 \times 10^7$ eV cm^{-3} sec^{-1}. Equation 3-6 then yields

$$\left\{\frac{d[O(^1S)]}{dt}\right\}_{UV} < 2.7 \times 10^4 \ (\text{cm}^{-3}\ \text{sec}^{-1}) \quad . \tag{3-7}$$

Because of the upper limits assumed for the parameters, especially η_2, it seems likely that the value given by Equation 3-7 is too large by at least a factor of 2. Nevertheless, it is instructive to compare it with values for the dominant excitation processes included in the ARCTIC code. Table 3-2 shows the calculated excitation rates for $O(^1S)$ from these other processes at an altitude of 101 km in the auroral arc, 8.2 sec after onset. With the assumed rate coefficients (none of which is well known) nearly half of the excitation rate comes from quenching of $N_2(A^3\Sigma)$. Zipf (Reference 32) has suggested a rate coefficient for this quenching reaction of 1.5×10^{-11} cm^3 sec^{-1}. Use of this value would provide an even larger contribution from A-state quenching.[**]

_____

[*] This includes a contribution of 0.04 from wavelengths 1000 Å to 1200 Å along with the 0.10 contribution from Table 3-1 for wavelengths < 1000 Å.

[**] A value of 1.5×10^{-11} for this rate coefficient, along with the other excitation processes shown in Table 3-2, leads to 5577 Å intensities larger than observed on ICECAP. Consequently, the rate coefficient has been lowered to the value shown in Table 3-2.

Table 3-2. Volume excitation rates of $O(^1S)$ at 101 km
in auroral arc of 27 March 1973.

PROCESS	ASSUMED RATE CONSTANT ($cm^3\ sec^{-1}$)	VOLUME EXCITATION RATE ($cm^{-3}\ sec^{-1}$)
direct electron excitation	---	6.4^3
$O^+(^2D)+O_2 \longrightarrow O(^1S)+O_2^+$	1^{-10}	1.8^3
$O^+(^2P)+O_2 \longrightarrow O(^1S)+O_2^+$	1^{-10}	3.6^2
$N^+(^3P)+O_2 \longrightarrow O(^1S)+NO^+$	1^{-10}	1.3^4
$N^+(^1S)+O_2 \longrightarrow O(^1S)+NO^+$	1^{-10}	1.1^3
$N(^2P)+O_2 \longrightarrow O(^1S)+NO$	1^{-11}	2.1^4
$e+O_2^+ \longrightarrow O(^3P)+0.97\ O(^1D)$ $+0.03\ O(^1S)$	2.8^{-7}	5.4^3
$N_2(A^3\Sigma)+O(^3P) \longrightarrow N_2(X^1\Sigma)+O(^1S)$	5.0^{-12}	4.2^4
		$\sum = 9.1^4$

If the upper-limit contribution due to the UV (Equation 3-7) is now added to the results shown in Table 3-2, we find that it would contribute about 20 percent to the total excitation rate of $O(^1S)$. Realistically, the contribution is probably no greater than about 10 percent if the contributions from the other processes are reasonably accurate. This result is at variance with the above-mentioned conclusions of Zipf who attributes most of the excitation of $O(^1S)$ to the UV mechanism.

It should be cautioned, however, that the only excitation rates shown in Table 3-2 that we have some confidence in are those arising from the direct electron process and from dissociative recombination in O_2^+. Rate coefficients for the other processes are very uncertain. Therefore, no firm conclusions on the relative importance of the UV mechanism for excitation of 5577 Å emission can presently be made, and our preliminary conclusion is highly tentative, to say the least.

SECTION 4

ATMOSPHERIC HEAVE UNDER AURORAL ELECTRON BOMBARDMENT CONDITIONS

The MICE code has been used to estimate the atmospheric heave resulting from IBC Class III auroral electron bombardment conditions. The primary electron flux at the top of the atmosphere was taken to be

$$\Phi = 2.2 \times 10^5 \; e^{-E/8.5} \; . \qquad (cm^{-2} \; sec^{-1} \; eV^{-1}) \qquad (4-1)$$

This corresponds to an integrated energy deposition rate of 1.6×10^{13} eV $cm^{-2} \; sec^{-1}$.

The altitude dependence of the deposition rate (ergs $gm^{-1} \; sec^{-1}$) determined by the ARCTIC code is shown as the solid curve in Figure 4-1. For input to the MICE code we have approximated this curve by the dashed curve in Figure 4-1, namely, a deposition rate of 1.4×10^5 (ergs $gm^{-1} \; sec^{-1}$) above 100 km.

The pressure efficiency above 100 km is not well known. However, in order to obtain an upper limit on the atmospheric heave, we have arbitrar'y assumed an efficiency of 70 percent so that a constant value of 1×10^5 (ergs $gm^{-1} \; sec^{-1}$) is input as a heating rate above 100 km.

The results are shown in Figures 4-2 and 4-3. Figure 4-2 shows the altitude of selected air parcels as functions of time for the first 4 minutes of the bombardment. Figure 4-3 shows the vertical displacement of the air at 4 minutes as a function of the initial altitude. From Figure 4-3 we see that the maximum heave occurs at an altitude of about 145 km

111
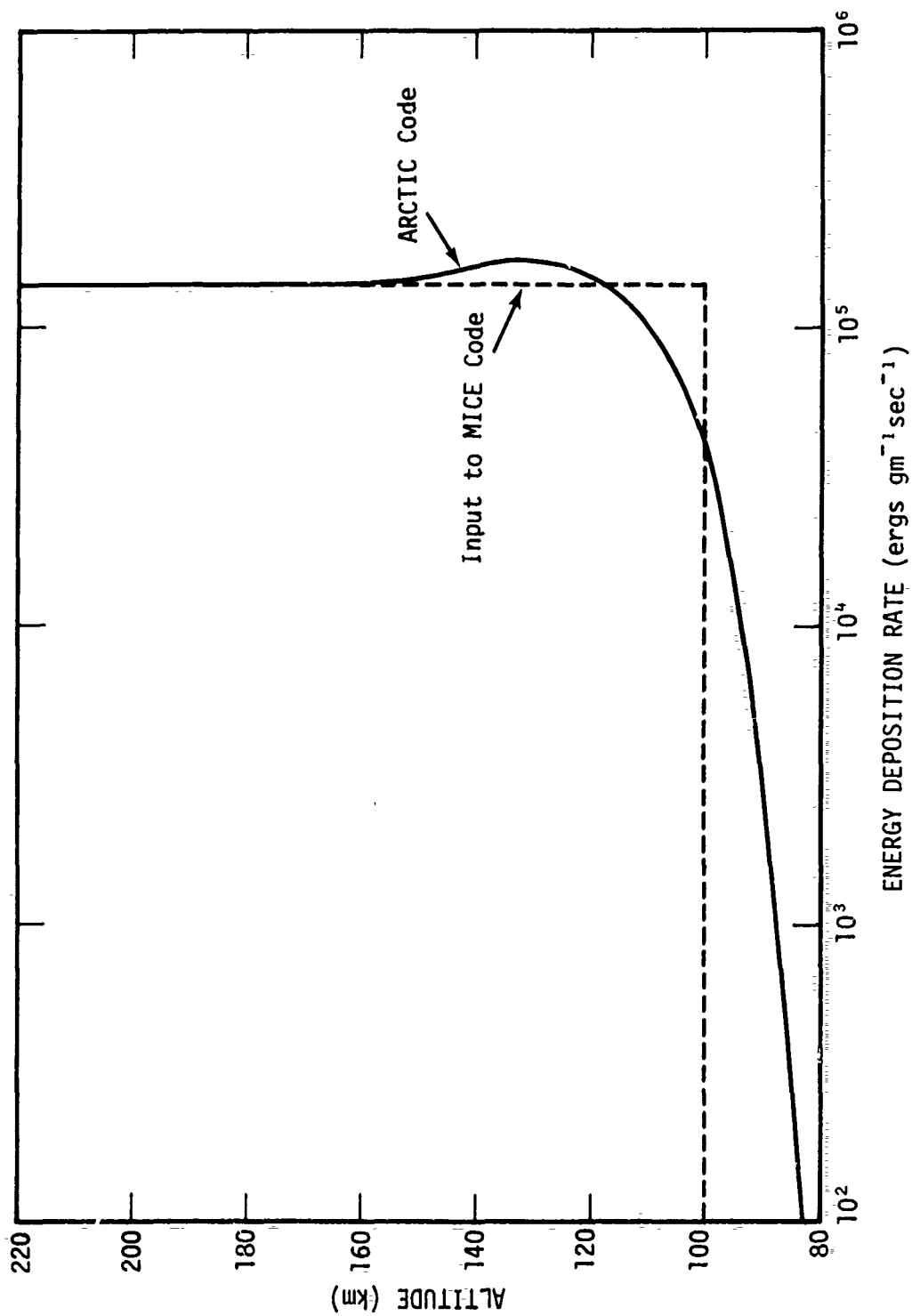
Figure 4-1. Energy deposition by auroral electrons adopted for heave calculation.
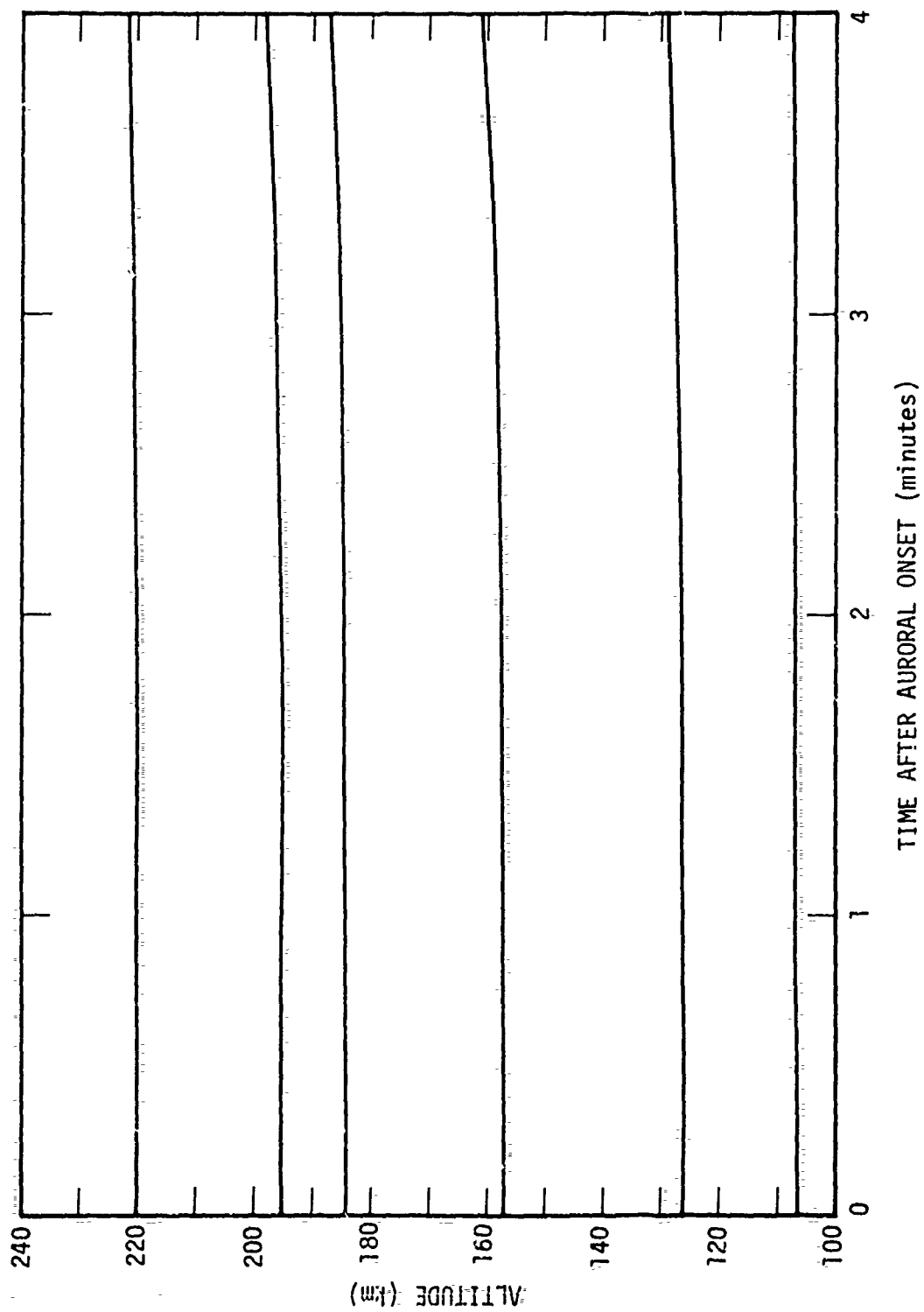
Figure 4-2. Atmospheric heave resulting from auroral electron bombardment.

113
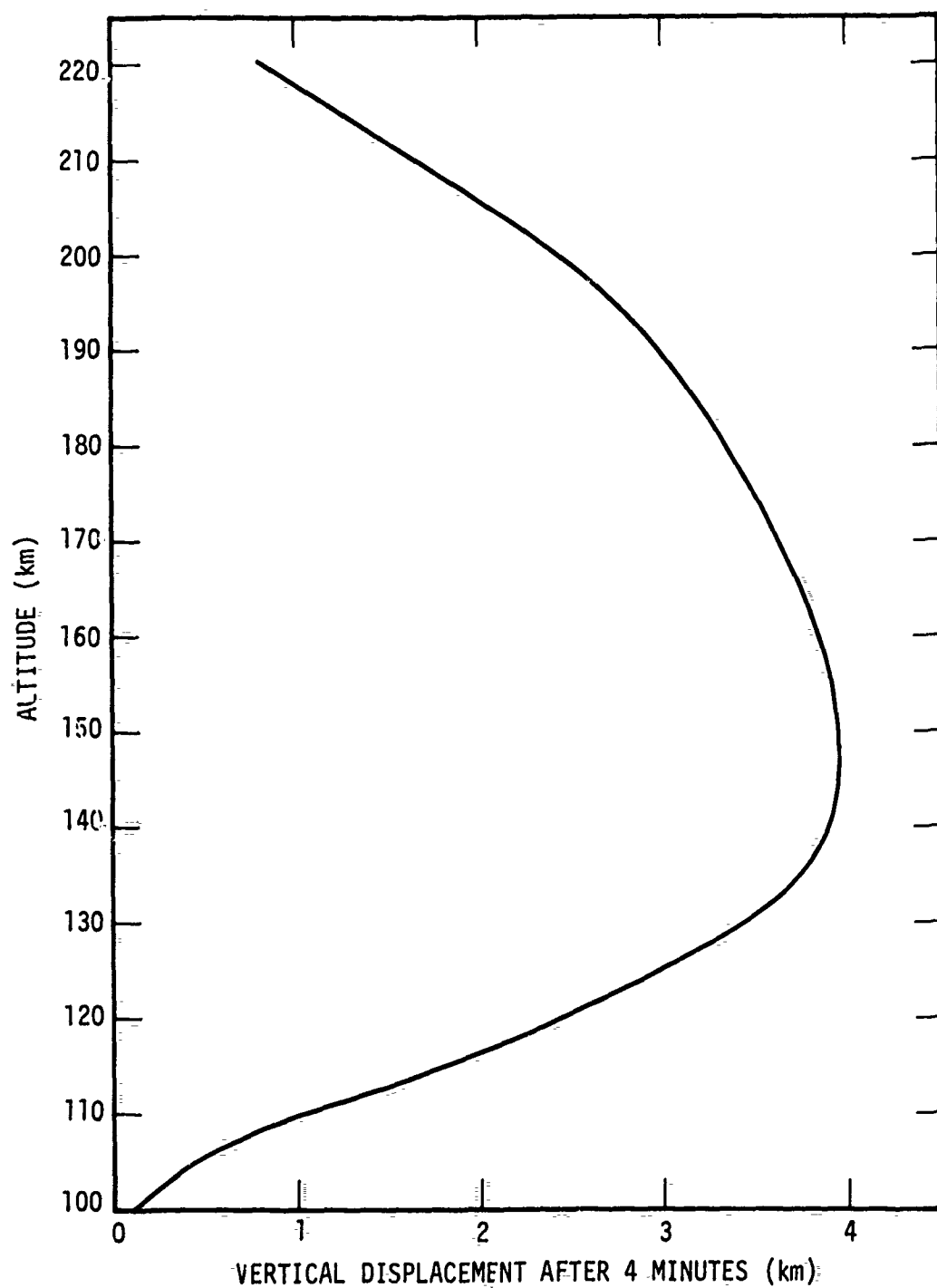
Figure 4-3. Vertical rise of atmosphere after 4 minutes of bombardment.

and attains a vertical displacement of less than 4 km after 4 minutes of continual bombardment. This is only about one fourth of the scale height at that altitude. The actual amount of heave is expected to be less than the results shown would indicate because we have used a pressure efficiency that is undoubtedly too high.

We conclude that atmospheric heave, resulting from ele·tron precipitation during an auroral event, is not a significant effec.. This conclusion is borne out by recent incoherent scatter measurements during the recovery phase of a magnetic substorm (Reference 43). The same measurements suggest, however, that heave at high altitudes resulting from joule heating by the electric field that drives the auroral electrojet, may serve to enhance the F-region ionization by significant amounts.

It should be noted, nevertheless, that evidence cited in Section 2 shows that the auroral zone latitudes undergo almost continual electron precipitation ranging from a weak "drizzle" to the intense bombardment associated with strong arcs. The calculations described above pertain to heave effects expected from strong events that are typically of short duration. We have not addressed the question of what may happen to the atmosphere at high latitudes when it undergoes a "drizzle" - type bombardment for days on end. It may, conceivably, produce a significant departure of the composition, or even the density, from that prevailing at lower latitudes.

SECTION 5
SUMMARY, DISCUSSION, CONCLUSIONS AND RECOMMENDATIONS

The work reported above has been divided into three main
categories: (1) Applications of the ARCTIC code, (2) EUV effects in the
aurora, and (3) Atmospheric heave from auroral electron precipitation. The
largest effort, by far, has gone into category (1), with particular emphasis
on a study of the auroral event of 27 March 1973 near Poker Flat, Alaska.
This section gives a brief summary of the results and conclusions of our
studies in these three areas, and lists some specific recommendations for
future action.

APPLICATIONS OF THE ARCTIC CODE

For potential use in weapon effects applications, the ARCTIC code
was first used to determine the energy partition that results from stopping
of keV electrons in normal air. The calculated partition into the various
excited states was tabulated. The accuracy of the results is not known
because many of the cross sections employed are quite uncertain. However,
the computed energy required to produce an ion pair in air agrees well with
the limited experimental data.

The code was then run for the case of a hypothetical auroral
event, and the resulting energy deposition profile was compared with ones
predicted by other codes. Our results were found to be in good agreement
with those from the Lockheed code, that performs the calculation in quite

116

a different way. Minor differences in the results can be attributed to differences in the assumed elastic scattering cross sections. Species excitation rates were also calculated and the results presented.

The major application of the ARCTIC code was to the auroral event of 27 March 1973, cited above. With the aid of data supplied to us by AFCRL, Photometrics, and Utah State University, we first constructed an approximate model to describe the geometrical and dynamical aspects of the event that consisted of a large drizzle region surrounding a smaller, but more intense, main arc. ARCTIC runs were made to assist in constructing the model, and subsequent runs were used to provide radiance and other data for comparison with observations. Conclusions, based on these comparisons, are as follows:

(1) At the time of rocket entry to the arc, the arc had a width ≈ 5 km (north-south) and was moving northward with a velocity ≈ 0.61 km $\sec^{-1}$. The associated drizzle region was probably of the "inverted-V" type and extended for a distance of about 540 km to the north and 310 km to the south of the main arc.

(2) Rocket photometer data of zenith brightness (3914 $\overset{o}{A}$) are inconsistent with the particle flux measurements. Either the particle data are too high by a factor ≈ 2 or else the photometer data are too low by a corresponding amount. Although our calculations were performed with the assumption that the particle data are too high, subsequent comparisons and considerations (including allowance for atmospheric transmission losses inherent in the ground-based photometer data) suggest that it is probably the 3914 $\overset{o}{A}$ photometer data that are in error.

(3) The calculated zenith radiance near 4.3 μm, including contributions from NO^{+} and CO_2, cannot account for the reported magnitude of the observed emission. Although the data from the spectrometer and

radiometer are not entirely consistent, our theoretical values are generally lower than those observed. The apparent constancy of the radiometer data with increasing rocket altitude above 120 km (if real) is a mystery.

(4) The calculated zenith radiance near 5.4 μm (NO chemilumin-escence) is as much as an order of magnitude lower than the observed values from both the dual channel radiometer and the CVF spectrometer. The meas-ured zenith radiance on rocket descent (viewing outside the arc) is nearly as great as that measured on ascent (viewing through the arc). This sur-prising result is not borne out by the calculations.

(5) Some of the data from the rocket-borne side-looking radiom-eters (2.7 and 5.4 μm) are contaminated by thermal emission from ejected parts of the rocket. However, other pieces of the data, believed to be aurorally produced, suggest that our computed NO radiances (at 2.7 μm) are low by at least an order of magnitude. This result is consistent with the findings in Item 4 above.

(6) The shapes of the observed (north- and south-viewing) radiance curves at 5199 Å are hard to reconcile with the calculated $N(^2D)$ emission. Suggested possibilities include (i) an additional strong source of $N(^2D)$ operating at low altitudes (~ 100 km) inside and outside the main arc (which, incidentally, would be consistent with Items 4 and 5 above), and (ii) contributions from direct excitation of permitted line radiation (N, N^+, O^+) that falls within the bandpass of the photometer.

(7) The shape of the observed (northward) 3466 Å radiance curve is also somewhat difficult to reconcile with the calculated $N(^2P)$ emission.

(8)   Comparisons with the observed electron density profile, and
also with the zenith radiance at 3914 $\overset{\circ}{A}$, suggest that our assumed particle
spectrum at energies < 3 keV contains too few electrons in the arc and too
many electrons in the drizzle region.

(9)   The positive ion mass spectrometer data imply that the NO
concentration between 100- and 105-km altitude was > 10^9 cm^{-3} in the vicinity
of the auroral arc. This represents nearly a 40-fold enhancement over cor-
responding low--latitude values.

(10)   Comparisons between the calculated zenith radiance at 1.27 μm,
and observations reported in the literature, suggest that auroral enhancement
of $O_2(^1\Delta)$ emission cannot be accounted for entirely on the basis of electron
precipitation.

With respect to the foregoing calculations, we should mention,
perhaps, that no account was taken of the electrojet. The work of Cole
(Reference 44) implies that at altitudes below 150 km, the effect of the
electrojet may be described (by means of a conductivity tensor in the
manner of Rees and Walker (Reference 45)) as joule heating. The ion tem-
perature can, conceivably, be raised above the neutral gas temperature,
although the unknown character of the electron precipitation over the
drizzle region would render difficult any reasonable assessment of the
electric field and the resulting increase in T_{ion}. However, temperature
increases by more than factors of 2 or 3 would not be expected, and we
believe that our neglect of the electrojet does not introduce serious errors.

In concluding our remarks, we wish to emphasize that the calcu-
lations and comparisons presented should be regarded as a "first-cut"
effort. Information obtained from additional and/or revised data, along
with insight gained from the above comparisons, will place us in a position
to define a better model for the auroral event and to reach more definitive
conclusions in the follow-on effort.

EUV EFFECTS IN AURORA

Two areas addressed with respect to possible extreme ultraviolet (EUV) effects in the aurora were: (a) the possibility that aurorally-generated EUV radiation, trapped in high-lying states of N_2, might leak out into the LWIR through transitions to neighboring states, thereby accounting for certain LWIR features observed from ICECAP rockets at high altitudes; (b) modification of the 5577 Å emission through EUV trapping and subsequent production of $O(^1S)$ by photodissociative excitation of O_2.

The conclusions reached, which are very tentative because of the almost total lack of data on the aurorally-generated EUV spectrum, are as follows:

(1) The N_2 molecule does not appear to be the source of the observed long wavelength infrared (LWIR) features. Bands that arise from states at energies below 12 eV in N_2 occur at the wrong wavelengths. States above about 12 eV, whose energy differences make them attractive candidates, are strongly predissociated and/or preionized and so will emit weakly, if at all.

(2) Based on an ARCTIC code study of energy partition, we estimate that not more than about 10 percent of the precipitated electron energy is radiated in the EUV.

(3) A simple model of photon transport leads to the conclusion that trapped EUV photons, that produce 5577 Å emission by photodissociative excitation of O_2, cannot account for the observed fact that auroral arcs are narrower when measured at 5577 Å than when measured at 3914 Å.

(4) No more than about 20 percent of the 5577 $\overset{\circ}{A}$ auroral emission can be attributed to photodissociative excitation of $O(^1S)$ by aurorally-generated UV radiation. This result, that is at variance with the findings of Zipf, is based partly on the validity of uncertain rate coefficients for chemical excitation, including the quenching reaction

$$N_2(A^3\Sigma) + O(^3P) \rightarrow N_2(X^1\Sigma) + O(^1S),$$
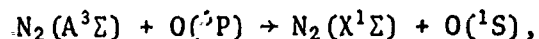
which we find to be the dominant source of $O(^1S)$ atoms.

AURORALLY-PRODUCED ATMOSPHERIC HEAVE

To study the possibility of atmospheric heave under auroral bombardment, the ARCTIC code was first run to establish an altitude profile of energy deposition under Class III auroral conditions. An approximation to the calculated profile was then used as input to the MICE code and, taking what we believe to be an upper limit for the pressure efficiency, we calculated the heave resulting from 4 minutes of continual bombardment.

The conclusion is that heave, under the stated conditions, is insignificant. The maximum effect occurs at 145 km where the vertical displacement of the air is only one fourth of the scale height at that altitude.

In spite of the foregoing conclusion, it seems possible, however, that the effects of prolonged bombardment in the auroral oval, that may occur almost continually, could lead to significant differences between the high- and low-latitude profiles. Resolution of this question would entail a calculation that takes into account additional effects such as winds, diffusion, solar radiation, etc.

RECOMMENDATIONS

In order to improve our understanding of the mechanisms involved in a disturbed environment, and to maximize the usefulness of future field data, the following recommendations are made. It is realized that some of them may be difficult to implement. They are listed in approximate order of importance as we currently view them.

(1) Rocket-borne optical and infrared instruments should be oriented so that they view upward along the magnetic field lines. Since the particle flux data permit a determination of the energy deposition and partition along the field lines, direct comparison between the computed and observed emissions would then be facilitated.

Instruments that look sideways receive radiation from long paths through (drizzle) regions that are not well defined, if at all, by the rocket-borne particle detectors. Calculated radiances for such paths are very uncertain and comparisons with the measured values are, therefore, much less valuable.

We realize that space limitations probably prevent the mounting of all optical/infrared instruments in the rocket nose. However, if it were possible to orient the rocket so that its axis were nearly horizontal, then the side-looking instruments could view upward along the field lines once per rocket spin.*

(2) Rocket flights, coordinated with satellite measurements of particle flux over a wide region surrounding the arc, would be very desirable. This is especially important if Item 1 above cannot be implemented, because information is needed to define the drizzle region that contributes in a dominant way to the radiance along sight paths that are not field aligned through the arc. In fact, such satellite-acquired data
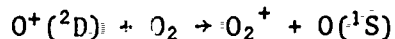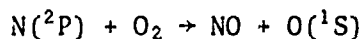
---

* Lacking this possibility, it is important that at least the 5199 Å photometer be mounted so as to view in the prescribed manner.

122

over a period of days prior to a proposed event would help to define the environmental conditions prevailing at the time of rocket launch.

(3) Instrument covers should not be ejected from the rocket, if possible. Their presence in the field of view of the (IR) instruments seriously degrades the usefulness of the data.

(4) A better understanding of the important excitation mechanisms for $O(^1S)$ atoms, leading to 5577 Å emission, can be achieved if rate coefficients for the following reactions are measured:

$$N_2(A^3\Sigma) + O(^3P) \rightarrow N_2(X^1\Sigma) + O(^1S)$$
$$N(^2P) + O_2 \rightarrow NO + O(^1S)$$
$$N^+(^3P) + O_2 \rightarrow NO^+ + O(^1S)$$
$$O^+(^2D) + O_2 \rightarrow O_2^+ + O(^1S)$$
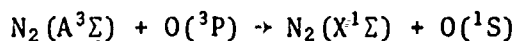
These are the dominant production sources for 5577 Å emission currently in the ARCTIC code, but their rate coefficients are quite uncertain. Direct electron excitation of $O(^1S)$ is not competitive with these sources nor, do we think, is photodissociation of O_2 the dominant mechanism. However, these conclusions could change if our assumed rate coefficients are too high.

(5) Rate coefficients involving the production and destruction of $N(^2P)$ atoms are also needed. These include

$$N^+(^1D) + O_2 \rightarrow N(^2P) + O_2^+$$
$$N^+(^1S) + O_2 \rightarrow N(^2P) + O_2^+$$
$$N(^2P) + O_2 \rightarrow NO + O$$

123
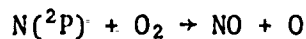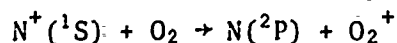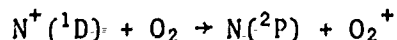
(6) Photon spectra and yields from the following chemiluminescent reactions need to be measured:

$$N(^2D) + O_2 \rightarrow NO + O \qquad\qquad (5.4,\ 2.7\ \mu m)$$

$$\left.\begin{array}{l} O_2^+ + NO \rightarrow NO^+ + O_2 \\ N_2^+ + O(^3P) \rightarrow NO^+ + N \end{array}\right\} \qquad (4.3\ \mu m)$$
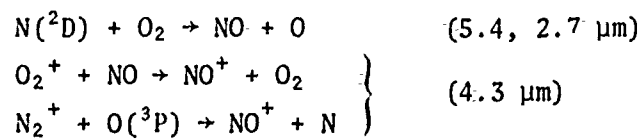
For the third reaction, the branching ratio for production of $N(^4S)$ and $N(^2D)$ atoms should also be obtained.

(7) In situ measurements of the EUV spectrum in an auroral environment are needed. Without such data, the importance of EUV effects on auroral interpretations will remain inconclusive.

REFERENCES

1. Tarr, P.W., D.H. Archer, N.G. Utterback, Studies of Auroral Simulation, DNA3297F, MRC-R-122, Mission Research Corporation, 11 April 1974.

2. Utterback, Nyle G., Is the Murcray Phenomenon Real? A Simple and Definite Test, MRC-N-124, Mission Research Corporation, February 7, 1974.

3. Jesse, W.P. and J. Sadauskis, Phys. Rev. 97, 1668 (1955).

4. Burt, D.A., and C.S. Davis, Rocket Instrumentation for ICECAP 73A, Auroral Measurements Program - Black Brant 18.205-1, AFCRL-TR-74-0195, Utah State University, February 1974.

5. Kofsky, I.L., and J.W. Schroeder, PHOTOMETRICS INC., private communication.

6. Ulwick, James, C., private communication.

7. Sharp, R.D., and R.G. Johnson, J. Geophys. Res. 73, 969 (1968).

8. Walker, J.C.G., et al., J. Geophys. Res. 73, 7285 (1968).

9. Frank, L.A., and K.L. Ackerson, J. Geophys. Res. 76, 3612 (1971).

10. Jones, R.A., and M.H. Rees, Planet. Space Sci. 21, 537 (1973)

11. Walker, J.K., J. Atm. Terr. Phys. 34, 1681 (1972).

12. Lincoln, J. Virginia, J. Geophys. Res. 78, 4005 (1973)

13. Zipf, E.C., J. Geophys. Res. 75, 6371 (1970).

14. Donahue, T.M., et al., Planet. Space Sci. 18, 171 (1970).

15. Swider, W., and R.S. Narcisi, J. Geophys. Res. 79, 2849 (1974).

16. Narcisi, R.S., private communication.

17. Meira, L.G., J. Geophys. Res. 76, 202 (1971).

18. Strobel, D.F., J. Geophys. Res. 76, 2441 (1971).

19.   Evans, D.S., J. Geophys. Res. 79, 2853 (1974).

20.   Romick, G.J., and A.E. Belon, Planet.Space Sci. 15, 1695 (1967).

21.   Baker, K., private communication.

22.   Degges, T.C., App. Optics. 10, 1856 (1971).

23.   Kumer, J.B., and T.C. James, J. Geophys. Res. 79, 638 (1974).

24.   Malkmus, W., J. Opt. Soc. Am. 53, 951 (1963).

25.   Wiese, W.L., et al., Atomic Transition Probabilities, V.I., Hydrogen
      Through Neon, NSRDS-NBS-4, National Bureau of Standards, 20 May 1966.

26.   Gattinger, R.L., and A. Vallance Jones, J. Geophys. Res. 78, 8305 (1973).

27.   Swider, W., J. Geophys. Res. 79, 3221 (1974).

28.   Evans, W.F.J., et al., Can. J. Phys. 48, 747 (1970).

29.   McClatchey, R.A. and J.E.A. Selby, Atmospheric Attenuation of Laser
      Radiation from 0.76 to 31.25 μm, AFCRL-TR-74-0003, Air Force Cambridge
      Research Laboratories, 3 January, 1974.

30.   Zipf, E.C., private communication

31.   Zipf, E.C., Trans. Am. Geophys. Union, 54, 403 (April 1973)

32.   Zipf, E.C., Trans. Am. Geophys. Union, 54, 1155 (Dec. 1973).

33.   Zipf, E.C., Trans. Am. Geophys. Union, 55, 363 (April 1974).

34.   Stair, A.T., et al., ICECAP meeting, Washington D.C., October 1973.

35.   Wyatt, C.L., and D.J. Baker, Rocket Launch of an LWIR Spectrometer
      Into an Aurora, final report, Utah State University, June 30, 1973.

36.   Saum, K.A., and W.M. Benesch, App. Optics, 9, 195 (1970).

37.   Hudson, R.D., and V.L. Carter, J. Geophys. Res. 74, 393 (1969).

38.   Carter, V.L., and J. Berkowitz, J. Chem. Phys. 59, 4573 (1973).

39.   Tilford, S.G., and P.G Wilkinson, J. Mol. Spectr. 12, 231 (1964).

40.   Ajello, J.M., J. Chem. Phys. 53, 1156 (1970).

41. Aarts, J.F.M., and F. J. DeHeer, Physica 52, 45 (1971).

42. Lawrence, G.M., and M.J. McEwan, J. Geophys. Res 78, 8314 (1973).

43. Bates, H. F., Planet. Space Sci. 21, 2073 (1973).

44. Cole, K.D., J. Atmos. Terr. Phys. 33, 1241 (1971).

45. Rees, M.H., and J.C.G. Walker, Ann. Geophy. 24, 119, (1968).

46. Herzberg, G., Spectra of Diatomic Molecules, Van Nostrand (1950).

47. Thulstrup, E.W., and Y. Öhrn, J. Chem. Phys. 57, 3716 (1972).

48. Billingsley, F.P., Chem. Phys. Lett. 23, (15 November 1973).

49. Stair, A. T., and H.P. Gauvin, in: Aurora and Airglow, ed. B.M. McCormac (Reinhold, New York, 1967) p. 365.

APPENDIX A

SPECTRAL DISTRIBUTION OF NO CHEMILUMINESCENT EMISSION FROM THE REACTION $N(^2D) + O_2 \rightarrow NO + O$

The spectral distribution of energy emitted in the fundamental (5.4 μm) and first overtone (2.7 μm) bands of NO from the $N(^2D) + O_2$ re- action has not been measured. It can be calculated if the distribution among vibrational states of NO immediately following the reaction is known. Unfortunately, this information is not available. However, in conformity with the assumptions made earlier with respect to chemiluminescence, we will assume that the vibrational levels are populated with equal probability up to the maximum allowed by energy conservation. On this basis, we proceed to derive the spectral distributions, making due allowance for the rotational structure of the bands.

If n is the highest vibrational state permitted by energy conser- vation (n=18 for the $N(^2D)+O_2$ reaction), we then assume that the probability of populating any of the levels $v=0,1,2,---, n$ is the same. With this assumption, it can then be shown that, for the fundamental bands, the average number of transitions $(v \rightarrow v-1)$ that occur following cascade is given by

$$\mathcal{N}_{v,v-1} = \frac{N(v)}{n+1} A_{v,v-1} / (A_{v,v-1} + A_{v,v-2}) \tag{A-1}$$

where $A_{v,v-1}$ and $A_{v,v-2}$ are the radiative transition probabilities for transitions $v \rightarrow v-1$ and $v \rightarrow v-2$, respectively. The quantity $N(v)/(n+1)$, which is the average occupation of vibrational level v per molecule, is determined from the equation

$$N(v) = 1 + N(v+1) \cdot A_{v+1,v} / (A_{v+1,v} + A_{v+1,v-1})$$

$$+ N(v+2) \cdot A_{v+2,v} / A_{v+2,v} + A_{v+2,v+1}) \qquad \text{(A-2)}$$

with $N(n) = 1$; $N(n+1) = N(n+2) = 0$.

The transition probabilities (sec^{-1}) corresponding to the fundamental and first overtone vibrations are, respectively,

$$A_{v,v-1} = 2.8 \times 10^{-8} S_0 \; \tilde{\nu}^2_{v,v-1} \cdot v \qquad \text{(A-3)}$$

and

$$A_{v,v-2} = 1.4 \times 10^{-8} S_0' \; \tilde{\nu}^2_{v,v-2} \cdot v(v-1) \qquad \text{(A-4)}$$

where S_0 and S_0' are the integrated absorption coefficients (cm^{-2}atm^{-1}) at N.T.P. for the fundamental and first overtone bands, respectively. The wavenumbers (cm^{-1}) of the fundamental and first overtone transitions are given, respectively, by

$$\nu_{v,v-2} = \omega_e - 2v\,\omega_e x_e + (3v^2 + 1/4)\,\omega_e y_e \qquad \text{(A-5)}$$

and

$$\tilde{\nu}_{v,v-2} = 2[\omega_e - (2v-1)\,\omega_e x_e + (3v^2 - 3v + 7/4)\,\omega_e y_e]. \qquad \text{(A-6)}$$

Similarly, for the first overtone bands,

$$\mathcal{N}_{v,v-2} = \frac{N(v)}{n+1}\, A_{v,v-2} / (A_{v,v-1} + A_{v,v-2}). \qquad \text{(A-7)}$$

Table A-1 shows the values adopted here for the various molecular constants appearing above and below.

Table A-1. Values adopted for molecular constants of $NO(X^2\Pi)$.

ω_e (cm^{-1})	$\omega_e x_e$ (cm^{-1})	$\omega_e y_e$ (cm^{-1})	S_0 (cm^{-2}atm^{-1})	S_0' (cm^{-2}atm^{-1})	B_e (cm^{-1})	α_e (cm^{-1})	Λ
1904.03	13.97	-0.0012	128	2.11	1.7046	0.0178	1

Let $f(\nu_{v,v-1})$ be the fraction of the total fundamental band energy emitted per reaction in the $v \to v-1$ transition. It follows from the foregoing that

$$f(\nu_{v,v-1}) = \tilde{\nu}_{v,v-1} \, \mathcal{N}_{v,v-1} / \sum_{v=1}^{n} \tilde{\nu}_{v,v-1} \, \mathcal{N}_{v,v-1}. \qquad (A-8)$$

Similarly, for the overtone bands,

$$f(\tilde{\nu}_{v,v-2}) = \nu_{v,v-2} \, \mathcal{N}_{v,v-2} / \sum_{v=2}^{n} \tilde{\nu}_{v,v-2} \, \mathcal{N}_{v,v-2}. \qquad (A-9)$$

Table A-2 shows the calculated values of f for each of the bands comprising the fundamental and first overtone band systems.

Each vibrational band within the fundamental and first overtone band systems has a rotational structure composed of many rotation-vibration lines. The lines form part of the P, Q, or R branches of the band if the rotational quantum number changes by -1, 0, or +1, respectively. In particular, the frequencies (cm^{-1}) of the vibration-rotation lines of the P, Q, and R branches of a band that arises from a $v' \to v''$ transition are given by[*] (Reference 46):

---

[*] The treatment presented here ignores fine structure effects due to a non-zero electron spin of the ground electronic state of NO. For the resolution considered, this is entirely adequate.

Table A-2. Calculated values for $f(\widetilde{\nu}_{V,V-1})$ and $f(\widetilde{\nu}_{V,V-2})$.

Transition	$\lambda(\mu m)$	f	Transition	$\lambda(\mu m)$	f
1- 0	5.330	1.47^{-1}	2- 0	2.685	2.77^{-2}
2- 1	5.411	1.29^{-1}	3- 1	2.726	4.85^{-2}
3- 2	5.494	1.13^{-1}	4- 2	2.768	6.37^{-2}
4- 3	5.579	9.86^{-2}	5- 3	2.812	7.42^{-2}
5- 4	5.667	8.61^{-2}	6- 4	2.857	8.09^{-2}
6- 5	5.758	7.51^{-2}	7- 5	2.903	8.43^{-2}
7- 6	5.853	6.52^{-2}	8- 6	2.951	8.49^{-2}
8- 7	5.950	5.63^{-2}	9- 7	3.001	8.34^{-2}
9- 8	6.050	4.83^{-2}	10- 8	3.052	7.99^{-2}
10- 9	6.154	4.12^{-2}	11- 9	3.105	7.48^{-2}
11-10	6.261	3.47^{-2}	12-10	3.160	6.84^{-2}
12-11	6.372	2.88^{-2}	13-11	3.217	6.10^{-2}
13-12	6.488	2.35^{-2}	14-12	3.276	5.26^{-2}
14-13	6.607	1.88^{-2}	15-13	3.337	4.35^{-2}
15-14	6.731	1.44^{-2}	16-14	3.401	3.41^{-2}
16-15	6.859	1.05^{-2}	17-15	3.467	2.35^{-2}
17-16	6.993	6.81^{-3}	18-16	3.536	1.46^{-2}
18-17	7.131	3.99^{-3}			

$$\tilde{\nu}_P = \nu_{v'v''} + (B_{v'}-B_{v''})\, J^2 + (B_{v'}-3B_{v''})\, J + (B_{v''}-B_{v'})\, \Lambda^2 - 2B_{v''}$$

$$(J=0,1,2,\text{---}) \qquad \text{(A-10)}$$

$$\tilde{\nu}_Q = \tilde{\nu}_{v'v''} + (B_{v'}-B_{v''})\, J^2 + (B_{v'}-B_{v''})\, J + (B_{v''}-B_{v'})\, \Lambda^2 \quad (J=0,1,2,\text{---})$$

$$\text{(A-11)}$$

$$\nu_R = \tilde{\nu}_{v'v''} + (B_{v'}+B_{v''})\, J + (B_{v'}-B_{v''})\, J^2 + (B_{v''}-B_{v'})\, \Lambda^2 \quad (J=1,2,3,\text{---})$$

$$\text{(A-12)}$$

Here, $\tilde{\nu}_{v'v''}$ is the frequency in the absence of any rotational considerations (given by Equations A-5 and A-6), J is the rotational quantum number of the upper state involved in the transition. Λ is the quantum number associated with the electron angular momentum about the internuclear axis, and B_v is determined in terms of the rotational constants B_e and α_e by the equation

$$B_v = B_e - \alpha_e\,(v+1/2). \qquad \text{(A-13)}$$

Values for the rotational and other constants used above are shown in Table A-1.

If a Boltzmann distribution among the rotational states is assumed, the intensities of the rotational lines within the P, Q, and R branches are then given by the following expressions (Reference 46):

$$I_P(v',J) = \frac{K\,\tilde{\nu}_p^4}{Q_r}\,\frac{(J+1+\Lambda)(J+1-\Lambda)}{J+1}\,e^{-hcF_{v'}(J)/kT} \qquad (J=0,1,2,\text{---})$$

$$\text{(A-14)}$$

$$I_Q(v',J) = \frac{K\,\tilde{\nu}_Q^4}{Q_r}\,\frac{(2J+1)\Lambda^2}{J(J+1)}\,e^{-hcF_{v'}(J)/kT} \qquad (J=1,2,3,\text{---}) \qquad \text{(A-15)}$$

133

$$I_R(v',J) = \frac{K \, \widetilde{\nu}_R^4}{Q_r} \frac{(2J'+1)\Lambda^2}{J(J+1)} e^{-hcF_{v'}(J)/kT} \quad (J=1,2,3,\text{---}) \quad \text{(A-16)}$$

Here, K is a constant, Q_r is the rotational part of the partition function, and $F_v(J)$, the rotational energy (cm^{-1}) of a state with vibrational and rotational quantum numbers v and J, respectively, is given by

$$F_v(J) = B_v \, J(J+1) - B_v \Lambda^2. \quad \text{(A-17)}$$

The foregoing relations, together with the results shown in Table A-2, are sufficient to determine the spectral distribution of energy emitted by NO from the $N(^2D)+O_2$ reaction. In particular, the fraction, $g_P(v',J)$, of the energy of a given band (specified upper (v') and lower (v'') vibrational quantum numbers) that is emitted in a P-branch transition from an upper state with rotational quantum number J, is just

$$g_P(v',J) = I_P(v',J)/I(v'), \quad \text{(A-18)}$$

where

$$I(v') = \sum_J [I_P(v',J) + I_Q(v',J) + I_R(v',J)]. \quad \text{(A-19)}$$

Thus, for example, the fractional contribution of this transition to the total energy emitted in the fundamental band system of NO is $f(\widetilde{\nu}_{v',v'-1}) \, g_P(v',J)$.

In computing the spectral distributions, we have included contributions for rotational states up to $J=30$. The fractional contributions of all lines falling in a given wavelength interval were then summed. The wavelength intervals (spectral resolution) chosen for the fundamental and overtone band systems are 0.033 μm and 0.025 μm, respectively. The temperature was taken to be 250 °K, corresponding to conditions at about 110-km

134

altitude. The results are shown in Figures A-1 and A-2. In these figures, the ordinate gives the fraction of the total energy emitted in the band system within the incremental wavelength interval chosen. For example, from Figure A-1 we see that 5.1 percent of the energy emitted per reaction in the fundamental band system occurs between 5.4 and 5.433 μm.
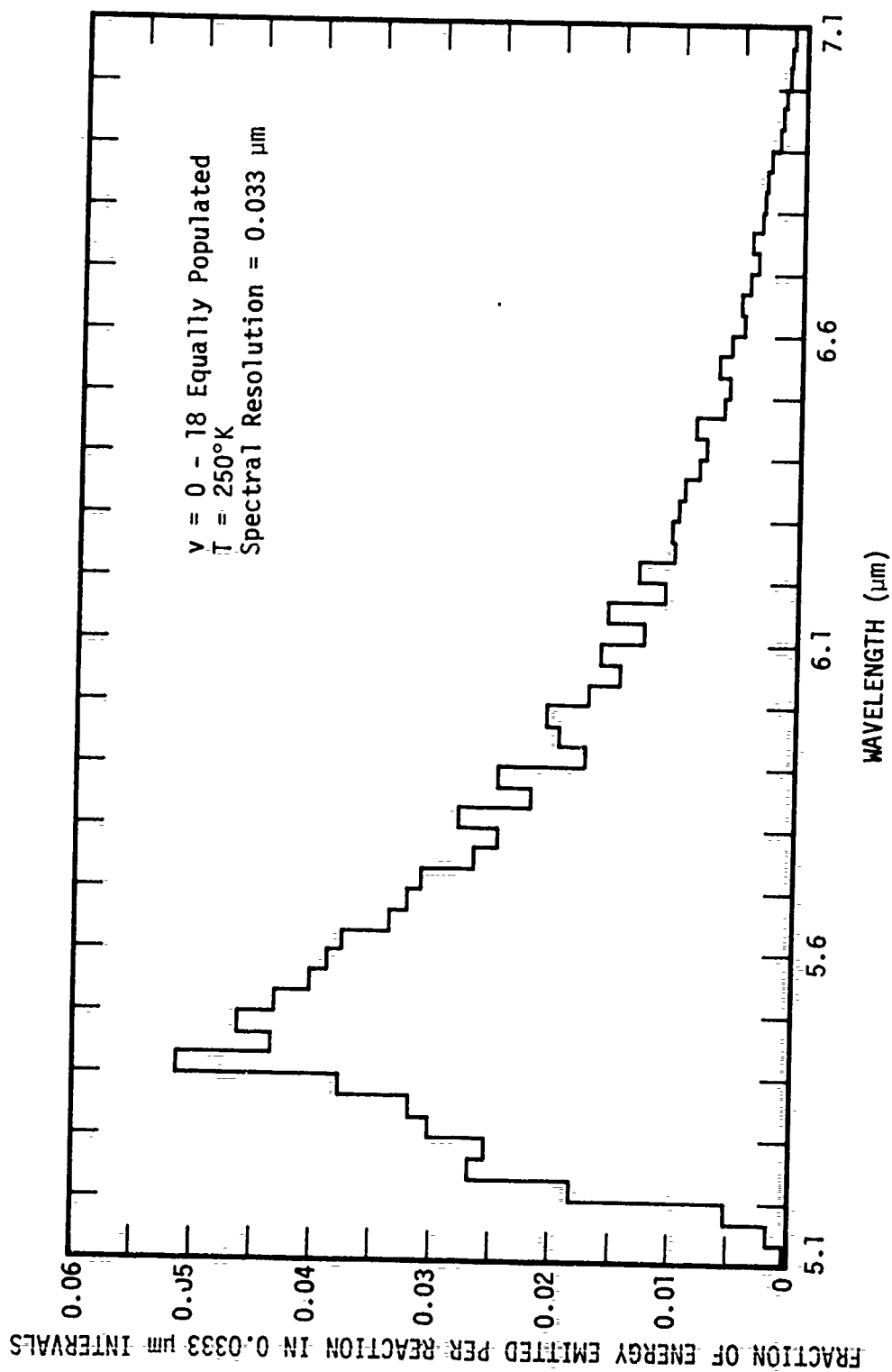
Figure A-1. Calculated spectrum of NO (fundamental) emission from the $N(^2D)+O_2$ reaction.

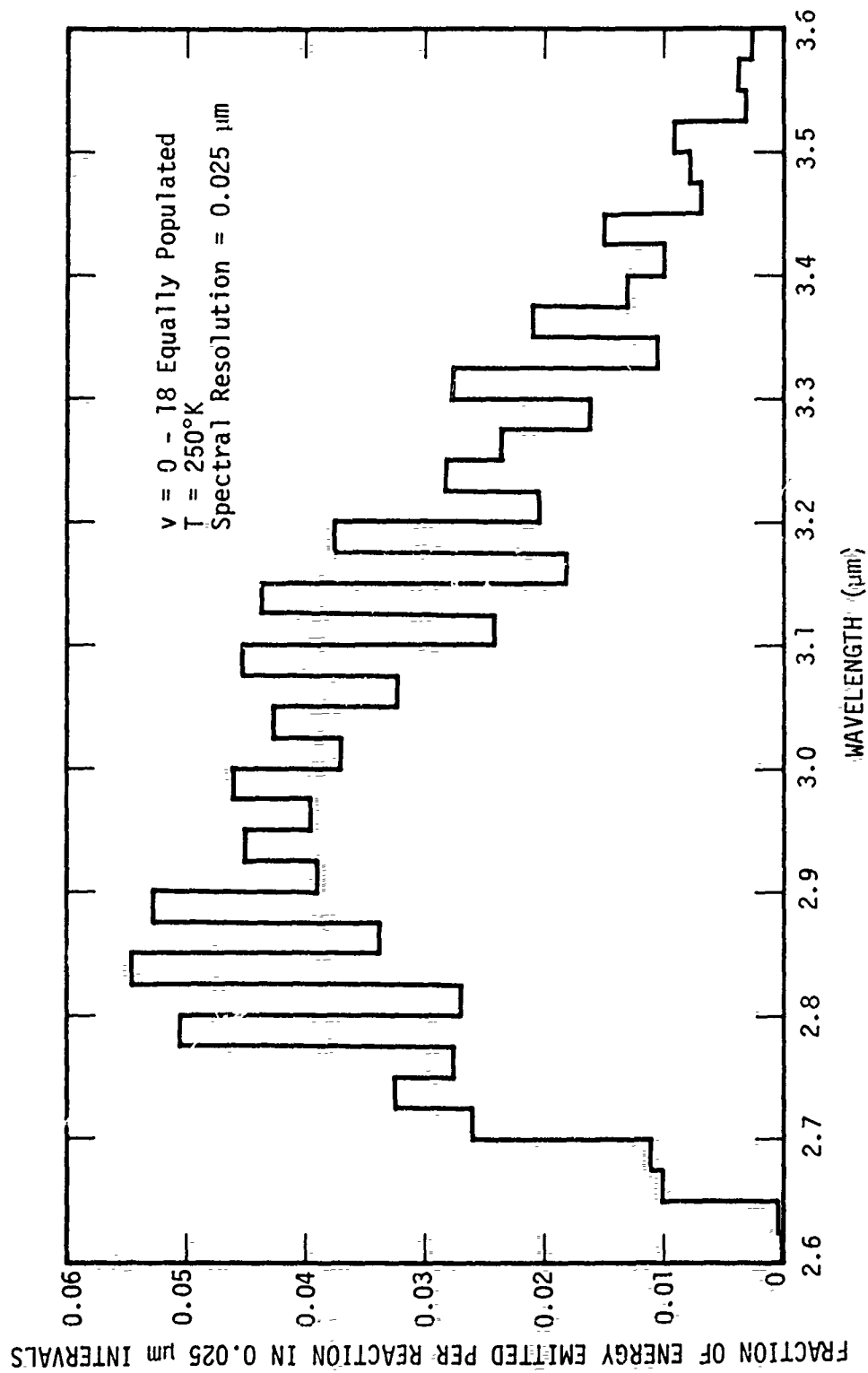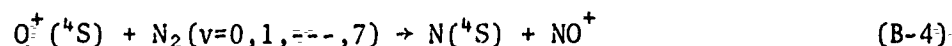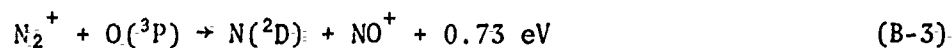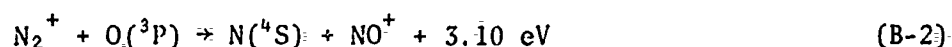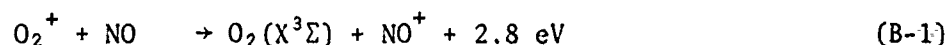Figure A-2. Calculated spectrum of NO (first overtone) emission from the $N(^2D)+O_2$ reaction.

APPENDIX B

SPECTRAL DISTRIBUTION OF NO^+ CHEMILUMINESCENT
EMISSION FROM THE REACTIONS
$O_2^+ + NO \rightarrow O_2 + NO^+$ AND $N_2^+ + O \rightarrow NO^+ + N(^4S)$

The ARCTIC code calculates the chemiluminescent emission from the 4.3-μm fundamental band of NO^+ by including contributions from the reactions:

$$O_2^+ + NO \quad \rightarrow O_2(X^3\Sigma) + NO^+ + 2.8 \text{ eV} \tag{B-1}$$

$$N_2^+ + O(^3P) \rightarrow N(^4S) + NO^+ + 3.10 \text{ eV} \tag{B-2}$$

$$N_2^+ + O(^3P) \rightarrow N(^2D) + NO^+ + 0.73 \text{ eV} \tag{B-3}$$

$$O^+(^4S) + N_2(v=0,1,---,7) \rightarrow N(^4S) + NO^+ \tag{B-4}$$

Since the photon efficiency for each reaction is presently unknown, the usual assumption is made that one half of the available energy goes into vibrational excitation of NO^+. On this basis, the calculations described in this report have shown that most of the NO^+ chemiluminescence arises from Reactions B-1 and B-2. The exothermicity of these two reactions is sufficient to populate the vibrational levels of NO^+ up to $v = 10$.

The procedure used to determine the spectral distribution of the emitted photons is similar to that described in Appendix A and will not be repeated here. The main difference between the treatment here and that for NO in Appendix A arises because NO^+ possesses a Σ ground electronic state and, consequently, the Q- branch lines are missing from its spectrum.

Preceding page blank

The molecular parameters for NO^+ are not well established. The values adopted here are shown in Table B-1 together with the corresponding references. Values for S_0, and S_0', the integrated absorption intensities of the fundamental and first overtone bands, respectively, are substantially lower than the values reported by Stair et al., (Reference 49). However, only the ratio between these quantities is involved in our calculations, and for this ratio the results reported in References 48 and 49 are reasonably close.

Table B-1. Values adopted for molecular constants of $NO^+(X^1\Sigma)$

Parameter	Value	Reference
$\omega_e(cm^{-1})$	2377	47
$\omega_e x_e(cm^{-1})$	16	47
$B_e(cm^{-1})$	2.002	47
$\alpha_e(cm^{-1})$	0.020	47
$S_0(cm^{-2} atm^{-1})$	88.8	48
$S_0'(cm^{-2} atm^{-1})$	0.6	48

The frequencies of the vibration-rotation lines of the bands are determined from Equations A-5, A-6, A-10, and A-12 with $\Lambda = 0$.

The fraction of the total energy of the fundamental band system emitted per reaction in the $v \rightarrow v - 1$ transitions and, correspondingly, for the first overtone system in the $v \rightarrow v - 2$ transitions, is shown in Table B-2 (compare Table A-2 for the case of NO).

Table B-2. Relative importance of contributing bands to
the fundamental and first overtone systems
in NO^+ chemiluminescence.

Transition	$\lambda(\mu m)$	f	Transition	$\lambda(\mu m)$	f
1-0	4.264	2.02^{-1}	2-0	2.147	6.23^{-2}
2-1	4.323	1.75^{-1}	3-1	2.177	1.07^{-1}
3-2	4.384	1.50^{-1}	4-2	2.208	1.35^{-1}
4-3	4.446	1.26^{-1}	5-3	2.239	1.49^{-1}
5-4	4.511	1.04^{-1}	6-4	2.272	1.50^{-1}
6-5	4.577	8.40^{-2}	7-5	2.305	1.39^{-1}
7-6	4.645	6.50^{-2}	8-6	2.340	1.18^{-1}
8-7	4.715	4.74^{-2}	9-7	2.375	8.85^{-2}
9-8	4.787	3.10^{-2}	10-8	2.412	5.12^{-2}
10-9	4.861	1.56^{-2}			

The spectral distributions were calculated assuming a Boltzmann distribution of rotational states at a temperature of 250 °K. The wavelength interval (spectral resolution) chosen for the fundamental and first overtone band systems is 0.02 μm. The results are shown in Figures B-1 and B-2. In these figures, the ordinate gives the fraction of the total energy emitted in the band system within the incremental wavelength interval chosen. For example, from Figure B-1 we see that about 3.1 percent of the energy emitted per reaction in the fundamental band system occurs between 4.2 and 4.22 μm.

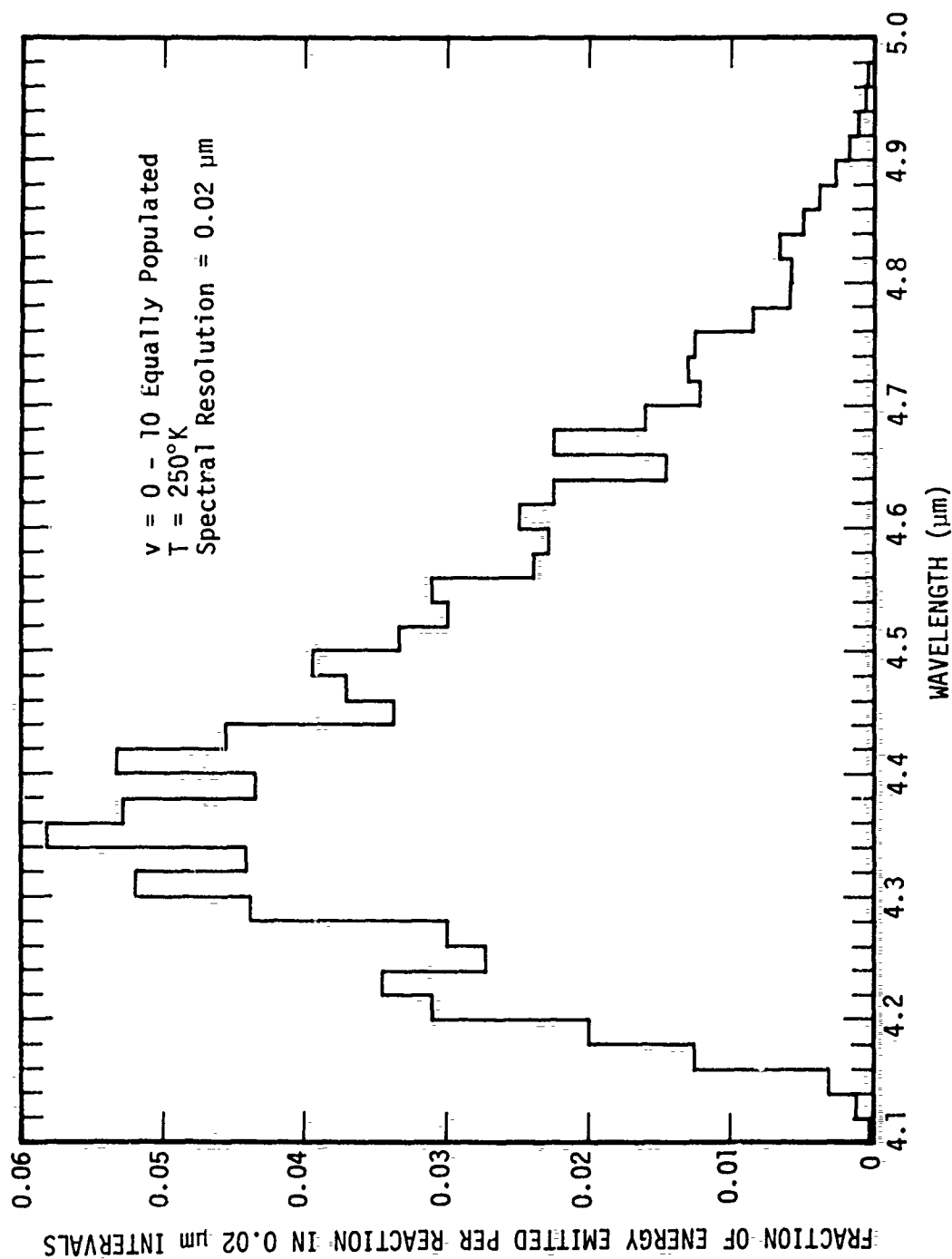Figure B-1. Calculated spectrum of NO^+ (fundamental) emission from the reactions $O_2^+ + NO \rightarrow O_2 + NO^+$ and $N_2^+ + O(^3P) \rightarrow NO^+ + N(^4S)$.
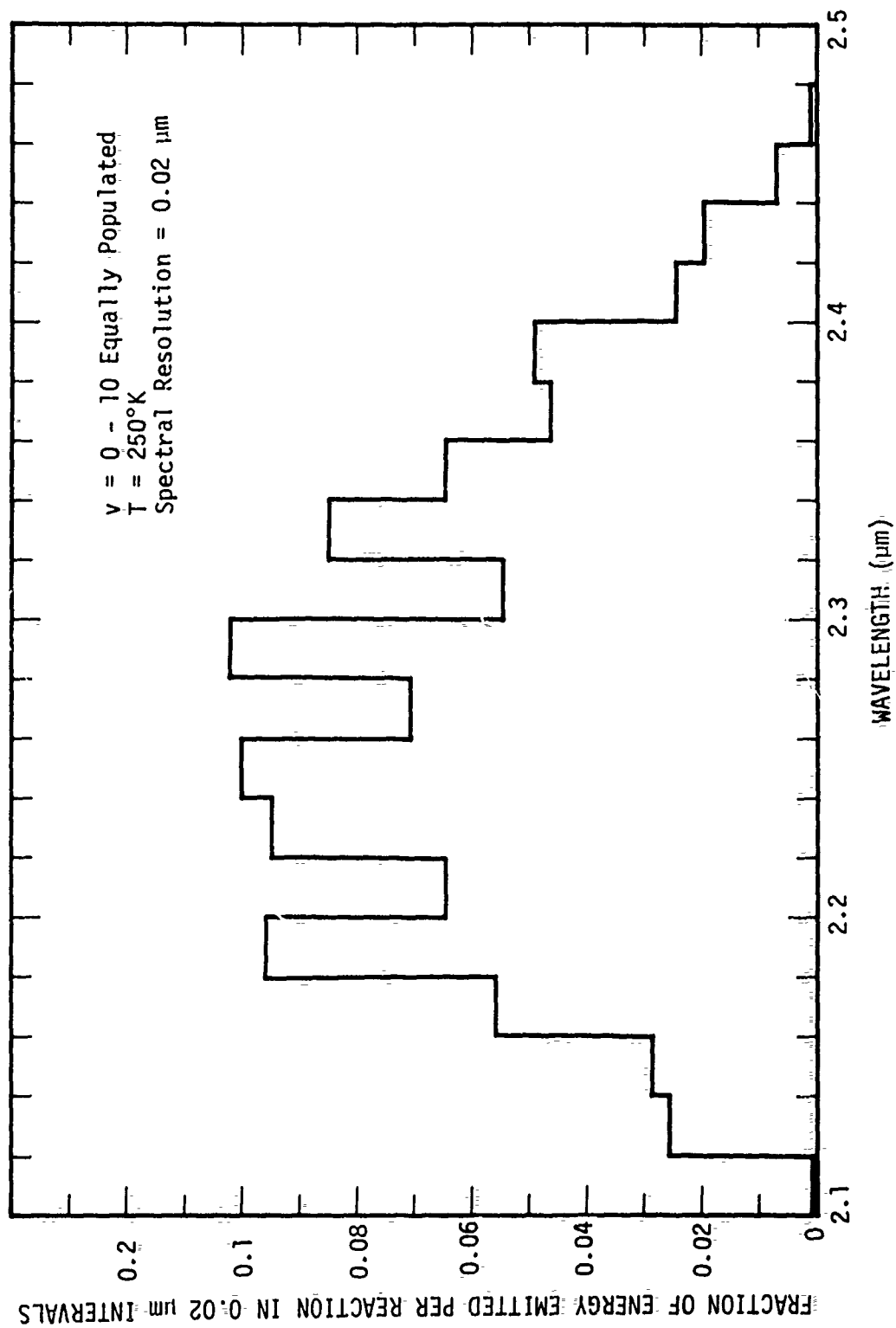
Figure B-2. Calculated spectrum of NO^+ (overtone emission) from the reactions $O_2^+ + NO \rightarrow O_2 + NO^+$ and $N_2^+ + O(^3P) \rightarrow NO^+ + N(^4S)$.

APPENDIX C
LISTING OF THE ARCTIC CODE

This appendix provides a listing (on microfiche) and a brief description of the ARCTIC code.

The ARCTIC code has the schematic structure indicated in Figure C-1. The (0,0) overlay consists of the main program ARCTIC which is essentially a driver program and three subroutines, ECRD, LATS, and ATMS. These subroutines are common to many of the subsequent overlays called. During execution, the ARCTIC main program calls one of the seven overlays CHEM, ELDEP, UVDEP, IFAC, EDIT, APOT, PIPUT depending on the function to be performed. These functions are described below.

Overlay (7,0) (main program PIPUT) reads in all data and initializes all common blocks and large core memory. This overlay also calculates all storage parameters, initializes the main deposition grid (if no restart is involved) and determines whether it is a one, two or three dimensional problem.

Overlay (2,0) (main program ELDEP) deposits the energy from the incoming electrons and partitions it among the different states. In the case of a two- or three- dimensional problem the entire deposition is done before returning to the main program ARCTIC.

Overlay (3,0) (main program UVDEP) is at present a dummy one. It is included in order to make future provision for the transport and deposition of UV radiation generated by the bombarding electrons.
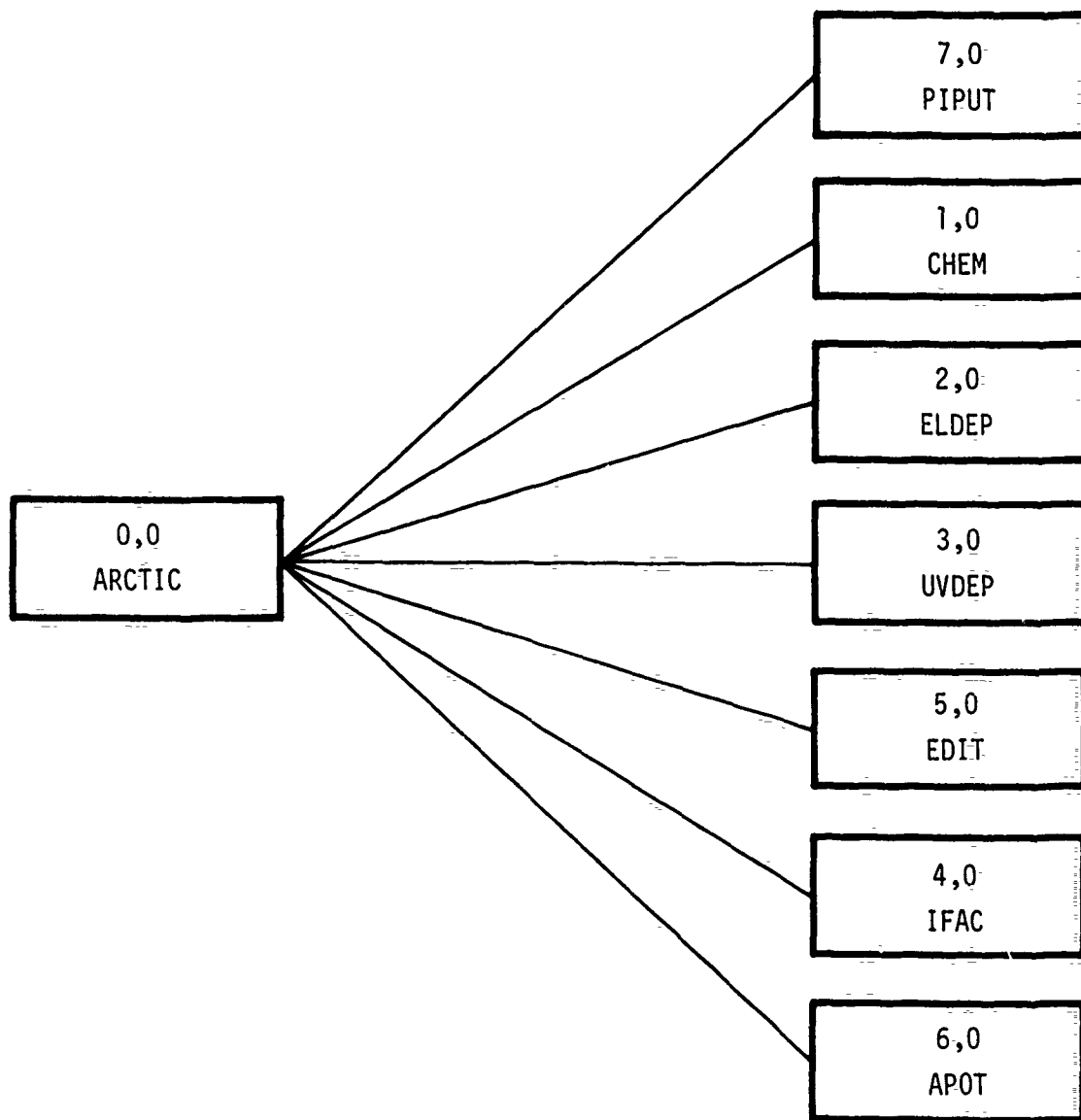
Figure C-1. Schematic structure of the ARCTIC code.

Overlay (5,0) (main program EDIT) is an output routine, which prints all relevant information on the electron and UV depositions.

Overlay (4,0) (main program IFAC) is an interface routine used for converting data between the overlays (2,0) (ELDEP), (3,0) (UVDEP) and overlay (1,0) (CHEM). This routine allows some flexibility in altering the deposition and chemistry overlays separately.

Overlay (6,0) (main program APOT) is a dummy.

Overlay (1,0) (main program CHEM) uses the output of overlay (4,0) to perform the subsequent chemistry. This overlay actually performs the integration of the coupled, time-dependent differential equations.

The microfiche listing of the code is enclosed in the envelope attached to the inside of the back cover.